

Design and optimisation of a type IV composite pressure vessel

M.V.R. van Meijel

Delft University of Technology

Design and optimisation of a type IV composite pressure vessel

by

M.V.R. van Meijel

to obtain the degree of Master of Science
at the Delft University of Technology.

Student number: 4744306

Thesis supervisors:

Ir. R. Barendse,

Dr. J.M.J.F. Van Campen,

Dr. D.M.J. Peeters,

TANIQ, company supervisor

TU Delft, Assistant professor

TU Delft, Assistant professor

This thesis is confidential and cannot be made public until October 11, 2023.



Delft University of Technology
Faculty of Aerospace Engineering
Department of Aerospace Structures and Materials

Graduation Committee

Dated: October 11th, 2021

Chair holder:

Prof. C.A. DransFeld

Committee members:

Dr. ir. O.K. Bergsma

Dr. ir. J.M.J.F. van Campen

ir. R. Barendse

Preface

After a long flight, starting with the hbo Aeronautical engineering in Holland, a pre-master, and subsequently a master's in Aerospace Engineering, I can finally conclude my academic career. My interest in aviation made me leave the beautiful South of the Netherlands, to come to Delft. Looking back at this decision, it may not have been the easiest route, but I am happy to have had this experience and am glad that I pursued a masters to deepen my knowledge about Aerospace engineering even more.

I'm delighted to have had the opportunity to conduct my thesis at TANIQ. This company has a very informal culture, which makes it easy to get to know colleagues and basically have a chat about anything. The daily lunches also have been a nice addition, seeing some colleagues attempting the weirdest combinations of food you can put on a sandwich. I would like to thank Rob Barendse for supervising me during my thesis. Throughout the internship he was always critical about the weekly results I presented, which helped me improving my models and thesis. Due to COVID most of our communication was through teams, but still I had a very nice time in which I learned a lot from him. It was also interesting to work together with Rob to attempt the production of CPV, where he tried every possibility in the book to succeed with the production of the pressure vessel.

I would also like to express my sincere gratitude to my TU Delft supervisor, Julien van Campen. We only met each other face to face during the last phase of my thesis, but nonetheless it has been a real pleasure to have had Julien as my supervisor. Every 2 weeks I was very happy to present him the new results, but Julien always made me think one step further, about what I actually did and why. This has really helped me to improve my skills, but maybe even more important, it helped me to have a critical mindset in whatever I do. He also helped me to be more direct in my communication, which sometimes was not the easiest task. In the latest phase of my thesis he has really supported me to get the most out of myself, and to stay motivated. Finally, as a person he is always friendly and very nice to talk to. I feel grateful to have been able to work together and am very curious how the research about composite pressure vessels will continue at the TU Delft.

Finally, not to be forgotten, I would like to thank my family and friends who more than once needed to hear that I am almost done with my studies and helped and supported me through difficult times. In particular, I want to thank my girlfriend for supporting me in the latest phase of my studies and who kept delaying her very much needed holiday for me to finish the thesis. But finally the big moment is here and we will very much enjoy a short break together.

*M.V.R. van Meijel
Rotterdam (NL), 24 September 2021*

Summary

Filament-wound composite pressure vessels (CPVs) can be used to store hydrogen gas at high pressures. This is required because hydrogen has a low volumetric energy density, which is the amount of energy per unit volume. Thus, to more densely pack the hydrogen atoms, the pressure can be increased to store more hydrogen gas, in a similar volume. This thesis will evaluate a type IV CPV, which consists of a polymeric liner to mitigate any leakage of the gas to the surroundings. This liner is over-wrapped with a fibre-resin system to give strength to the structure. Conventionally, CPVs are manufactured by wet-winding. In this production process, the fibres are wetted in a resin bath prior to being wound on the mandrel, which yields varying material properties. Tow-preg tape has consistent material properties and possibly a higher friction coefficient than wet-winding. However, the cost of tow-preg material is high. Therefore, this thesis aims to understand the mechanical response of an internally pressurised CPV, with the end goal to minimise the amount of material used in a single product.

For the baseline design, an analytical model is constructed, which is used to quickly review the stress-state at the cylindrical section of a CPV. The baseline design will be utilised to observe the weight improvement compared to the optimised design. Traditionally, the netting analysis is used in the preliminary design phase of a CPV. This method neglects the stiffness contribution of the matrix and only uses the strength of the fibres to calculate the required thickness of the hoop and helical layers. However, the shortcoming of this method for thick walled CPVs, is that it only considers membrane forces and no shearing between adjacent plies. Therefore, an analytical model is constructed, which calculates the stresses in every ply, on the cylindrical section of a thick-walled CPV.

A failure criterion is required to assess if a CPV can sustain a defined burst pressure. Following the world-wide failure exercise, the Tsai-Wu and Puck failure criteria showed the highest accuracy, compared to other criteria that were assessed. However, there is no literature available which states all the required information necessary to evaluate which criteria correlates better with experimental results. Therefore, the most conservative failure criterion is chosen: the Tsai-Wu criterion.

The effect of grouping and positioning helical and hoop plies was investigated to observe the effect on the stress-state. The cylindrical section is predominantly loaded in the hoop direction, and the stresses diminish due to the thickness of the CPV, which is characteristic for a thick-walled CPV. To alleviate the hoop strain, hoop plies should be positioned at the inner side of the laminate. The evaluation of the stacking sequence, revealed that interchanging hoop and helical plies yields best performance, i.e. lowest failure index (FI), for the same number of plies. The preliminary design was constructed using this stacking sequence evaluation. An additional 67% laminate thickness was required using the analytical model, as opposed to the netting analysis.

Various element types have been evaluated for their performance in Abaqus. This analysis demonstrates that shell elements, although they require low computational effort, they are not able to capture out-of-plane stresses. Solid elements on the other hand, are able to describe the stresses in the thickness direction, albeit these elements are less computationally efficient. The benefits of both the shell and solid elements are incorporated in the axisymmetric element. This is a solid element which describes a 3D geometry in a 2D plane, which is possible because the stresses remain constant along the circumferential direction. Using the axisymmetric element, a good accuracy is achieved, whilst also minimising computational time. In the FEA model, several in-situ phenomena are defined to more accurately model the mechanical behaviour of a CPV. These can be characterised as a non-geodesic winding angle on the dome, hoop and helical ply drop-off and resin rich areas after a drop-off.

A similar stacking sequence evaluation was performed using the FEA model. This analysis showed a different optimal solution compared to the analytical model. The most efficient stacking sequence is obtained by positioning and grouping all helical plies on the inside of the laminate, and all hoop plies on the outside. This sequence adds more bending stiffness to the laminate by positioning low angle helical plies on the outside of the laminate. It also prevents the inner hoop plies from failing prematurely due to transverse loading.

The final baseline design was constructed using the stacking sequence results. This design required 25% more thickness than the analytical model, which results in a total composite weight of $W = 9.31$ kg. Thus, the FEA model is more conservative than the analytical model. This was expected because the analytical model does not consider the discontinuity stresses present at the dome-cylinder interface.

A surrogate-assisted optimisation framework is created which requires a design of experiment (DOE), to create evenly spaced samples over the design space. This is done using latin hypercube sampling (LHS), which ensures that a sample is created at every row and column of the design space, and no duplicates are present. A surrogate model is used to approximate the behaviour of the FEA model to reduce the computational cost of the optimisation. The Kriging surrogate model is used, which interpolates the input data and a stochastic departure from this result. The input values for the surrogate model are the samples from LHS and calculated FI and weight from the FEA model. The samples are constrained by design bounds, in which helical winding angles can either increase, decrease or be constant through the thickness. The number and position of hoop plies may vary. A genetic algorithm is created, which is an evolutionary stochastic algorithm. These algorithms are used for non-convex design spaces. An initial population is created to examine the design space. The individuals are altered using several operators, such as mutation, crossover and elitism. This procedure attempts to find a global minimum. The result of the surrogate-assisted optimisation, is a reduction of the total composite weight by 13%, as well as a more evenly distributed FI across the thickness of the CPV.

Various literature sources have stated that the friction coefficient of pre-preg tape could be as high as 0.5, while wet-winding only has a friction coefficient of 0.2. An experimental evaluation has been performed to assess the friction coefficient of tow-preg tape. A special mandrel shape is used in which the axial position of the tape is linearly proportional to the friction coefficient. Several deformations were observed during the experiment, such as wrinkling and ply realignment. The experiment showed that the current tape has a friction coefficient of $\lambda = 0.8$. Nonetheless, it is inadvisable to use this value for future computations as several deformations can occur.

Through the use of tow-preg during the production of the CPV, it was shown that re-spooling the material resulted in folds on the Hafner-spool. Once the tape was positioned on the mandrel, loose fibres were present which were pulled off from adjacent layers.

A certifiable CPV should be designed through a combination of numerical models and experimental tests. The numerical models should incorporate characteristics which are present during the design and manufacturing of CPVs, such as non-geodesic winding angle, thickness variation on the dome and void creation. Furthermore, it can be concluded that the viscosity mainly influences FW process parameters. A higher viscosity yields a higher friction coefficient, which enables a bigger design space for helical winding angles and axial position of the hoop ply. A lower width reduces the thickness accumulation on the dome, but also increases production time, given that the same coverage on periphery should be achieved. The analytical model showed simplicity in modelling the CPV. However, although it can predict the stresses at the cylindrical section, it does not consider the stress-state at the dome-cylinder interface. Therefore an additional 25% laminate thickness is required to attain the desired burst pressure. A surrogate-assisted optimisation can be used to approximate the behaviour of the FEA model as well as reduce the material usage in a CPV. This results in a total weight reduction of 13.1%. The stacking sequence of a CPV should be defined by the stress-state at the dome-cylinder interface. To alleviate axial bending stresses, helical plies should be positioned and grouped on the outside to increase the bending stiffness. Hoop plies are required for the hoop stress, and should be positioned at the mid-plane of the laminate.

In this thesis an initial framework has been developed to predict the mechanical response of a CPV and minimise its material usage. However, it is recommended that more CPVs should be produced to better understand their mechanical response. During the production, the thickness build-up at the dome should be reviewed as well as the varying fibre volume fraction and porosity as an effect of the stacking sequence. Following the production, a burst pressure test should be performed, which monitors the strains and out-of-plane displacement to correlate to the FEA model. The current optimisation framework was able to minimise the amount of material. However, a prediction error still remains. This can be mitigated by creating a better DOE, by creating more samples or by reducing the design bounds. The current framework defines FPF as final failure. However, there could be remaining strength after FPF. Therefore a progressive damage model should be constructed. These models disregard failed

plies and increase the internal pressure until final failure. Lastly, the production process should be altered for this specific material, as the material should be directly wound from the bobbin. This can be achieved by a tensioner system, which guides the material through various spools on the mandrel.

Contents

Preface	ii
Summary	iii
Nomenclature	viii
1 Introduction	1
1.1 Project motivation.	1
1.2 Research Objective.	1
1.3 Research questions	2
1.4 Thesis outline.	2
2 Literature review	3
2.1 General CPV design	3
2.1.1 Polymeric liner	4
2.1.2 Polar boss.	5
2.2 Tow-preg properties and characteristics.	6
2.3 Analytical thick walled analysis of CPVs	7
2.4 Failure analysis of composite material.	9
2.4.1 Tsai-Wu failure criterion	10
2.4.2 Puck's failure theory	11
2.5 Filament winding	13
2.5.1 Friction coefficient	14
2.5.2 Winding path	15
2.5.3 Coverage	16
2.5.4 Winding pattern.	17
2.6 Analytical description of the dome thickness	19
2.7 Finite element model	21
2.7.1 Element types	21
2.7.2 Coordinate system	22
2.8 Surrogate modelling	23
2.8.1 Design of experiments	23
2.8.2 Kriging	23
2.9 Evolutionary optimisation algorithms	24
3 Baseline design	26
3.1 Analytical model	28
3.1.1 Stacking sequences	28
3.1.2 Selection of a failure index	29
3.1.3 Evaluation of stacking sequence effect	31
3.1.4 Analytical baseline design	35
3.2 Development of the FEA model	38
3.2.1 Element performance	38
3.2.2 Creation of the FEA geometry	42
3.2.3 Thickness variation on the dome	46
3.2.4 Implementation of non-geodesic winding angle.	48
3.2.5 Mesh convergence analysis	51
3.3 Correlation of the analytical model with FEA	53
3.3.1 Stacking sequence effect	53
3.3.2 Final baseline design	54
3.3.3 General CPV behaviour	58

3.4 Conclusion	62
4 Optimisation framework	64
4.1 Surrogate modelling	64
4.2 Stacking sequence optimisation of a thick-walled CPV	68
4.3 Results and discussion.	69
5 Experimental evaluation	72
5.1 Experimental set-up	72
5.2 Friction experiment of tow-preg tape	74
6 Conclusion	76
7 Recommendations	79
References	84
A Baseline design	85
B Optimised design	88
C Manufacturing defects	91

Acronyms

Abbreviations

Abbreviation	Definition
CFRP	Carbon Fibre Reinforced Plastic
CPV	Composite Pressure Vessel
FEA	Finite Element Analysis
FF	Fibre Failure
FVF	Fibre volume fraction
FPF	First Ply Failure
FW	Filament Winding
GA	Genetic Algorithm
IFF	Inter Fibre Fracture
LPF	Last Ply Failure
NWP	Nominal Working Pressure
TW	TaniqWind
WWFE	World Wide Failure Exercise

Greek symbols

Symbol	Definition	Unit
γ	Shear strain	
ϵ	Strain	-
θ	Angle with respect to the meridian (hoop direction)	rad
λ	Friction coefficient	-
ν	Poisson ratio	-
ρ	Density	$\frac{kg}{m^3}$
σ	Stress	MPa
τ	Shear stress	MPa

Latin symbols

Symbol	Definition	Unit
r	Radial coordinate	mm
R	Cylindrical radius	mm
z	Axial coordinate	mm

1

Introduction

This chapter will provide the motivation of the current research in Section 1.1. From the project motivation several research questions are defined to substantiate the research objective. Lastly, the outline of the thesis is presented in Section 1.4

1.1. Project motivation

Due to an ever growing demand in sustainable transportation, there is an increased need for the development of hydrogen as an energy carrier. Based on mass, hydrogen contains about three times as much energy than conventional gasoline¹. However, the volumetric energy density, which is the amount of energy per volume unity, is much lower for hydrogen. Therefore it needs be stored either at cryogenic temperatures or at hyperbaric pressure. The most common nominal working pressures (NWP) for hydrogen are either 350 or 700 bar. Because of these excessive pressures, the composite pressure vessels (CPVs) require to become thick-walled. This makes the out-of-plane stress components significant which requires calculation models that take into account these effects. Also, the material of CPVs account for around 60% [47], which support the need to minimise the material usage.

This thesis evaluates whether the use of tow-preg material could possibly reduce the amount of material necessary to attain a predefined burst pressure. Currently, the production of CPVs is mainly executed using wet-winding. The use of this process results in varying material properties due to differences in fibre volume fraction. Also, the friction coefficient is minimal, because the resin has a low viscosity. This friction is required for the production of winding paths, which deviate from the traditional geodesic angle. On the other hand, tow-preg material introduces constant material properties and possibly an elevated friction coefficient. This friction coefficient provides an opportunity to vary the winding angle through the thickness, by which the material strength can be made more uniform in every lamina. However, the challenge during the design and production of CPVs is that several effects are present which alter the mechanical response [35], such as varying stiffness on the dome-cylinder interface, non-geodesic winding angle on the dome and resin-rich areas. This thesis will attempt to describe the behaviour of the CPV, by including several phenomena in numerical models to minimise the material usage.

1.2. Research Objective

This thesis is focused on developing a calculation framework which is able to accurately describe the mechanical response of a CPV, to minimise the material usage. Current research has been focusing on geodesic winding paths [57, 42], which are winding paths that do not require friction. However the usage of tacky pre-preg tape could result in a new design space for the optimisation of a CPV, by using non-geodesic winding paths. Thus, to explore the analytical and experimental optimisation procedure of a CPV for the storage of gaseous hydrogen the following research objective is proposed:

¹<https://www.energy.gov/eere/fuelcells/hydrogen-storage>

Within the time period of the thesis, the objective is to create a design strategy in which the possibilities of using pre-impregnated tows are reviewed to minimise the required material to withstand burst pressure, by creating an optimisation framework which evaluates the stresses and strains in a thick-walled composite pressure vessel used for storing gaseous hydrogen.

1.3. Research questions

To ensure the feasibility of the proposed research objective, several questions are introduced to subdivide the problem. The main research question of this thesis is:

How to design a certifiable type IV pressure vessel using pre-impregnated tow-fibres minimising structural weight and cost?

To substantiate the research question, several sub-questions are defined to substantiate the main research question:

1. *Which properties of pre-impregnated tow-fibres impact the filament winding process in what way?*
2. *To what degree of accuracy can an analytical approach be used to predict the stress distribution in a pressurised CPV?*
3. *What is a suitable optimisation strategy for the design of CPVs?*
4. *How does the loading of a CPV influence the design of the lay-up used?*

1.4. Thesis outline

In Chapter 2 an outline of the utilised theory is presented, which will be used throughout this thesis. A preliminary design will be constructed in Chapter 3, using both an analytical method and a numerical model. Both models will be correlated to observe discrepancies in the solutions. Following this, using the designs from the previous chapter, a surrogate-assisted optimisation will be performed in Chapter 4 to minimise the material usage in a CPV and optimise the strength through the thickness. The results from a friction experiment are reviewed in Chapter 5. Ultimately, based on the research questions, the report will provide a conclusion, and finally some recommendations are proposed for further research.

2

Literature review

This chapter will serve as a preliminary literature review on the design and optimisation of CPVs. First the design of a current CPV will be highlighted in Section 2.1. In Section 2.2 the utilised material will be reviewed. Section 2.3 presents the analytical model, which is used to calculate the stresses and strains in a thick-walled CPV. Section 2.4 describes the most commonly used criteria to describe failure for CPVs. The filament winding (FW) process is explained in Section 2.5. The winding on the dome imposes some boundary conditions which results in significant thickness build-up on the dome and an analytical model to describe this thickness build-up is described in Section 2.6. Besides the analytical model, an FEA model is constructed to evaluate the more intricate stress-state on the dome. In Section 2.7 several element types in Abaqus are reviewed for their formulation. Lastly, in Section 2.8 and Section 2.9 basic knowledge is provided to construct a meta-model and to subsequently use it with a genetic algorithm.

2.1. General CPV design

The standard layout of a CPV consist of a polymeric liner, metal boss and a composite overwrap, which is characterised as a type IV pressure vessel. The liner is provided by the German research institute Fraunhofer, which collaborates with TANIQ in the DaQoTa project. The goal of this project is to investigate the design of a CPV, which is produced using thermoplastic tape placement. Unlike the current thesis, where thermoset tow-preg tape will be utilised. The geometry of the liner is depicted in Figure 2.1. The total length of the CPV is 841 mm and the external diameter of the polymeric liner is 314 mm. This results in an internal storage volume of 52 litres. Furthermore, the outside of the dome has an elliptical shape with a semi-major axis of 157 mm and a semi-minor axis of 94.27 mm.

Furthermore, it has been reported by Fraunhofer that the boss part and the polymeric part release at circa 40 MPa. Therefore the burst pressure of the current thesis is reduced to 35 MPa in order to mitigate undesirable failure. Using this pressure, 35 MPa, the storage capability of the CPV will be¹:

$$m_{hydrogen} = \rho_{hydrogen} \left[\frac{kg}{m^3} \right] * V_{CPV} [m^3] = 1.2 [kg] \quad (2.1)$$

where the density of hydrogen is determined at 35 MPa at 25 °C.

¹<https://h2tools.org/hyarc/hydrogen-data/hydrogen-density-different-temperatures-and-pressures>

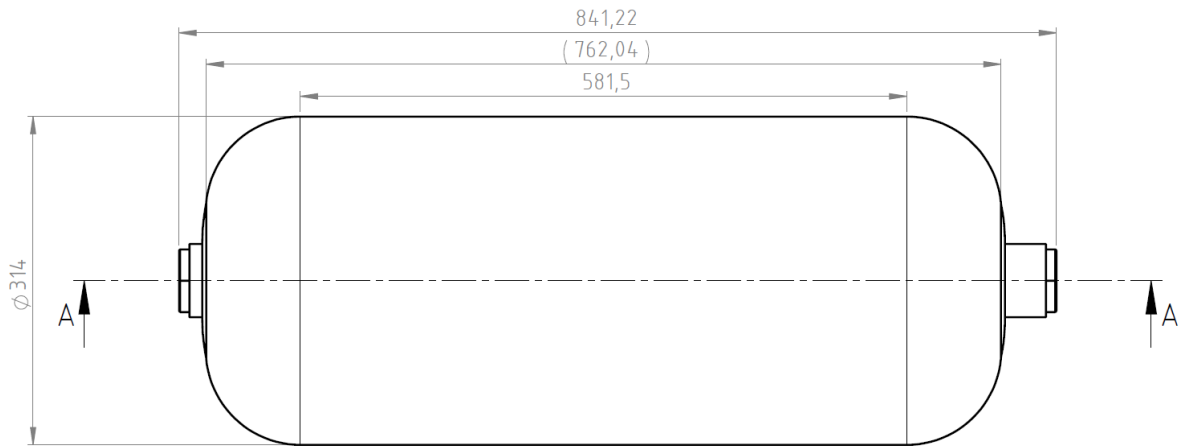


Figure 2.1: Geometry of the liner, obtained from technical drawing of the DaQoTa project

The dome section has an elliptical shape and can be parametrised accordingly to Equation 2.2.

$$\frac{(r - h)^2}{R^2} + \frac{z^2}{b^2} = 1 \quad (2.2)$$

where r and z are the radial and axial position respectively, and R and b are the semi-major and the semi-minor axis of the ellipsis, respectively. In the FEA model the polar boss will be located on the symmetry axis, therefore the definition of the ellipse is off-centre by h , which is 35 mm.

2.1.1. Polymeric liner

The purpose of the liner is to create an impermeable barrier for the internal gas. The polymeric liner is a distinct feature of the type IV CPV. This type of liner has originated due to the need to reduce the weight of pressure vessels but is characterised by a low stiffness and reduced permeation arrest. By using a polymeric liner instead of the original metal liner the density can be reduced up to three fold (aluminum alloy vs PA-6) [50]. However, polymeric liners are much more prone to permeation of the internal gas as opposed to metal liners. This mainly occurs due to the free volume being present in polymers [15]. The permeation rate at 35 MPA is about $400 \text{ wt} \cdot \text{ppm}$, for a pressurisation time of 5 minutes, which is the weight of the penetrated hydrogen per unit of the liner weight in parts per million. As is observed from Figure 2.2, an increase in pressure also leads to an elevated permeation rate.

Table 2.1: Mechanical properties of the PA6 liner

	Units	Values
E	MPa	2950
ν_{12}	-	0.3
$\sigma_{tensile, strength}$	MPa	100
ρ	$\frac{\text{kg}}{\text{m}^3}$	1300

For a type IV CPV, the main functionality of the liner is to block permeation of the hydrogen gas to the ambient air. Therefore, it usually has a low stiffness and thus low load-bearing capability. Some publications neglect the presence of the liner in the calculation models [35, 54, 36], because of its minimal stiffness and thus low contribution to the structural strength. The mechanical properties of PA-6 in are shown in Table 2.1². The inner radius of the liner at the cylindrical part is 152 mm and the outer radius 157 mm, resulting in a 5 mm thickness of the liner.

The production of polymeric liners is usually performed by rotation molding (roto-molding). Here a metal mould is heated and the polymer is inserted. After this the mould is rotated and the polymer conforms to the mould shape. Upon cooling the polymer consolidates (thermoplast) [34].

²https://www.substech.com/dokuwiki/doku.php?id=thermoplastic_polyamide_nylon_6

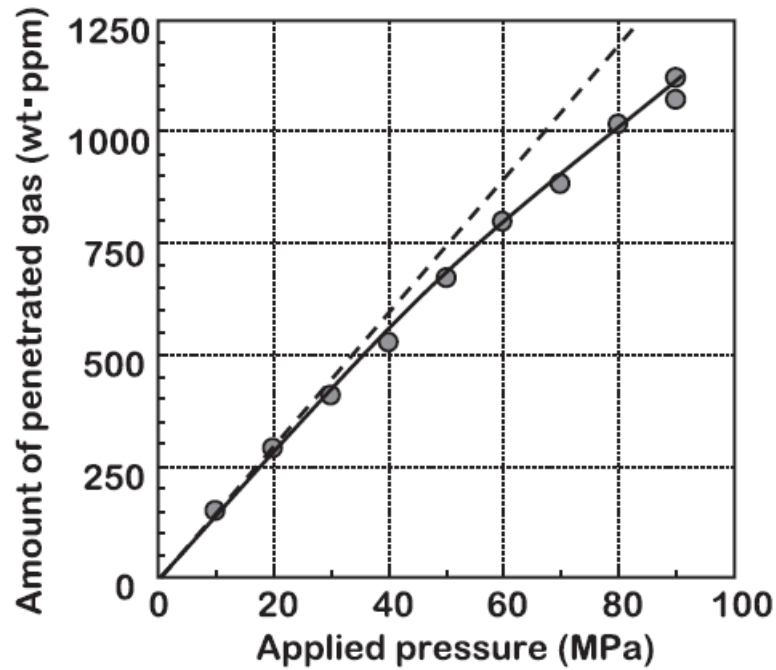


Figure 2.2: Pressure dependency on the amount of penetrated gas using a HDPE liner [15]

2.1.2. Polar boss

The goal of the boss is to provide a means of connection. Here it is important that the polar boss and liner provide a seal, such that no gas may escape. Furthermore, the stress state due to the internally applied pressure at the boss section is very intricate, which makes it difficult to assess failure at this section. Also, if the composite in the boss area fails it may be possible that boss blow-out could occur, with serious consequences for the environment outside surrounding the CPV [27]. A more in-depth discussion will be given in Chapter 3. The current pressure vessel has a stainless steel boss, weighing 1.4 kg per boss and the mechanical properties are shown in Table 2.2³.

Table 2.2: Mechanical properties of the stainless steel boss

	Units	Values
E	GPa	190
ν_{12}	-	0.265
$\sigma_{yield,strength}$	MPa	2500
ρ	$\frac{kg}{m^3}$	7480

³https://www.engineeringtoolbox.com/young-modulus-d_417.html

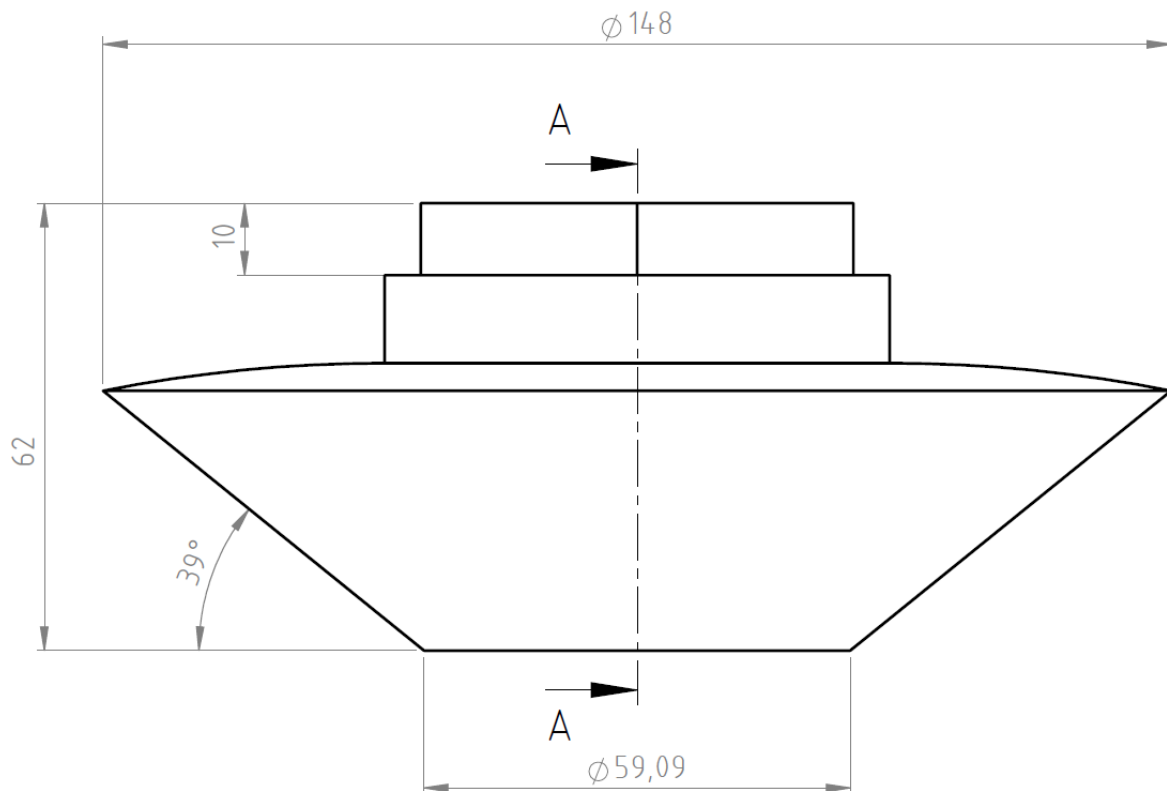


Figure 2.3: Technical drawing of the stainless steel boss, obtained from technical drawing of the DaQoTa project

2.2. Tow-preg properties and characteristics

A type IV CPV has a polymeric liner and is over-wound with a composite. The composite consists of two main parts, namely the fibre and matrix. Here the fibre has the most impact on the mechanical behaviour of the composite. The fibre of choice in the design of a CPV is usually carbon fibre due to modulus-to-density ratio and strength-to-density ratio [59]. Furthermore, the epoxy or matrix acts as a bond between the layers of fibres. The most commonly used is a thermoset matrix, which is also the cheapest. The role of the matrix is to keep the bundle of fibres together and transfer the load to the fibres. As opposed to thermoplastic resins, thermoset resins have a low viscosity at room temperature which makes processing easier. However, thermoplastic can be reheated and reshaped [9].

Currently, most CPVs are being produced using wet-winding, in which the fibres are wetted in a matrix prior to being applied on the mandrel. Here, the fibre and resin system should be stored separately, usually at room temperature. However, the current thesis will be using pre-impregnated (pre-preg) tape. Here, unidirectional (UD) fibres are impregnated with a B-stage resin. In this stage, the resin is still soft and tacky and no crosslinks are being created [34]. This enables storage of tow-preg tape for a longer period of time at room temperature. The shelf life can be increased to 12 months by storing the tow-preg at $-18\text{ }^{\circ}\text{C}$. Another advantage of pre-preg is the more consistent mechanical properties, because the fibre volume can be better controlled as opposed to wet-winding. However, pre-preg is more expensive, around 1.5 times [13], as opposed to wet-winding, which could make the production of a CPV with pre-preg less economic interesting. The effect the properties have on the friction coefficient will be discussed in Section 5.2.

Table 2.3: Mechanical properties of the composite

	Units	Values
E_1	GPa	151.6
E_2	GPa	8.63
G_{12}	GPa	4.84
ν_{12}	-	0.37
ν_{23}	-	0.52
X_t	MPa	2315.1
Y_t	MPa	78.7
X_c	MPa	1620.9
Y_c	MPa	200
S	MPa	77.4
ρ_{CFRP}	$\frac{kg}{m^3}$	1520
t_{ply}	mm	0.33
w_{tape}	mm	5
V_f	%	60

The utilised composite is an ITS50 (24K filaments) carbon fibre with a Hexion epoxy resin, shown in Table 2.3. The through thickness Poisson ratio, ν_{23} , is very difficult to obtain through experimental test, therefore the value from Nebe et al [35] will be used. Furthermore, the datasheet provided by the material supplier did not contain Y_c . Therefore the value provided from Daniel [12] is used for all calculations.

2.3. Analytical thick walled analysis of CPVs

The analysis of thin-walled CPVs reduces the complexity of the stress-state into two dimensions, i.e. plane stress. Here the in-plane axial and hoop stress at the cylindrical section can be calculated as follows [50]:

$$\sigma_{hoop} = \frac{PR}{t} \quad \sigma_{axial} = \frac{PR}{2t} \quad (2.3)$$

where P is the pressure, R is the radius of the cylinder and t is the wall thickness. From these equations it can be observed that the hoop to axial ratio equals 2:1. For netting analysis, the contribution of the matrix is neglected during the analysis. Therefore the stresses in the fibres can be calculated by:

$$\sigma_{hoop} = \sigma_f \sin^2 \alpha \quad \sigma_{axial} = \sigma_f \cos^2 \alpha \quad (2.4)$$

By setting the hoop to axial ratio to 2, the well-known optimum winding angle can be computed:

$$\frac{\sigma_{hoop}}{\sigma_{axial}} = \tan^2 \alpha = 2 \quad (2.5)$$

$$\alpha = \tan^{-1} \sqrt{2} = 54.7^\circ$$

In reality this winding angle is rarely used for CPVs, because the performance of the structure is heavily affected by slight deviations from this angle. Also, this angle only applies for infinitely long thin cylinders. While, usually a CPV is closed by domes, which imposes additional boundary conditions and discontinuity stresses.

Various attempts have been made to make an analytical description of a thick-walled composite cylinder. The first well known description of an anisotropic cylindrical shell was made by Lekhnitskiy [28]. His method stacked multiple shells and imposed continuity conditions at surfaces of the shells. Through this the radial stresses should match with adjacent shells. The limitation of this method is that it does not impose any boundary conditions at the end of the cylinder. Thus it simulates an infinite cylinder, which is a non-conservative assumption. Because it does not take into account the discontinuity stresses generated at the dome-cylinder interface.

Tsai continued the works from Lekhnitskiy by imposing a constant strain in the axial direction, while Lekhnitskiy used a zero strain [45]. However, the meridional bending, imposed by the domes, has been neglected. Tsai used a progressive damage model to simulate the burst pressure. The model is based on the Tsai-Wu failure criterion, described in Section 2.4. Here, the stiffness properties of a lamina are degraded if the failure index (FI) exceeds 1.

Furthermore, results showed that the stresses/strains started to deviate from an external-to-internal radius ratio of 1.1 and higher [36, 39], or similarly for a ratio of $\frac{R}{t} < 10$. In the case of the present thesis, this requires the laminate thickness to be $(152 * 1.1) - 5 - 152 = 10.2 \text{ mm}$, which is obtained by multiplying the inner radius with 1.1 and subtracting the inner radius and liner thickness. Continuing, Tsai suggests increasing the winding angle of plies which have a low failure index, to improve the load distribution through the thickness.

In this thesis the analytical tool developed is based on works from Zu [59], Xia [54] and Park et al [38]. Prior to the analysis some assumptions are made to reduce the complexity:

- Stresses do not change in the hoop direction, i.e. $\frac{\delta}{\delta\theta} = 0$
- The helical plies act as a homogenous orthotropic unit
- Only the in-plane shear stress is considered non-zero, i.e. $\tau_{rz} = \tau_{r\theta} = \tau_{z\theta} = 0$
- The effect of the interlaminar shear modulus is negligible with respect to the modulus in the fibre direction
- Similar to Tsai, a generalised plane-strain condition is assumed, i.e. constant axial strain, because according to Saint-Venant's principle the discontinuity stresses only exists at sections close to the domes

The full derivation can be found at [59], [60] or [54]. However, the latter does not consider the presence of an isotropic liner, while the current analysis does.

The stresses in a single lamina can be calculated using the following equation:

$$\begin{pmatrix} \sigma_z \\ \sigma_\theta \\ \sigma_r \\ \tau_{z\theta} \end{pmatrix}^k = \begin{bmatrix} H_Z & I_Z & J_Z & K_Z \\ H_\theta & I_\theta & J_\theta & K_\theta \\ H_r & I_r & J_r & K_r \\ H_{z\theta} & I_{z\theta} & J_{z\theta} & K_{z\theta} \end{bmatrix}^k \begin{pmatrix} \epsilon_0 \\ D_1^k r^{\beta^k - 1} \\ D_2^k r^{\beta^k - 1} \\ \gamma_0 r \end{pmatrix}^k \quad (2.6)$$

where $\sigma_z, \sigma_\theta, \sigma_r, \tau_{z\theta}$ are the axial, hoop, radial and in-plane shear stress, respectively. The components (H, I, J, K) are described in [59]. The stresses in the liner can be computed in a similar fashion, shown in Equation 2.7.

$$\begin{pmatrix} \sigma_z^L(r) \\ \sigma_\theta^L(r) \\ \sigma_r^L(r) \\ \tau_{z\theta}^L(r) \end{pmatrix} = \frac{E}{(1-2\nu)(1+\nu)} \begin{bmatrix} 1-\nu & 2\nu & 0 & 0 \\ \nu & 1 & 1-2\nu & 0 \\ \nu & 1 & 2\nu-1 & 1 \\ 0 & 0 & 0 & \frac{1-2\nu}{2} \end{bmatrix} \begin{pmatrix} \epsilon_0 \\ D_1^L \\ \frac{D_2^L}{r^2} \\ \gamma_0 r \end{pmatrix} \quad (2.7)$$

where E is the young's modulus of the isotropic liner, ν is the in-plane Poisson's ratio of the liner.

To determine the unknown integration constants in Equation 2.6 and Equation 2.7, a system of algebraic equations should be solved. This system depends on the number of plies present in the structure. In this example, a two ply system is solved. This is done to reduce complexity of the algebraic system. For more plies the system can be expanded by adding more rows sequentially.

$$\begin{pmatrix} D_1^L \\ D_1^{(1)} \\ D_1^{(2)} \\ D_2^L \\ D_2^{(1)} \\ D_2^{(2)} \\ \epsilon_0 \\ \gamma_0 \end{pmatrix} = \begin{bmatrix} d_{11} & 0 & 0 & e_{11} & 0 & 0 & a_{11} & 0 \\ d_{21} & d_{22} & 0 & e_{21} & e_{22} & 0 & a_{21} & a_{22} \\ 0 & d_{32} & d_{33} & 0 & e_{32} & e_{33} & a_{31} & a_{32} \\ d_{41} & d_{42} & 0 & e_{41} & e_{42} & 0 & a_{41} & a_{42} \\ 0 & d_{52} & d_{53} & 0 & e_{52} & e_{53} & a_{51} & a_{52} \\ 0 & 0 & d_{63} & 0 & 0 & e_{63} & a_{61} & a_{62} \\ f_{01} & f_{02} & f_{03} & 0 & f_{05} & f_{06} & f_{07} & f_{08} \\ 0 & g_{02} & g_{03} & 0 & g_{05} & g_{06} & g_{07} & g_{08} \end{bmatrix}^{-1} \begin{pmatrix} -p \\ 0 \\ 0 \\ 0 \\ 0 \\ 0 \\ \frac{pr_a^2}{2} \\ 0 \end{pmatrix} \quad (2.8)$$

The matrix can be expanded adding more rows below $D_1^{(2)}$ and $D_2^{(2)}$ for n plies. In which each subsequent row is shifted to the right and one down. Through this continuity of the stresses is ensured at the boundaries of each lamina. Following this, as is observed besides the continuity equations for the liner and composite, two additional compatibility equations are required to solve the algebraic system for n plies. The first equations states that the axial stress in the liner and in each ply should equal the circumferential stress due to the internal pressure, as depicted in Equation 2.9.

$$2\pi \left(\int_{r_a}^{r_b} \sigma_z^L(r) r dr + \sum_{k=1}^n \int_{r_{k-1}}^{r_k} \sigma_z^{(k)}(r) r dr \right) = \pi p r_a^2 \quad (2.9)$$

Furthermore, a zero-twisting condition is imposed, which is required to obtain the unknown twisting coefficient. This condition is described as follows:

$$2\pi \left(\sum_{k=1}^n \int_{r_{k-1}}^{r_k} \tau_{z\theta}^{(k)}(r) r^2 dr \right) = 0 \quad (2.10)$$

With the given sets of equations, the stresses and strains can be computed at each location of the isotropic liner and orthotropic laminate, for n plies. However, to assess the quality of the laminate, a failure criteria should be employed to assess failure in any of the plies. To predict failure in a ply, the stresses should be transformed from the global coordinate system (r, z, θ) to the local system $(1, 2, 3)$ of the lamina as follows:

$$\sigma_{loc} = [T] \sigma_{global} \quad (2.11)$$

where the rotation matrix and the global stress matrix are given below [59]:

$$\begin{Bmatrix} \sigma_1 \\ \sigma_2 \\ \sigma_3 \\ \tau_{12} \end{Bmatrix} = \begin{bmatrix} \cos^2\theta & \sin^2\theta & 0 & 2\cos\theta\sin\theta \\ \sin^2\theta & \cos^2\theta & 0 & -2\cos\theta\sin\theta \\ 0 & 0 & 1 & 0 \\ -\sin\theta\cos\theta & \sin\theta\cos\theta & 0 & \cos^2\theta - \sin^2\theta \end{bmatrix} \begin{Bmatrix} \sigma_z \\ \sigma_\theta \\ \sigma_r \\ \tau_{z\theta} \end{Bmatrix} \quad (2.12)$$

Here, θ is the fibre orientation.

2.4. Failure analysis of composite material

As already indicated in Section 2.3, after the stress state is known in a CPV, it should be evaluated for failure. For composites this can be subdivided in to first ply failure (FPF) and last ply failure (LPF). Here, FPF indicates that either the matrix or the fibre, at any location, has exceeded the failure index of 1. Contrary, using a LPF approach, the initial failure (FPF) results in degradation of that location, reducing the load-bearing capability. This reduction of stiffness is performed until the analysis diverges, which implies final failure and no load-bearing capability. As indicated by Tsai et al [45], a more efficient laminate can be obtained by creating a uniform failure index through the thickness. This can be achieved by altering the winding angles. By achieving a uniform failure index through the thickness, failure of the structure should be close to FPF. This would indicate that all layers are loaded optimal, possibly minimising the weight. In this research FPF will be considered as final failure of the CPV. Because first it should be evaluated how a static analysis influences the design of a CPV and what characteristics of a CPV should be incorporated in the calculation models to obtain an accurate result, with respect to a burst pressure test.

This chapter will provide an overview of two different failure criteria. These have been chosen based on the World Wide Failure Exercise (WWFE) [17, 1] and their use in various publications, validating their correlation to numerical models. However, in the WWFE it is indicated that there remains significant doubt in any of the available criteria and that the definition for failure varies throughout. Here, the first statement will be validated and the second will be defined as that the failure-index of either the fibre or matrix has exceeded 1 will result in failure. In all of the 19 presented loading cases Tsai-Wu and Puck showed the best correlation to test results.

It should be noted that a failure criteria is an approximation of reality. Therefore it is also important to observe the correlation with respect to analytical and numerical models to experimental test. This will be further reviewed in Section 3.3.1.

2.4.1. Tsai-Wu failure criterion

This criteria is defined as a quadratic interaction criterion [49]. The general form of such a criteria is indicated below:

$$F_{ij}\sigma_i\sigma_j + F_i\sigma_i = 1 \quad (2.13)$$

where F_{ij} and F_i are the strength parameters (different for each quadratic criteria) and $\sigma_{i,j}$ are the stress components for $i,j = 1,2,..6$. In the WWFE it was shown that this criterion had very good predictive capabilities, especially for unidirectional (UD) laminate. However, especially in the bi-axial compression area, the prediction is poor (unconservative), as shown in Figure 2.4. Also, initial failures are not predicted accurately, while final failure is. Here, initial failure or first ply failure (FPF) is characterised by either failure of the matrix or fibre of a single ply. While final failure or last ply failure (LPF) is obtained by degrading the properties of a failed ply, until the last ply fails. Most of the prediction performed showed to be conservative with respect to the test data provided in the WWFE, in particular Tsai-Wu.

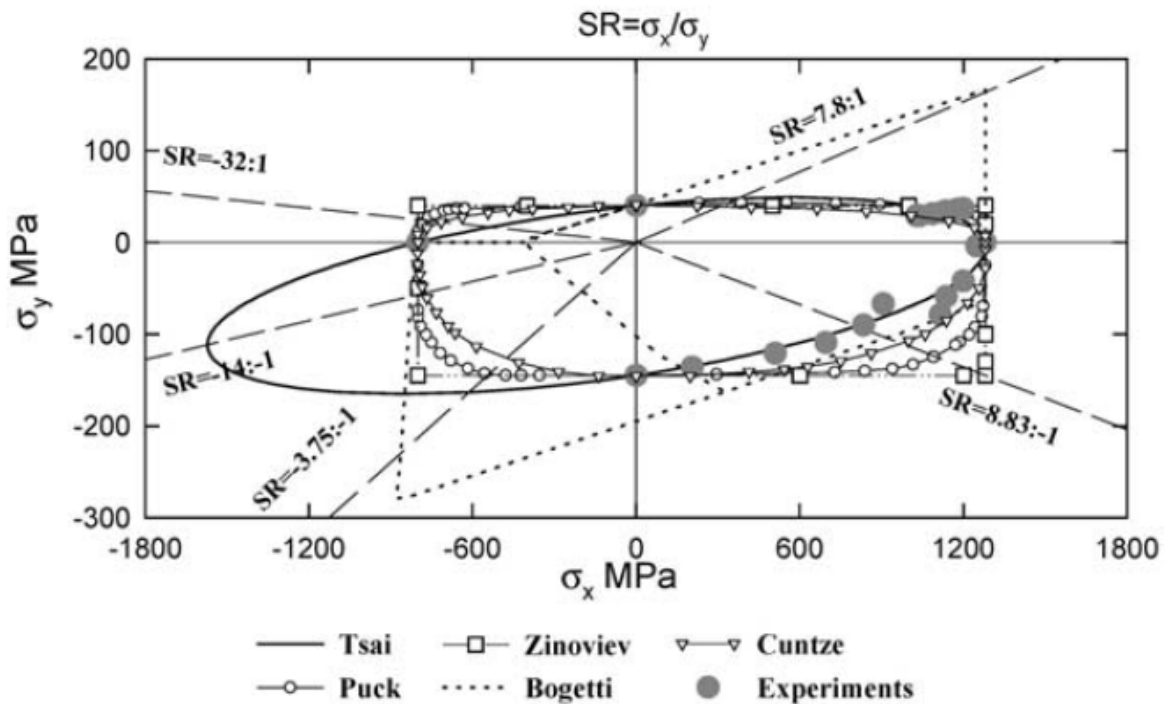


Figure 2.4: Various failure criteria assessing the failure index for a bi-axial loading case, for a UD glass fibre epoxy [48]

However, with-all Tsai-Wu shows good correlation to experimental results reviewed in the WWFE. This is because these types of failure criteria are curve-fitted to empirical data [59], by adjusting the strength parameters, which are related to UD lamina strengths. Because this criteria is invariant it can also be readily applied to a cylindrical coordinate system used in this thesis. However, this failure criteria, or any quadratic interaction criterion, does not distinguish between matrix or fibre failure, which might be useful for degrading properties in progressive failure analysis.

In this thesis an orthotropic material system is used, with the 2-3 axis being the isotropic plane. Also, the change of sign in shear stress, will not alter the failure stress [12, 49]. With these assumption some strength parameters can be discarded. These are shown below [59]:

$$F_4 = F_5 = F_6 = F_{45} = F_{56} = F_{46} = F_{14} = F_{15} = F_{16} = F_{24} = F_{25} = F_{26} = F_{34} = F_{35} = F_{36} = 0 \quad (2.14)$$

The Tsai-Wu failure criteria in a 3D space can be described by expanding Equation 2.13 and neglecting the terms indicated in Equation 2.14. Then failure can be described if the following equation equals one [12, 38]:

$$F_1\sigma_{11} + F_2(\sigma_{22} + \sigma_{33}) + F_{11}\sigma_{11}^2 + F_2(\sigma_{22}^2 + \sigma_{33}^2) + 2F_{12}\sigma_{11}(\sigma_{22} + \sigma_{33}) + 2F_{23}\sigma_{22}\sigma_{33} + 2(F_{22} - F_{23})\tau_{23}^2 + F_{66}(\tau_{12}^2 + \tau_{13}^2) = 1 \quad (2.15)$$

where the strength parameters are defined as:

$$\begin{aligned}
 F_1 &= \frac{1}{X^t} - \frac{1}{X^c}, & F_2 &= \frac{1}{Y^t} - \frac{1}{Y^c}, \\
 F_{11} &= \frac{1}{X^t X^c}, & F_{22} &= \frac{1}{Y^t Y^c}, \\
 F_{12} &= -\frac{1}{2\sqrt{X^t X^c Y^t Y^c}}, & F_{23} &= \frac{1}{2\sqrt{Y^t Y^c}}, \\
 F_{66} &= -\frac{1}{S^2}
 \end{aligned} \tag{2.16}$$

However, in the analytical method the through thickness shear stresses are not computed and the expected failure is usually intra-laminar, i.e. fibre fracture and matrix cracking [59]. Therefore, Equation 2.15 can be reduced to:

$$F_1 \sigma_{11} + F_2 (\sigma_{22} + \sigma_{33}) + F_{11} \sigma_{11}^2 + F_2 (\sigma_{22}^2 + \sigma_{33}^2) + 2F_{12} \sigma_{11} (\sigma_{22} + \sigma_{33}) + 2F_{23} \sigma_{22} \sigma_{33} + F_{66} \tau_{12}^2 = 1 \tag{2.17}$$

This equation should be computed for every location and every single lamina, to determine if any location has exceeded the value 1. It is imported to note that the stresses should be transformed into the local ply coordinates prior to assessing the failure index, as shown in Equation 2.12.

2.4.2. Puck's failure theory

This theory is based on the phenomenological behaviour of a lamina at a three-dimensional micro-mechanical level and based on the Mohr-Coulomb fracture hypothesis. The latter states that fracture is influenced only by the stresses acting on that fracture plane (fp), or action plane as termed in Puck's theory and illustrated in Figure 2.5. It has been developed by Puck and Schürmann [22].

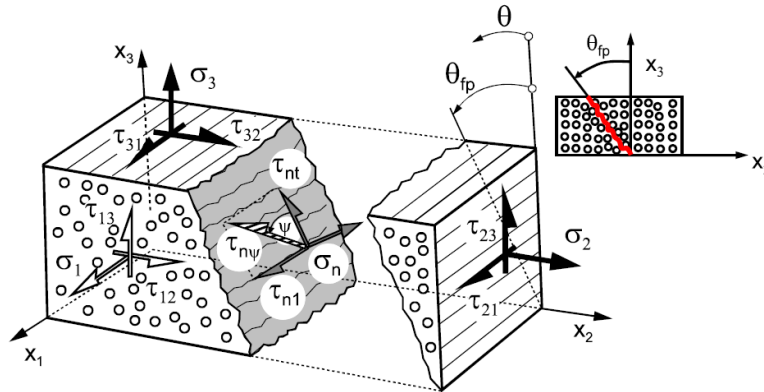


Figure 2.5: The action plane of the stresses rotated along the fracture angle [22]

The theory consist of five different failure modes, of which two are designated to fibre failure (FF) and three to the inter-fibre failure (IFF). For the latter different forms are possible, as shown in Figure 2.6. The most common forms of IFF for CPV are the transverse tension and longitudinal shear [22]. These result in straight cracks parallel to the action plane. However, these types of cracks are only created during the initial pressurisation and do not lead to final failure. This is because areas with a growing crack still have a load-bearing capability. Thus it can be seen as an area with reduced stiffness.

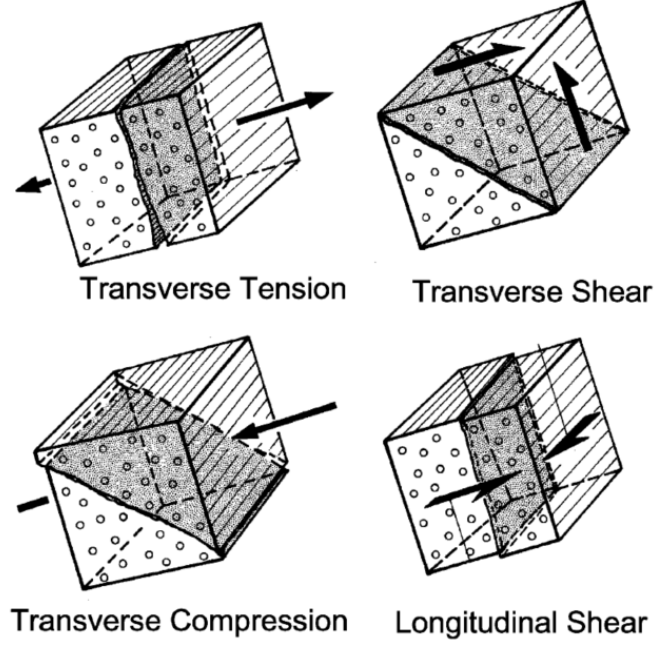


Figure 2.6: Different forms of IFF [22]

The stresses acting on the fracture plane can be calculated as follows:

$$\begin{aligned}\sigma_n(\theta) &= \sigma_2 \cos^2 \theta + \sigma_3 \sin^2 \theta + 2\tau_{23} \cos \theta \sin \theta \\ \tau_{nt}(\theta) &= -\sigma_2 \cos \theta \sin \theta + \sigma_3 \sin \theta \cos \theta + 2\tau_{23} (\cos^2 \theta - \sin^2 \theta) \\ \tau_{n1}(\theta) &= \tau_{31} \sin \theta + \tau_{12} \cos \theta\end{aligned}\quad (2.18)$$

Compared to other failure criterion's, Puck's method employs a different notation for the strength parameters, as shown in Equation 2.19, which should all be positive.

$$\begin{aligned}R_{\parallel}^t &= X^t, & R_{\parallel}^c &= X^c, \\ R_{\perp}^t &= Y^t, & R_{\perp}^c &= Y^c, \\ R_{\perp\perp} &= S\end{aligned}\quad (2.19)$$

The first failure type described is the fibre failure, as shown in Equation 2.20. This failure type is based on the maximum stress criterion and is regarded as final failure for a lamina. Through this, it is linked with the tensile strength of the fibre in the matrix.

$$f_{EFF} = \frac{1}{\pm R_{\parallel}^{t,c}} \left[\sigma_1 - \left(\nu_{\perp\parallel} - \nu_{\perp\parallel f} m_{\sigma f} \frac{E_{\parallel}}{E_{\parallel f}} \right) (\sigma_2 + \sigma_3) \right] \quad (2.20)$$

where $m_{\sigma f} = 1.1$ for CFRP [29], which is the mean magnification factor for transverse stresses. Based on the sign of σ_1 , $R_{\parallel}^{t,c}$ should be tensile or compressive and positive or negative, respectively. Furthermore, $\nu_{\perp\parallel f}$ and $E_{\parallel f}$ are the in-plane Poisson ratio and the longitudinal Young's modulus of the fibre, respectively.

The most extensive part of Puck's failure criteria is the IFF, highlighted in Equation 2.21 - Equation 2.23 [22, 29]. These modes are based on experimental evidence and the interaction of stresses. As opposed to FF, IFF is characterised by macroscopic cracks which grow parallel to the fibre direction and are preceded by micro-mechanical cracks.

for $\sigma_n \geq 0$

$$f_{EIFF}(\theta) = \sqrt{\left[\left(\frac{1}{R_{\perp}^{AT}} - \frac{p_{\varphi}^t}{R_{\perp\varphi}^A} \right) \sigma_n(\theta) \right]^2 + \left(\frac{\tau_{nt}(\theta)}{R_{\perp\perp}^A} \right)^2 + \left(\frac{\tau_{n1}(\theta)}{R_{\perp\parallel}^A} \right)^2} + \frac{p_{\parallel\varphi}^t}{R_{\perp\varphi}^A} \sigma_n(\theta) \quad (2.21)$$

for $\sigma_n < 0$

$$f_{E\ IFF}(\theta) = \sqrt{\left[\left(\frac{p_{\perp\varphi}^c}{R_{\perp\varphi}^A}\right) \sigma_n(\theta)\right]^2 + \left(\frac{\tau_{nt}(\theta)}{R_{\perp\perp}^A}\right)^2 + \left(\frac{\tau_{n1}(\theta)}{R_{\perp\parallel}^A}\right)^2} + \frac{p_{\parallel\varphi}^c}{R_{\perp\varphi}^A} \sigma_n(\theta) \quad (2.22)$$

where

$$\begin{aligned} \frac{p_{\perp\varphi}^{t,c}}{R_{\perp\varphi}^A} &= \frac{p_{\perp\perp}^{t,c}}{R_{\perp\perp}^A} \cos^2\varphi + \frac{p_{\perp\parallel}^{t,c}}{R_{\perp\parallel}^A} \sin^2\varphi, \\ \cos^2\varphi &= 1 - \sin^2\varphi = \frac{\tau_{nt}^2}{\tau_{nt}^2 + \tau_{nt}^2}, \\ R_{\perp\perp}^A &= \frac{R_{\perp}^c}{2(1 + p_{\perp\perp}^c)} \end{aligned} \quad (2.23)$$

The inclination parameters, $p_{\perp\parallel}^t, p_{\perp\perp}^c, p_{\perp\perp}^{t,c}$, equal 0,3, 0.35, 0.3 for a carbon fibre [29, 22], respectively. Following this, the IFF-criteria is similar to Hashin, namely that stresses acting on the fracture surface promote fracture. Puck extended this by transforming the stresses to the fracture plane. As stated in Equation 2.18, the stresses depend on the angle θ . To find the decisive fracture plane, a numerical approach should be employed to calculate the stress exposure between $90 \leq \theta \leq 90^\circ$. Here, the stress exposure is defined as the plane with the highest risk of fracture. An example of the variation of the stress exposure is shown in Figure 2.7. Here, the blue lines are the inner plies and the red lines the outer plies. It can be observed that the maximum exposure for an internally pressurised pressure vessel is at 34° .

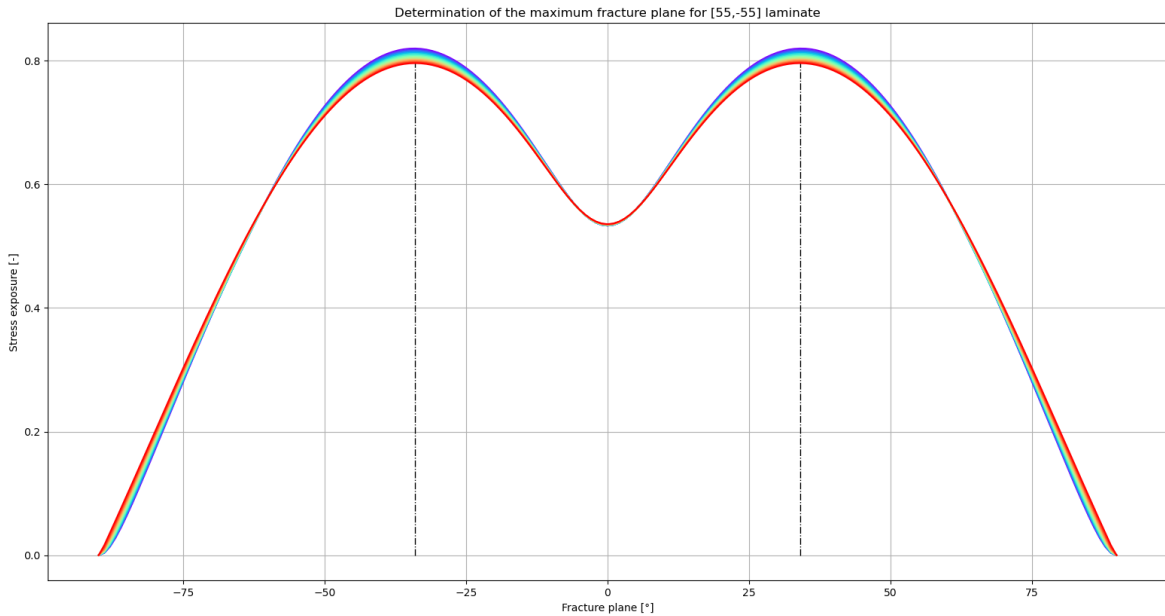


Figure 2.7: Variation of stress exposure for a $[55, -55]_4$ laminate for an internal pressure of 35 MPa, generated with Python

2.5. Filament winding

This manufacturing method deposits tape on the mandrel which originates from a spool or bobbin [7]. Filament winding (FW) is a sub-division of Automated Fibre Placement (AFP), as both manufacturing methods use a similar type of delivery head for placement of tow-preg, but deposit the tape differently, also shown in Figure 2.8. Prior to placement on the mandrel the tape can be pre-heated to increase the tack of the material system. As opposed to AFP, FW does not have a compaction roller directly on the mould, but rather uses a guidance roller. The guidance roller puts the tape under tension prior to placement on the mould. Using the compaction roller in the AFP process could reduce the number of voids present in the laminate, while the compression during the FW originates from the tension on

the tape during the winding. However, the robot head is closer to the mandrel and fixture if it directly places the tape on the mould. This could cause collision with the robot head and the fixture or mould for low winding angles. Following this, both methods could have up to 7 degrees of freedom, namely 3 translation, 3 rotational and the rotation of the mandrel. Using FW a continuous path is placed on the mandrel, except if there is a change from helical to hoop path, or the other way around. Then the tape could be cut and re-attached to the mould. However, it is possible to make a transition path from helical to hoop and the other way around [23]. This is achieved by using a non-geodesic winding path to transition from hoop to helical path or the other way around. A geodesic winding path is one which connects two points on a surface along the shortest distance [30]. These type of paths have a good stability, i.e. do not slip or move and thus do not require any friction, as discussed in Section 2.5.1. Contrastingly, any path which deviate from the geodesic path does require friction and is defined as non-geodesic winding paths. To generate a continuous path, the tape should turn-around on the polar boss. This may induce bridging of the tape and could be mitigated by increasing the dwell or minimum turning radius. During the steering, the inner tows are in compression which may result in out-of-plane buckling of the tape and should be avoided [7, 40].



Figure 2.8: AFP robot head used for filament winding of a CPV at the samXL facility

2.5.1. Friction coefficient

During placement of tapes they tend to move along a path called the geodesic trajectory, which is the shortest path between two points on a curved surface. This type of path has a good stability, provides a short path length and does not require any friction. Any path which deviates from the geodesic pattern requires friction and is defined as a non-geodesic winding path. These trajectories enable a greater design freedom in terms of achievable winding angles. Here, it is favourable to have a higher friction coefficient, as this yields a greater design space. This could be used to optimise the strength of each lamina. Furthermore, friction is defined as the ratio of lateral over normal force, as illustrated in Equation 2.24 and illustrated in Figure 2.9. The primary forces acting upon a non-geodesically wound

trajectory are the tensile force, normal force and the force transverse to the tape [30]. The latter force may cause the tape to slip during the winding if the material has insufficient friction. The onset of slippage occurs once the maximum available friction, which is 0.5 in this thesis, exceeds the ratio of lateral force over the normal force [24], as defined in Equation 2.24.

$$\lambda = \frac{F/R_n}{F/R_g} = \frac{f_\mu}{f_n} \quad (2.24)$$

where F is the longitudinal fibre force, R_n the normal radius of curvature, R_g the geodesic radius of curvature, f_μ is the lateral force per unit length and f_n the normal force per unit length [23].

The friction coefficient depends on several factors. The main factor is the viscosity of the resin. Increasing the viscosity results in a higher available friction coefficient [53]. Other influences such as winding speed, tension on the tape do not have a significant effect on the magnitude of the coefficient. Another major influence is the underlying surface. Here a polymeric liner will result in a different friction coefficient, compared to winding of tow-preg tape. Generally, a higher friction coefficient is achieved for a coarser underlying surface. The exact quantification of the available friction for a material system may be difficult to determine. However, Koussios [23] created a mandrel shape, in which the axial position represents a friction value. The quantification of the friction coefficient for the present tow-preg tape is evaluated in Section 5.2.

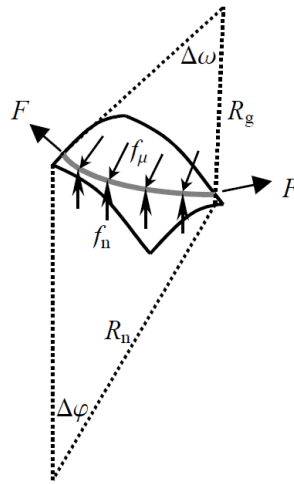


Figure 2.9: Lateral and normal forces acting on a winding path [23]

2.5.2. Winding path

Geodesic winding path is determined by the meridian profile and the polar radius, which results in a unique winding path. Therefore, another option is to use non-geodesic winding, which requires frictional forces, as explained in Section 2.5.1. Through this, a wider range of winding angles can be achieved on the cylindrical section, starting from 90 degrees at the polar boss. This is useful because several studies [36, 38, 18, 27] have shown that a beneficial stress redistribution can be achieved by adjusting the winding angle through the thickness. Here, non-geodesic winding on a random shape profile is defined as [58]:

$$\frac{d\alpha}{dz} = \lambda \left[\frac{\sin\alpha \tan\alpha}{r} - \frac{r''}{1+r'^2} \cos\alpha \right] - \frac{r' \tan\alpha}{r} \quad (2.25)$$

where r, r', r'' are the functions of the shape profile and the first and second derivative of the shape profile, respectively. This equation has an analytical solution for certain profiles, otherwise these should be solved using iterative procedures. A common solution method is the fourth-order Runge-Kutta numerical scheme.

For the continuity of the winding path, the winding angle approaches 90 degrees at the polar radius. However, care should be taken in the numerical scheme, as divergence might be observed when

approaching this angle using Equation 2.25. This is because for angles above 89 degrees, the first derivative of the shape profile, becomes very small, which results in a singularity.

As can be seen in Equation 2.25, using $\lambda = 0$, results in the traditional geodesic winding path. However, using an increased value would result in the ability to achieve a wider variety of winding angles. For wet-winding of CPVs a $\lambda = 0.2$ is usually used and a $\lambda = 0.5$ for dry winding or tape winding [58, 50].

Furthermore, it is possible to use either positive or negative friction. Using positive friction, starting from the polar boss, results in a higher winding angle on the cylinder as opposed to geodesic winding. On the contrary, negative friction may be used to achieve a lower winding angle on the cylinder than geodesic winding. This effect is illustrated in Figure 2.10.

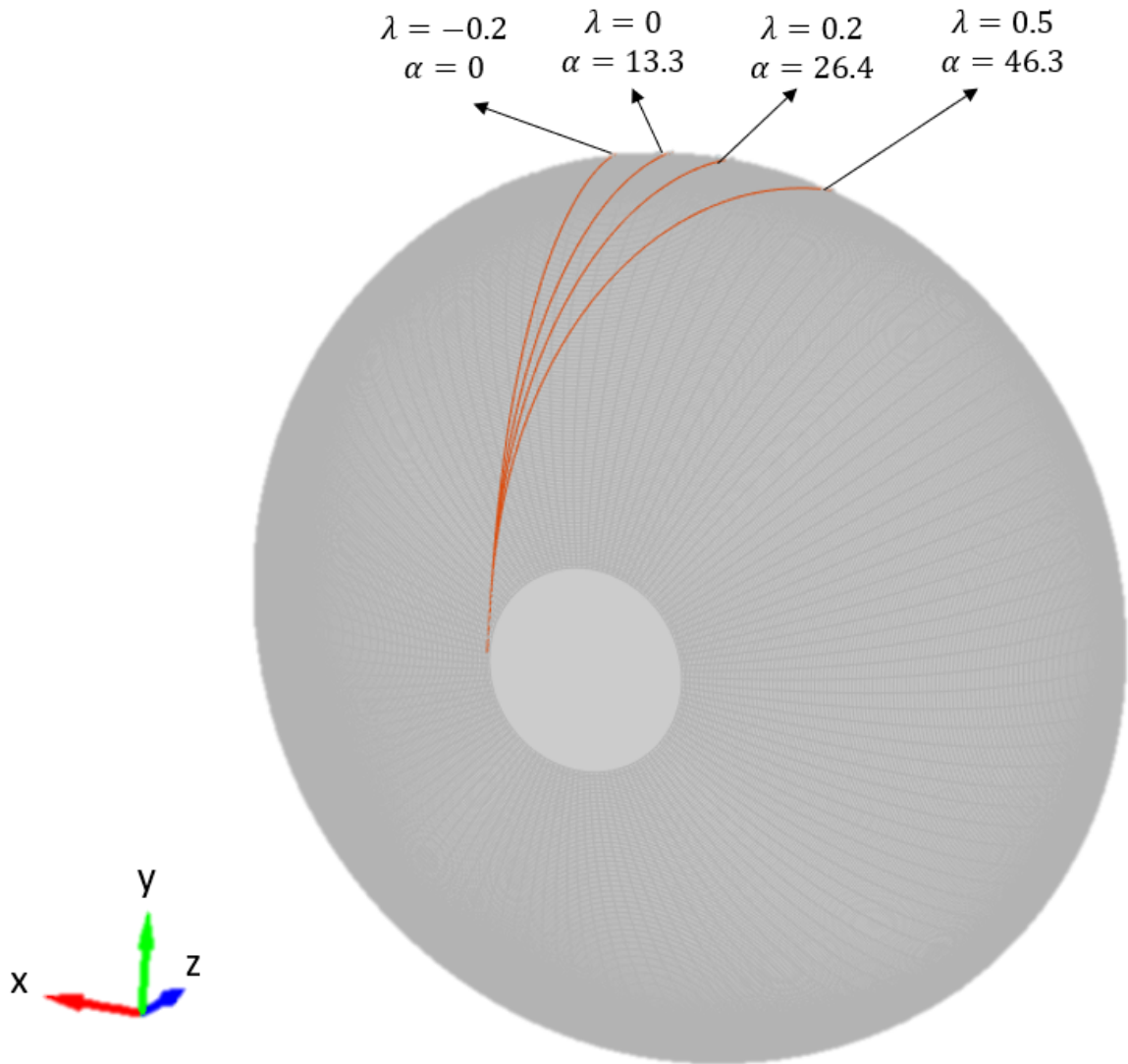


Figure 2.10: The effect of friction on the winding path, plotted on the outer liner profile as defined in Section 2.1

2.5.3. Coverage

To fully cover the rotationally symmetric mandrel it is important that there exists a repetition in which the periphery is fully covered [23]. This requires that the tape width be an integral multiple of the tangential dimension of the CPV. However, if the tape is positioned at an angle with respect to the meridian an effective width should be utilised [34]:

$$\cos\alpha = \frac{W}{W_{eff}} \quad (2.26)$$

where α is the winding angle with respect to the meridian. To be able to get a complete coverage of the CPV, the tape should be placed adjacent next to each other along the complete circumference. However, during the production of a CPV a positive winding angle is interchanged by a negative angle. This results in an intertwined structure on the cylinder and dome. Thus, to obtain a full coverage on the CPV, a positive and negative layer should be placed. This is defined as 200% or fitting the effective tape width twice along the circumference of the cylindrical section. which can be expressed as [23]:

$$n \frac{W}{\cos \alpha} = 2 * 2\pi R_{cyl} \quad (2.27)$$

The above equations are also visualised in Figure 2.11. Usually it is difficult to exactly obtain a desired coverage value. Because using the effective width it is complicated to fit the tape width an integer times in the circumference. Therefore it is accepted to have a slight deviation with the required coverage parameter in order to find a suitable winding pattern.

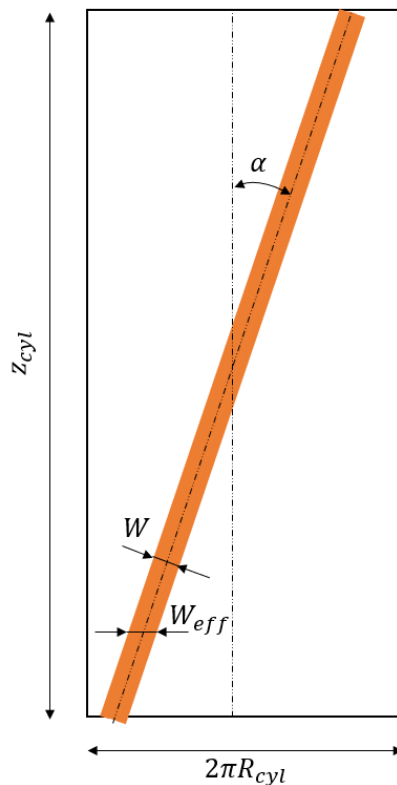


Figure 2.11: Unwrapped cylindrical section illustrating the effective width of a towpreg tape at a winding angle α

2.5.4. Winding pattern

The production of a rotationally symmetric CPV using FW leads to the creation of a winding pattern. This pattern is created by the repetitive nature of FW and the requirement to fully and equally cover the equator of the CPV [23]. The objective to create an uniform thickness on the periphery of the product results in a game of integers. For this thesis the tape width and the amount of coverage is a set parameter. To create 200% coverage the following variables can be altered to create a suitable pattern [19, 11]:

- p: number of angular partitions in which the equator is divided
- q: number of partitions skipped for one winding path
- n_q : number of points on the equator which are skipped in one step of the winding pattern
- s: leading or lagging pattern

An example of a schematic winding pattern is shown in Figure 2.12. A winding pattern can be described by defining p and q. In this example with $p = 5$ and $q = 2$, the equator is divided into 5 angular partitions.

After the first winding path the loop progresses 2 partitions in clockwise direction. When this process has been performed 5 times the pattern is repeated. For a leading pattern the loop starts on the right side of the initial position and for a lagging pattern the new loop starts on the left side of the first point. The decision if a winding path is lagging or leading depends on the amount of overlap created with that particular pattern and the type of material used, for a tacky material a lagging pattern may be preferred. The goal is to achieve a uniform thickness distribution with a minimal tape overlap and reducing the thickness build-up on the dome section.

However, the starting point and the endpoint of a loop may not coincide. An additional dwell angle may be required to match the loop at the turn-around points. The dwell angle is the angular propagation at the turn-around point [23]. A larger dwell angle will result in a higher thickness build-up on the polar boss, because more tape is deposited at this area.

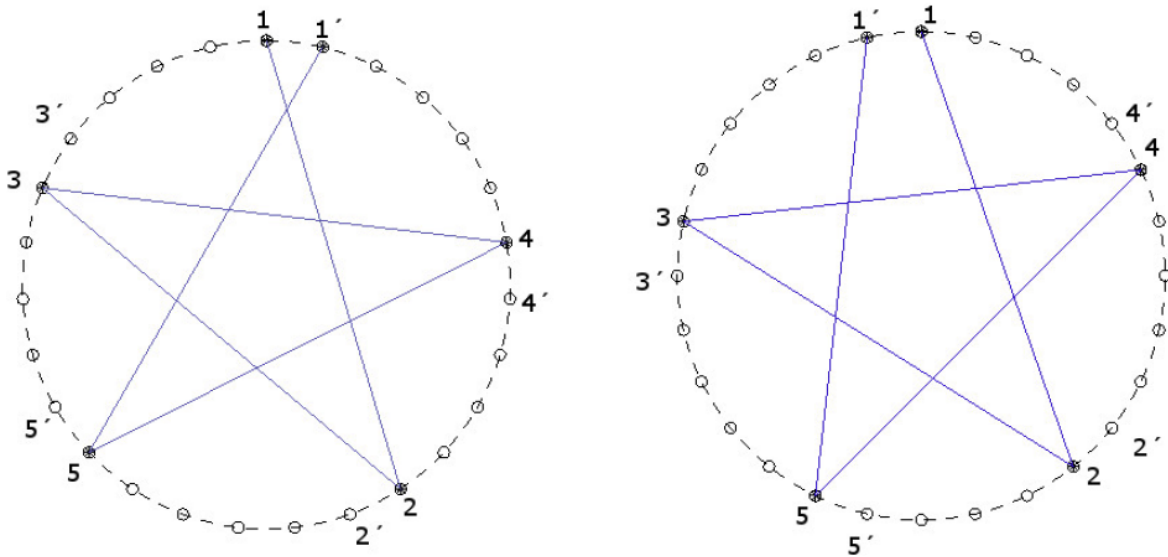


Figure 2.12: A leading (left) and lagging (right) 5/2 winding pattern [19]

After several winding paths a characteristic unit cell is formed on the mandrel, commonly defined as a diamond or mosaic shape, also shown in Figure 2.13. The size of the repetitive unit cell depends on the variable p . For a larger value of p , the length of the unit cell reduces. This is defined as a high winding pattern. It is desirable to have a low p value, as high values might induce more voids [44]. These voids may act as crack initiators.

Concluding, the creation of a winding pattern depends on several factors, such as the number of partitions on the equator, the tape width and the dwell angle. The final goal of the winding pattern is to obtain a uniform thickness along the circumference and minimising the thickness build-up on the polar boss. For a particular winding path a finite number of winding patterns are available to choose from. Here, the pattern which minimises the overlap of tape, i.e. a coverage higher than 200%, and the dwell angle should result in the minimisation of the utilised tape. Furthermore, it is also undesirable to have a lower coverage than 200%. As this would result in dry spots on the CPV, which could possibly result in premature failure.



Figure 2.13: Example of a unit cell with the characteristic diamond shape [44]

2.6. Analytical description of the dome thickness

During the production of CPVs a varying thickness is inherently created due to the varying winding angle on the dome section. Here, the winding path should be tangent at the polar boss to ensure a continuous winding for subsequent paths. This results in a thickness build-up on the polar boss section and can lead to several production and mechanical issues. To describe the mechanical behaviour of CPVs it is necessary to make an accurate estimation of the thickness build-up. Neglecting the additional thickness, would result in an underestimation of the stiffness at the dome section and the stress/strain results would be incorrect in the FEA model. One simple method to describe the variation of the thickness on the dome section is described as follows [43]:

$$t(r) = \frac{R \cos \alpha_0}{r \cos \alpha} t_r \quad (2.28)$$

where R , α_0 and t_r are the radius, winding angle and thickness at the cylinder, respectively. Also, r , α and $t(r)$ are the local radius, local winding angle and thickness at a radial position, respectively. The simplicity of the equation makes it prone to inaccuracies. Here, the thickness at the polar radius becomes infinite, because the tape width is assumed to be very thin [52, 51].

More recently, several publications have made similar attempts to describe the thickness better, such as Vasiliev et al [51], Koussios [23] and Wang et al [52, 43]. These methods divide the determination of the thickness into two parts; from cylinder to two tape-width distance ($r_{2b} < r \leq R$) and from two tape-width distance to the polar boss ($R_0 \leq r \leq r_{2b}$), where $r_{2b} = R_0 + 2b$. In this thesis Wang's method is used, because several publications [26, 52] have validated the thickness build-up on the dome using this approach, showing a high degree of correlation with experimental tests. To determine the thickness, using Wang's method, from the cylinder, up to a distance of two tape distance ($r_{2b} < r \leq R$), the following equation should be used:

$$t(r) = \frac{m_r n_r}{\pi} \left[\cos^{-1} \frac{r_0}{r} - \cos^{-1} \frac{r_0 + b}{r} \right] t_p \quad \text{for } r_{2b} < r \leq R \quad (2.29)$$

where m_r , n_r are the number of single plies and their quantity at the cylinder, respectively, and can be determined as follows:

$$n_r = \frac{t_r}{2t_p} \quad m_r = \frac{2\pi R \cos \alpha_R}{b} \quad (2.30)$$

where t_p and b are the thickness of a tape and the width of a tape, respectively. Furthermore, t_r and α_R are the thickness of the tape at the cylindrical section and the winding angle at the cylinder. Here, t_r is usually defined for a $\pm\alpha$ helical ply, as one layer commonly consists of a plus and minus ply for CPVs. But in this thesis the thickness is calculated for each single ply and therefore $n_r = \frac{1}{2}$. Following this, the section from two tape-width, until the polar boss should be calculated ($R_0 \leq r \leq r_{2b}$). Multiple theories attempted to use a similar expression as Equation 2.29 to be able to describe the thickness in the last part. However, this results in a sharp thickness peak at around a tape-width distance from the polar radius, as can be seen in Figure 2.14 for the simplified and Vasiliev's method. In reality this peak is not observed due to several phenomena, such as fibre slippage, material consolidation and fibre realignment. Thus, during the production of CPVs, this peak is spread over the region adjoining the peak, but the amount of material present at the peak remains invariant. Therefore a cubic polynomial is fitted to adjust for the sharp peak. This cubic polynomial is constructed using four boundary conditions, which in most methods can be divided in [52]:

- The thickness at the polar radius should equal the thickness at the cylindrical section, i.e. $m_0 n_0 = m_R n_R$, where m_0 and n_0 are the quantity of fibre tows and number of single plies at the polar radius.
- The thickness at two tape-width should be accordingly Equation 2.29
- Derivatives of the cubic spline equation should be continuous and smooth, i.e. $t(r) \in C^2$ for $[R_0, r_{2b}]$
- The volume is invariant within two tape-width, i.e. the peak is spread over this area

Using these statements, a system of equations can be constructed, to solve for the cubic polynomial, which is defined as:

$$t(r) = A + Br + Cr^2 + Dr^3 \quad \text{for } r_0 \leq r \leq r_{2b} \quad (2.31)$$

where the coefficients can be computed using the system of equations defined below:

$$\begin{Bmatrix} A \\ B \\ C \\ D \end{Bmatrix} = \begin{bmatrix} 1 & r_0 & r_0^2 & r_0^3 \\ 1 & r_{2b} & r_{2b}^2 & r_{2b}^3 \\ 0 & 1 & 2r_{2b} & 3r_{2b}^2 \\ \pi(r_{2b}^2 - r_0^2) & \frac{2\pi}{3}(r_{2b}^3 - r_0^3) & \frac{\pi}{2}(r_{2b}^4 - r_0^4) & \frac{2\pi}{5}(r_{2b}^5 - r_0^5) \end{bmatrix}^{-1} \begin{Bmatrix} \frac{t_R \pi R \cos \alpha_0}{m_0 b} \\ \frac{m_R n_R}{\pi} \left[\cos^{-1} \frac{r_0}{r_{2b}} - \cos^{-1} \frac{r_0 + b}{r_{2b}} \right] t_p \\ \frac{m_R n_R}{\pi} \left[\frac{r_0}{r_{2b} \sqrt{r_{2b}^2 - r_0^2}} - \frac{r_b}{r_{2b} \sqrt{r_{2b}^2 - r_0^2}} \right] t_p \\ V_{const} \end{Bmatrix} \quad (2.32)$$

where V_{const} are defined as:

$$V_{const} = \int_{r_0}^{r_b} 2\pi r \frac{m_R n_R}{\pi} \cos^{-1} \frac{r_0}{r} t_p dr + \int_{r_b}^{r_{2b}} 2\pi r \frac{m_R n_R}{\pi} \left[\cos^{-1} \frac{r_0}{r_{2b}} - \cos^{-1} \frac{r_0 + b}{r_{2b}} \right] t_p dr \quad (2.33)$$

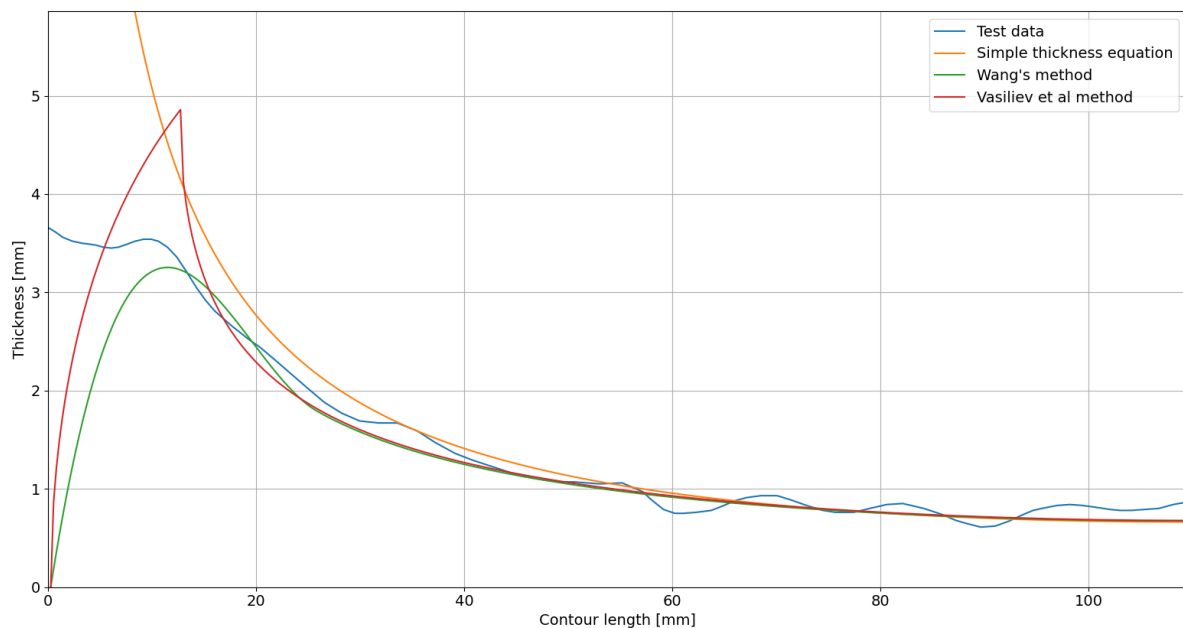
Reviewing Wang's formulation it should be recognised that in Equation 2.29, the first part in the brackets illustrates the Clairaut equation. Also, α_R in Equation 2.30, is the winding angle which is achieved using geodesic winding, at the cylinder. Therefore, to obtain the correct thickness at the cylindrical section, i.e. at R for $t(r) = t_p$, a geodesic winding pattern should be used, which is uniquely defined by the polar radius and cylinder radius. This assumption violates the goal of the thesis. Because it is evaluated what the effect is of using towpreg instead of wet-winding for the production of CPVs. Using towpreg increases the friction coefficient to 0.5 from 0.2, where the latter is applicable for wet-winding [51]. Thus, using this assumption may result in a deviation of the variation of the thickness in the numerical models versus the produced CPV. However, currently, no analytical methods exist which approximate the thickness at the dome for non-geodesic winding patterns.

In previous research by Taniq [46], test data has been collected to evaluate the performance of several thickness algorithms, described above. This data is plotted with Python in Figure 2.14, using the data provided in Table 2.4. It is important to note is that the test data is plotted along the contour length of the dome section, obtained by $ds = \sqrt{dz^2 + dr^2}$, where s is the contour length in mm. It should also be noted that the simplified method from Vasiliev et al [51] is used to illustrate the sharp thickness peak at one tape-width. This method does not consider a cubic spline in the region near the polar boss.

In Figure 2.14 initially on the polar boss the thickness is underestimated by Wang and overestimated by the other models. However, a good correlation is observed for increasing contour positions between the experimental and analytical models. This is because in this region the stacking of plies is less prominent, than around the polar boss. Since for this example the turn-around point is located at the polar boss, a turn-around point is required to create a continuous winding path. The thickness build-up can be further altered by the definition of a dwell angle, which is further discussed in Section 2.5.4. For thick-walled CPVs significant thickness build-up may accumulate at the polar boss. This can be mitigated by defining several stepbacks, to create a more uniform thickness distribution on the dome. Wang's method uses the cubic spline method to smear the volume, which results in a better approximation of the thickness build-up, for $r < r_{2b}$. However, Vasiliev overestimates the maximum thickness generated in this section, because it does not account for the slipping and realignment of the tape near this section. A sharp peak is present, because in this section a $\cos^{-1}(\frac{r_0}{r})$ term is present, which is initially zero on the polar boss and increases rapidly for increasing radial position. Furthermore, all methods converge to the similar tape thickness on the cylindrical section. Main research to improve the analytical thickness distribution should be focused on the region near the polar boss. This should include the effect of non-geodesic winding paths and ply realignment.

Table 2.4: Input parameters for the experimental test

	Units	Values
R_0	mm	20.2
b	mm	12.5
t_{ply}	mm	0.33
α_0	rad	0.362
R	mm	100

**Figure 2.14:** Comparison of the thickness distribution for several methods versus test data

2.7. Finite element model

In this thesis Abaqus [2] is used for performing the finite element analysis (FEA). Within Abaqus, geometry is discretised using elements. Each element type corresponds to a particular application. This section will review some of the most common element types. Using this background several models are created using these elements assessing their performance in Section 3.2.1.

2.7.1. Element types

The element library of Abaqus consists of a variety of element types, each with a specific use. An element commonly used for thin-walled structures is the shell element S4R, a shell with 4 nodes and reduced integration. Here, reduced integration elements only have one integration point, in the centre of the element. However, using reduced integration reduces CPU time and the stress/strain solutions are computed at the Barlow points, which are reduced integration Gauss points. These element types are also called first-order elements. Care should be taken when reduced integration is used for highly distorted structures. This may result in hourglassing, i.e. the element has no stiffness (zero-energy). This is usually resolved by introducing a small amount of artificial stiffness. Shell elements should be used when the thickness is significantly smaller than the other dimensions [2], i.e. a plane stress condition where the out-of-plane stress is negligible. However, continuum shell element can be used for three-dimensional analysis. These elements have only displacement degrees of freedom, but the kinematic and constitutive behaviour of a regular shell element. Both of these elements only require the in-plane stiffness properties in Abaqus (lamina). Conveniently, for plane-stress elements Abaqus has the possibility to compute the Tsai-Wu or Hashin failure criteria, by supplying the strength parameters. Due to this, the model does not require any extraction of the stresses to assess possible failure. Also, a

composite model can be defined using the composite modeller, in which each layer is defined with a winding angle and position.

Following this, solid elements (C3D8R) are used for thick-walled structures and when an accurate description of the stresses/strains through the thickness are required. Because the elements are described in three-dimensions, it is possible to define anisotropic material properties, which are called engineering constants in the Abaqus environment. However, in the current thesis an orthotropic material is used, with symmetry in the 2-3 plane. This is because, usually, the properties in the thickness direction are not available and are difficult to assess with experimental tests. The bending capabilities of solid elements can be improved by using a solid continuum element (CSS8). This element attempts to prevent shear locking, which is the inability to model the displacement field under bending. Here, additional degrees of freedom are introduced to improve the deformation gradient. For the (continuum) solid there is no built-in failure criteria in Abaqus. Therefore, to assess failure in a composite material, the stresses should be exported for post-processing.

Lastly, the axisymmetric elements (CAX4R) combines both the accuracy of the solid element and low computational cost of the shell element. These elements are modelled in a 2D-plane, which is applicable for structures which are axially symmetric, both in their geometry and boundary conditions. Thus, a complete CPV is described by taking a cross-section along the symmetry plane. Through this the accuracy of a solid element is used, while significantly reducing the number of required elements. Other than the shell and solid element, which are described in cartesian coordinates, the axisymmetric elements are described in cylindrical coordinates (r, z, θ) . Furthermore, the CAX4R element can be extended by allowing deformations in the hoop direction, i.e. torsion, resulting in the CGAX4R element. The problem still remains axisymmetric, because the deformation does not change as a function of the hoop-direction. These elements are used because off-axis plies may generate a non-zero resultant in the coupling terms, as reviewed in Section 3.2.1, resulting in an in-plane shear strain [59]. Additionally, for the axisymmetric element there is no possibility to compute the failure index. Therefore, it is necessary to extract the stresses.

2.7.2. Coordinate system

The global cartesian coordinate system is used in Abaqus for defining the geometry, shown in Figure 2.15. Depending on the element type, the global coordinate system is either 1D, 2D or 3D. The element which have been reviewed in this chapter are either 2D or 3D. While the geometry may be defined in a 3D plane, the element may have a 2D definition, such as the shell element.

The definition of the composite material properties is either done by lamina or by engineering constants. A graphical illustration showing the coordinate system for these material systems is shown in Figure 2.16. For a lamina, only properties 1-2 are required to be defined. For the engineering constants the properties in every direction should be defined. However, in this thesis the properties are confined to an orthotropic system, in which the 2-3 plane is isotropic.

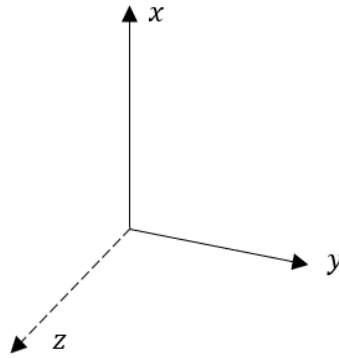


Figure 2.15: Global coordinate system in Abaqus

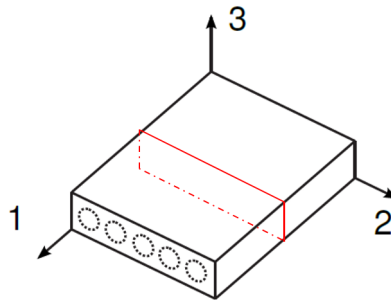


Figure 2.16: Orthotropic material coordinate system in Abaqus, with the isotropic 2-3 plane

2.8. Surrogate modelling

Numerical models have become increasingly complex and computationally expensive. This makes it troublesome to compute the non-linear design space used for optimisation. A framework to reduce the exploration of the design space is called a meta-model or surrogate model. This model is constructed from the original model, starting with a set of data points, also called as training points [8]. Based on these training points an approximate function can be constructed, which is able to predict the response of the numerical model, without the computational effort of the original model. This makes surrogate models very useful for optimisation purposes, in which large design spaces can be computed swiftly. This next section will elaborate on an efficient sampling method to determine the input for the surrogate model. Next, a surrogate model will be reviewed, which is often used and known for its robustness and reliability.

2.8.1. Design of experiments

The surrogate model needs a sufficient number of sample points, spread over the complete design space. This is defined as design of experiments (DOE). To have an accurate description of the surrogate model it is important that the sample points are not concentrated on the bounds of a design space, but rather are dispersed over the whole domain [4]. One popular quasi-random method is the Latin hypercube sampling. This method ensures that each row and column of the design space is filled.

However, for a DOE it is important to request a sufficient number of sample points, to give enough input to the surrogate model. This may be further extended by restricting the bounds of the DOE, and zooming in on a particular domain of the design space. Here, a more accurate representation of the surrogate can be achieved in the desired domain, later used for optimisation purposes.

2.8.2. Kriging

A regression model is a variant of a surrogate model, in which the predicted value should be as close to the desired value, i.e. the numerical model. Nik et al [4] made a comparison between several surrogate models and showed that the Kriging model is a robust method, with a high performance. However, the training of the model may be computationally expensive if there are a large number of design variables.

The Kriging surrogate model is named after the South-African geologist D.G. Krige [37] and comprises of two main parts [8]:

$$y(x) = \sum_{i=1}^k \beta_i f_i(x) + Z(x) \quad (2.34)$$

namely, the polynomial function $f(x)$ and the stochastic Gaussian process, $Z(x)$, with a zero mean. Also, β_i are the linear regression coefficients to be determined. The spatial co-variance function is defined as [8, 37]

$$\text{cov}[Z(x^i), Z(x^j)] = \sigma^2 R(x^i)(x^j) \quad (2.35)$$

where R and σ are the spatial correlation function and the process variance, respectively. The choice of R quantifies how good the data is fitted for the meta-model and how fast $|x^i - x^j|$ increases as R goes to zero. This means that, the prediction becomes poor. The Gaussian correlation function is often used for R :

$$R(x^i, x^j) = \prod_{l=1}^{n_x} \exp(-\theta_l (x_l^i - x_l^j)^2) \quad (2.36)$$

To assess the quality of the surrogate model a new set of training points or validation points should be generated. From this, for example the root mean square error (RMS) can be computed to observe the correlation of the surrogate model with the numerical model.

$$RMS = \frac{1}{n_{samples}} \sum_{i=0}^{n_{samples}-1} (y_i - \hat{y}_i)^2 \quad (2.37)$$

where \hat{y}_i is the predicted output value and y_i the true value from the numerical model.

2.9. Evolutionary optimisation algorithms

Evolutionary algorithms are based on the principle works of Charles Darwin representing the reproduction of animals. These algorithm types use stochastic processes, also present in nature, to evaluate discontinuous and non-convex design spaces [41]. This makes these optimisation algorithms computationally expensive. For the design of CPVs several of these type of algorithms have been employed to minimise the weight. Francescato et al [14] used a genetic algorithm (GA) to find the optimal symmetric stacking sequence for a thin-walled type III CPV. Furthermore, Leh et al [27] optimised a type IV CPV using a GA, considering the effect of damage evaluation. Alcantar et al [3] compared the efficiency of a GA with simulated annealing (SA), showing that a GA reduced the weight by 5.7% and the SA reduced the weight by 7.1%. However, SA used a different population size and can not compared with the results of the GA.

The GA is an easily implementable optimisation algorithm, which attempts to find a global minimum using several operators. This search could be unsuccessful, resulting in a local minimum, if the initial population and genetic parameters are not correctly defined. As already observed above, it is commonly used for the structural optimisation of CPVs. Following this, the algorithm is stochastic and based on an initial population [10]. The design space is examined by a population of individuals. For every individual the fitness is assessed based on the objective function. If the individual has a better fitness, the genes are passed to the next generation of individuals. Because the GA alters the chromosomes of an individual and it stochastic nature, a GA is a powerful heuristic which can cover the full design space [10]. However, due to it stochastic nature it may require many function evaluation in order to find the global minimum. This makes it difficult to implement for structural optimisation purposes, where the response function is non-linear and computationally expensive.

Based on the fitness of an individual it is selected for reproduction. The child of this individual is created by using one of the genetic operators. Each individual has chromosomes which contains the design variables. The design variables are represented by a gene, which can be encoded in binary or real numbers. For the latter it is not required to encode and decode the genes during the reproduction phase.

The continuation of the population, after the initial population, is created by several genetic operators. The first operator is the crossover of a pair of chromosomes. Here, for example chromosome A is crossed with chromosome B at a random location, creating a child with a new set of genes. Next, changing the genetic order within a chromosome is called mutation. This results in a different order of the genes within the chromosome. Lastly, elitism is used when an individual has a high fitness. This individual is conserved in the next generation without altering its chromosomes. All these operators are used to search the entire design space. The ultimate goal is to minimise the objective function. Here, the algorithm is arrested once the fitness of an individual does not improve.

3

Baseline design

Traditionally, in the preliminary design phase the required thickness of a CPV is calculated using the netting analysis [42, 57]. The result of this analysis defines how thick the hoop and helical layers need to be to reach a desired burst pressure. Here, the burst pressure is usually defined as the nominal working pressure (NWP) times a safety factor, which is 2.25 for storing of hydrogen [25, 6, 42]. However, this analysis neglects the stiffness of the matrix, assumes that membrane forces are carried by the fibres and does not consider out-of-plane stresses. This results in an underestimation of the stresses, which results in a non-conservative thickness. Therefore the results should be verified in a FEA model. Using this FEA model the number of plies are increased until failure is mitigated, i.e. the FI is below 1 in every ply.

In this chapter a design for a CPV is constructed using an analytical model. The calculation procedure and assumptions for this model are explained in Section 2.3. The analytical model considers the stresses through the thickness and the boundary conditions imposed by the domes. Using the analytical model, a quick and clear result is generated for the stresses and strains through the thickness, for any stacking sequence desired. The burst pressure can be predicted using a failure criteria and the calculated stress state from the analytical model. This procedure is performed for every single ply to evaluate the most critical lamina.

Subsequently, the stacking sequence is verified in a FEA model. In this chapter various elements are reviewed for their performance. A model is created based on the best performing element type. The creation of the FEA model consist of generating the cylindrical and elliptical geometry. In the cylindrical section the properties and winding angles do not change along the longitudinal direction. However, in the dome section several phenomena are modelled, such as varying thickness, non-geodesic winding angle and drop-off of hoop and helical plies. The resulting FEA model should enable to give a better view of the complete stress state of the CPV and if the calculated thickness, from the analytical model, are sufficiently accurate.

Lastly, a discussion will be provided, reviewing the results of the analytical model and the FEA model and what their similarities or discrepancies are. An overview of the baseline design methodology is provided in Figure 3.1. Here an additional decisional option is integrated to mitigate that the initial preliminary design constructed by the analytical model is too heavy by reviewing that the FI is above 0.8.

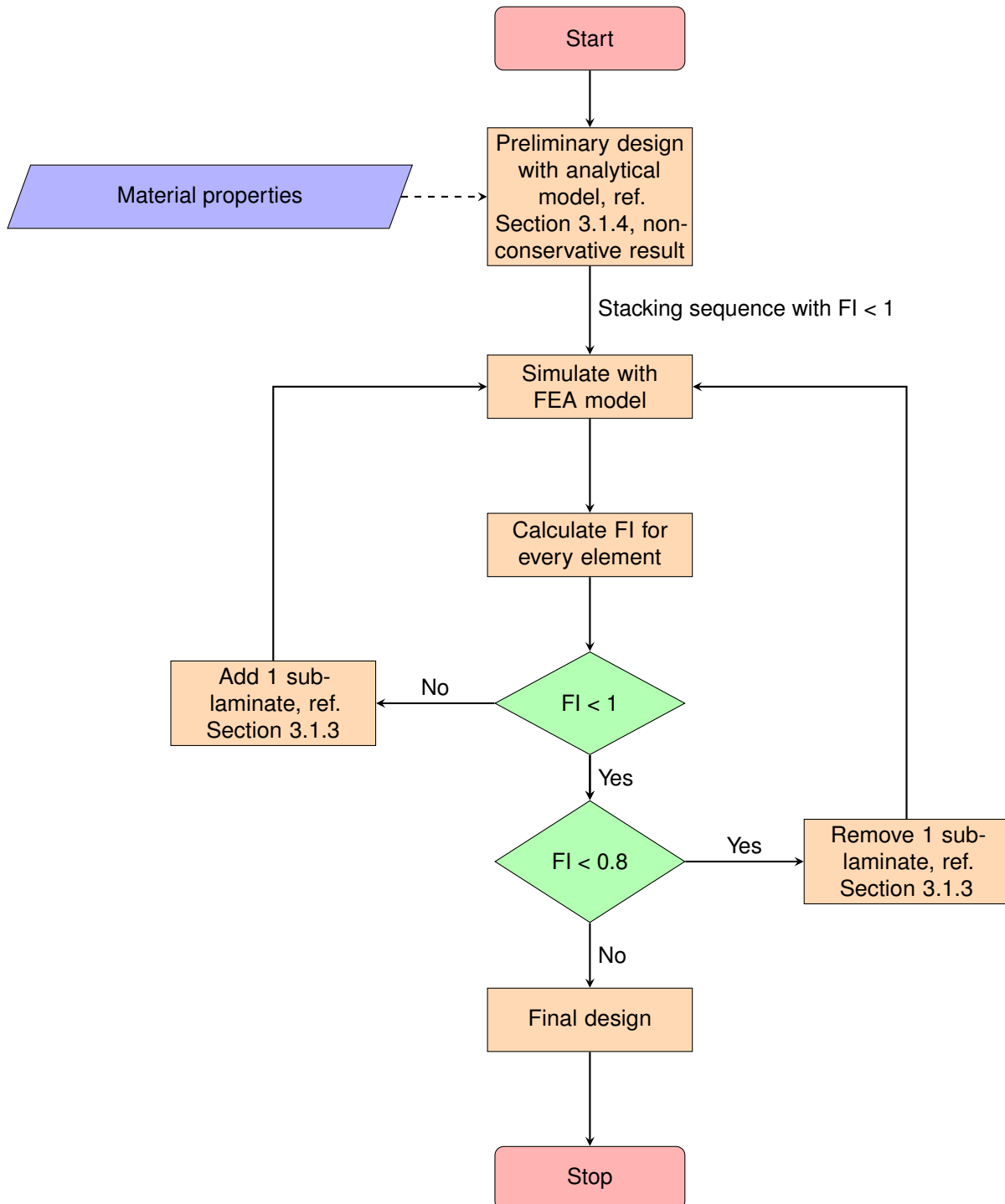


Figure 3.1: Flowchart of the baseline design methodology

3.1. Analytical model

The analytical method, described in Section 2.3, can be used to swiftly obtain the stress distribution through the thickness for any laminate, with user-defined mechanical properties, including a polymeric liner. Because of the simplicity, it can be utilised to observe the effect of stacking low and high angles, either on the inside and/or outside of the laminate. This is important, because the stacking of different angles at particular position inherently leads to a redistribution of stresses. Also, Asije et al [36] showed that the stacking sequence has an influence on the fibre volume and porosity. Namely, high angles at the outside of the laminate, compress the inner plies, resulting in a lower porosity and higher fibre volume fraction (FVF). However, this in-situ effect is not taken into account with the analytical model. Also, it solely models the cylindrical section of a CPV. The stress state at the cylinder-dome interface is not computed, which is expected to yield higher stresses than on the cylindrical section, due to the non-geodesic winding angle, doubly curved shape profile and varying stiffness. It is expected that the analytical model underestimates the maximal stresses present in a CPV. This will result in a non-conservative design of the CPV using the analytical model.

To utilise the analytical model, the orthotropic material properties and the isotropic polymeric liner material properties need to be defined. Furthermore, the inner radius of the liner and composite needs to be provided. Using this data, a stacking sequence is defined using a list or numpy array in the Python code, an example is provided below:

$$[\alpha, -\alpha] + [90, 90, 90, 90] + [\alpha, -\alpha] + [90, 90, 90, 90] \quad (3.1)$$

where α is the helical winding angle, as defined on the cylinder. This particular sequence is based on the 2:1 stress ratio from the hoop to axial stress, respectively. The left side of Equation 3.1 is located on top of the liner, thus at $R = 157 \text{ mm}$. While the right-side is the outermost part of the CPV. Thus the stacking sequence, from left to right, is defined from the outside of the liner to the outside of the laminate. A similar notation is used for the stacking sequence in the FEA model. Each ply depicted in Equation 3.1 needs to be defined individually.

Using the provided data, the procedure explained in Section 2.3 is performed. This results in the stress, strain and FI results for every ply, at any radial coordinate. It is important to note that the position where the results are computed are free of any disturbances caused, by for example meridional bending, induced by the dome-cylinder strain compatibility. This effect is further reviewed in Section 3.3.

3.1.1. Stacking sequences

This section will evaluate the effect of different stacking sequences, using the analytical model. Thus the result may only be applicable in the cylindrical region of the CPV. This is reviewed in Section 3.3.

A stacking sequence can be defined by a repeating sub-laminate. For a CPV such a sub-laminate usually consists of a set of helical and hoop plies. Using the Classical Laminate Theory (CLT) [21], constructed in Python, the ABD matrix for a sub-laminate can be reviewed. The results are presented in Table 3.1, using the material properties from Section 2.2. The goal of the design of a laminate is to inhibit the presence of the B matrix. This matrix implies that there are (undesirable) coupling terms created, if being non-zero.

Table 3.1: Evaluation of ABD components for the stacking of helical plies

	A_{11}	A_{22}	B_{13}	B_{23}	D_{11}	D_{22}
	$10^4 [Nmm^{-1}]$		$10^3 [N]$		$10^3 [Nmm]$	
$[10, -10]_2$	13.8	1.01	-9.87	-2.78	20.1	1.47
$[10, -10]_S$	13.8	1.01	0	0	20.1	1.47

As expected, the symmetric laminate has a zero B matrix. With this, the shear and extensional coupling terms are mitigated. However, during FW the helical plies have an intertwined nature. This means that at some locations the stacking is + followed by a - helical layer, while at another longitudinal positions this is switched. Therefore, the helical sub-laminate will be defined using $[\alpha, -\alpha]$.

In this section the various stacking sequences are presented which are used to evaluate the effect of stacking and grouping of plies, on the response of the CPV. Asijee et al [36] reviewed the effect of

grouping and positioning helical and hoop plies. Here, four different laminates are reviewed to observe the effect on the stress redistribution through the thickness. These are schematically shown in Figure 3.2 and can be summarised as follows:

- **Laminate A:** Alternating helical and hoop plies
- **Laminate B:** Grouping more helical and hoop plies using the same positioning as laminate A
- **Laminate C:** All hoop plies positioned on the inside of the laminate and the helicals on the outside of the laminate
- **Laminate D:** The exact opposite stacking sequence as opposed to laminate C

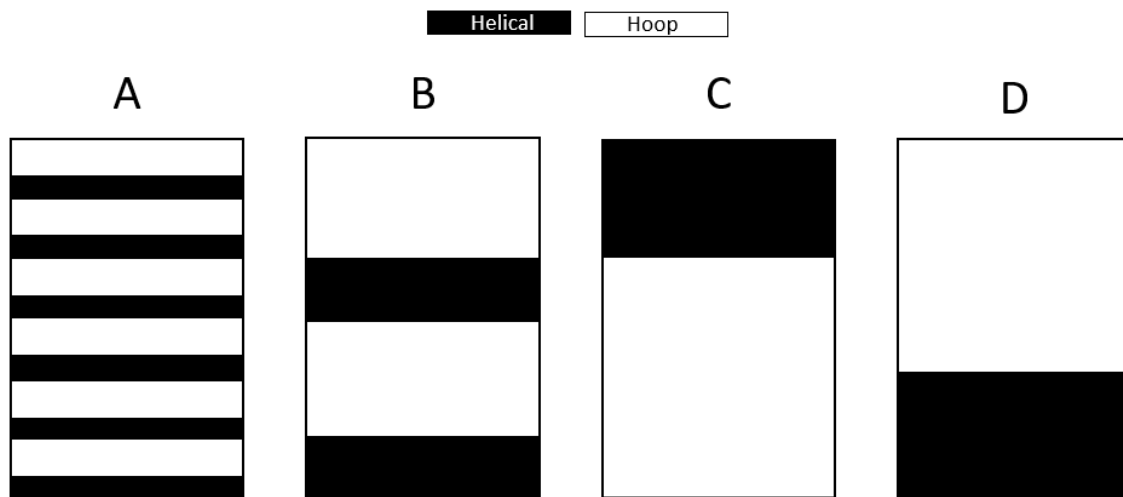


Figure 3.2: Different stacking sequences used to evaluate the effect of grouping and positioning helical and hoop plies

The bottom side of the laminates are located on top of the polymeric liner and the top side of the laminates are the outside of the CPV.

3.1.2. Selection of a failure index

Resulting from the WWFE [48] two particular failure criteria showed the best performance for evaluating failure of thick-walled CPVs. The Tsai-Wu method describes the failure surface using a quadratic polynomial, which is fitted through empirical data [58]. This method is very easy to implement as it is defined using a single equation. It is commonly used because the predicted FI is conservative [48], which results in a safe design. However, the prediction in a full bi-axial compressive stress-state is poor. But, this stress state does not or rarely occur in CPVs. Next, the Tsai-Wu failure index makes no distinction between the different possible failure modes, such as fibre failure or matrix failure. This would lead to problems in a progressive failure analysis. For such analyses the stiffness properties are degraded of the matrix or if the fibre has failed the complete lamina is discarded.

Following this, Puck's failure criteria is based on the phenomenological damage mechanism present in a lamina. Here, failure is induced by the stress acting on the action plane. To compute the FI, the maximum stress acting on the action plane is searched within $-90 < \theta < 90$, where θ is the angle of the fracture plane. The criteria distinguishes between FF and IFF, where the latter is further sub-divided into three modes.

For CPVs the most common failure type, in the cylindrical section, is intra-laminar [58, 45]. Mechanisms which can be explained as such are fibre fracture or matrix cracking. The same observation is made by Nebe [35], where mainly tangential tension and in-plane shear caused failure. Furthermore, due to the thick-walled effect, the out-of-plane stress actually prevents failure in the inner layers. This is because the radial compressive stress, reduces the deformation in-plane which is caused by the Poisson effect [35].

Furthermore, the lack of test data makes it challenging to make a well-justified decision between the two criteria. In Table 3.2 the same analysis is performed as in Section 3.1.3, but with an internal applied pressure of $P = 70$ MPa, to further emphasize the difference between the two criteria. As expected, Tsai-Wu is more conservative and thus predicts earlier failure. Puck distinguishes between five different failure modes, namely two for FF and three for IFF. The FF is mostly defined by stress on the fibre and IFF by the transverse, radial and shear stress, which can be seen in Equation 2.18. The FF and IFF attain a maximal value on the inside of the laminate and the FF increases for an increasing positive radial stress, while the exact opposite is true for Tsai-Wu. The difference in prediction can be attributed on how the radial stress is incorporated in the criteria. The negative radial stress reduces the FI for Tsai-Wu, because the transverse stress is summed with the radial stress, which has a negative value for CPVs. This summation is used at several locations in the quadratic interactive criteria, whereby it has a large influence on the FI. The effect of the negative radial stress does not influence the IFF index of the Puck criteria significantly. Actually, the exact opposite effect is observed than Tsai-Wu. The most common failure mode for Puck is IFF. The fracture plane is maximal at a 34 degree angle. At this position the shear and normal stress have the largest magnitude combined, as shown in Figure 3.3. However, the transverse stress and radial stress are not maximal because of the trigonometry equations shown in Equation 2.18. The method of including the radial stress in the failure criteria makes Tsai-Wu generally more conservative. Here, Tsai-Wu combines the fibre or matrix failure in one single criteria, while Puck makes a distinction. The Tsai-Wu has a lower FI at the inner side of the plies, where the radial stress has a higher magnitude, while Puck has the highest FI at this position because at this position the matrix stress and radial stress are the highest. The FI for Tsai-Wu increases for decreasing radial stress. Furthermore, the IFF for Puck only depends on transverse stress, radial stress and in-plane shear stress and because all these components decrease through the thickness the FI is maximal at the inner side of the laminate. In conclusion, the out-of-plane stress is differently incorporated in both criteria. This stress has more effect on the FI for Tsai-Wu than for Puck. The beneficial effect of the radial stress decreases through the thickness of the laminate, which result in the FI being present at the outside of the laminate.

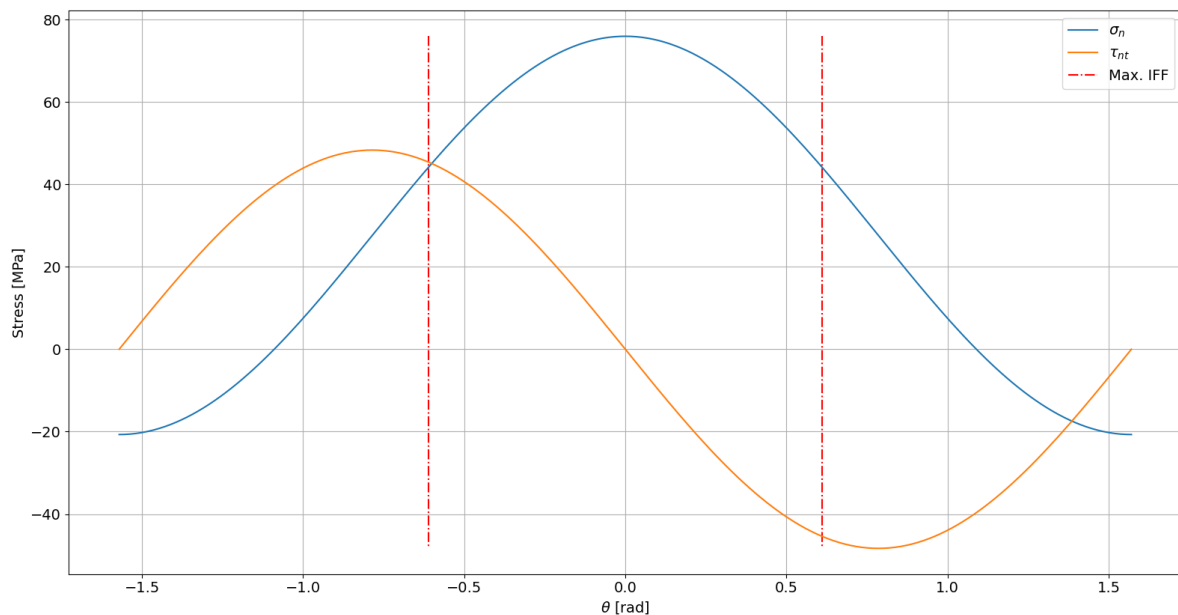


Figure 3.3: Variation of the normal and shear stress inclined on the action plane

To which extent the cylindrical stresses correlate with the analytical method is reviewed in Section 3.3. From the results stated in Table 3.2, it can be stated that the Puck criteria requires less plies than Tsai-Wu, based on the cylindrical stress state. This might be beneficial to reduce the thickness of the CPV. Though, if Puck underestimates the failure, it might result in pre-mature failure in a burst pressure test. It should be stated that in their current form both criteria only predict FPF. Thus, it might be possible that initial failure would not result in final failure. Since in practice, after the first ply has failed, the load

will be redistributed over the remaining intact plies. Here, several studies [35, 18, 29] have conducted a progressive failure analysis, still showing a significant remaining load-bearing capability after initial failure. However, the load-distribution is optimum if all plies fail at the same time, which implies that the position and angle of the ply are optimised with respect to the applied loading condition.

Table 3.2: Difference in failure prediction for a cylindrical section, reviewing Puck and Tsai-Wu, for $P = 70$ MPa and $t = 11.88$ mm, where the different stacking sequences are defined in Section 3.1.1

	A	B	C	D
Tsai-Wu	0.928	0.948	0.848	0.981
Puck	0.908	0.918	0.809	0.933

Continuing the above discussion, even less data is available in which the stacking sequence and material data is known, combined with an experimental test. Therefore, the WWFE will be used to make a decision on which failure criteria is utilised to predict failure. Here, Kaddour et al [1], showed that for a tri-axial stress state Puck had a very high degree of accuracy, while Tsai-Wu was rather conservative. A similar type of graph is shown in Figure 2.4, where Puck is conservative in the compressive-tensile area. However, generally the in-plane stress state is tensile-tensile. In this regime Puck and Tsai-Wu have a similar prediction.

Concluding, the Tsai-Wu failure criteria will be used, because there is no definitive difference between the two evaluated failure criteria. Since both can not be validated for their accuracy for the design of thick-walled CPV. Therefore, the most conservative failure criteria will lead to a safe design. This is a design in which the required burst pressure is either reached or surpassed.

3.1.3. Evaluation of stacking sequence effect

Following the helical stacking sequence, the general behaviour of the cylindrical section can be best reviewed using the strains through the thickness. Because the strain distribution through the thickness is independent of the grouping and positioning of the plies, only the magnitude will be altered. The strain distribution is illustrated in Figure 3.4. The stacking sequence used for this illustration is:

$$[10, -10, 90, 90, 90, 90]_6 \quad (3.2)$$

with an internal pressure of $P = 70$ MPa, to clearly show the thick-walled effect. Here, the helical winding angle is obtained by reviewing the minimum possible helical winding angle, using the available friction (0.5) in TW. For the helical ply, a lower angle is more desirable, as it has higher strength in the longitudinal direction. Following this, the ratio of hoop to helical layers is 2:1, following the hoop to axial stress ratio (see Section 2.3). The helical and hoop layers are added sequentially, similarly to the classical netting analysis [42, 57]. However, the grouping and positioning of the layup will be reviewed below.

In Figure 3.4 it can be seen that the meridional or axial strain is constant through the thickness of the cylinder, as also stated by Tsai [45]. The axial strain is constant, which implies that there are no meridional bending effects present in the cylindrical section. This is because the applied load is rotationally symmetric and the boundary conditions are also symmetric [35]. The hoop or tangential strain decreases through the thickness. A similar trend is observed for the radial strain, which decreases through the thickness. This effect is typical for thick-walled structures and is not observed in thin-walled analyses. The radial strain is characterised by its negative magnitude. This originates due to the radial expansion of the CPV, which results in a thinning of the wall-thickness [35]. Lastly, the shear strain also decreases through the thickness. This strain arises due to a non-zero resultant in the coupling terms, in the stiffness matrix, originating from off-axis plies [59]. In the actual FW process, positive and negative plies are inter-twined. However, in the analytical model the plies are located at a different radial position, resulting in the in-plane shear.

The above analysis shows that the axial, tangential and radial strain have the highest magnitude. Here, the axial and hoop strain are similar, because there are twice as many hoop plies as helical plies. For the cylindrical section it is optimal, to position most plies in the hoop direction, in order to alleviate

the hoop strain, because the goal of the stacking sequence is to minimise the strain, or maximize the stiffness in the load-direction.

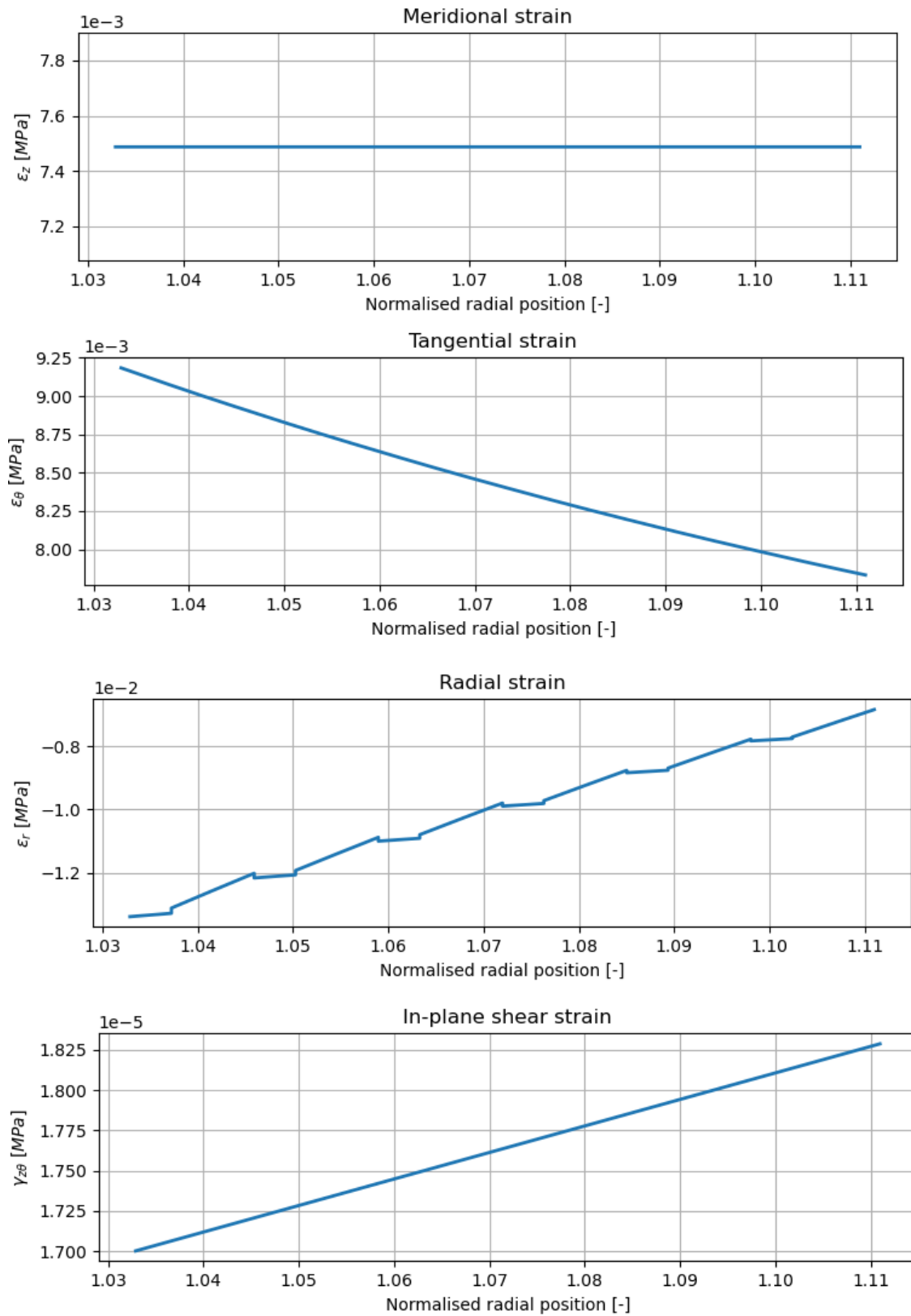


Figure 3.4: Strain distribution through the thickness of a cylinder computed using the analytical model

Following the general cylindrical CPV strain distribution, the presented stacking sequence in Section 3.1.1 is reviewed for its performance. The results are depicted in Figure 3.5. Here, the x-axis shows the normalised radial position, starting from the outside of the liner and the y-axis shows the stress in MPa or the FI. The applied inner pressure is 35 MPa, which is the desired burst pressure for this thesis. All lay-ups have the same number of a helical and hoop plies, 12 and 24, respectively. This results in a total laminate thickness of $(12 + 24) * 0.33 = 11.88$ mm. The number of helical and hoop plies are chosen accordingly to the 2:1 hoop to axial stress ratio.

Reviewing the results in Figure 3.5, the axial stress decays gradually through the thickness of the laminate and the helical plies have the highest stiffness in this direction. Furthermore, as expected the hoop plies have the highest stiffness in the tangential direction. This effect can be further amplified by positioning the hoop plies on the inner-side of the laminate. Through this the plies are located at a position where the tangential strain is the highest and the stress is alleviated more efficiently. By using a 2:1 ratio for the hoop and helical plies, the axial and tangential stress is similar in magnitude. For the cylindrical section of the CPV, the hoop strain has the largest magnitude on the inner side of the laminate. Thus placing more hoop on the inner side results in the best performance. This is seen for laminate C, where the FI is lower for the inner side, compared to other stacking sequences. This effect is further amplified by the compressive radial stress present in the inner layers. Due to this, the in-plane tensile stress is reduced because of the reduced Poisson deformation [35], caused by the radial stress. This can also be observed in Equation 2.15.

Next, the in-plane shear stress is only present in the helical plies, because plies are oriented in a $\pm\alpha$ manner and at a different radial position, which generate an in-plane shear stress. Next, the radial stress on the inner ply, starts at the applied internal pressure. However, it is slightly lower due to the presence of the liner. The outside of the laminate is required to have zero radial stress. Here, the hoop plies have a higher out-of-plane stiffness, which results in a faster decaying stress. This can be seen for laminate C, in which the radial stress has a steeper gradient.

In conclusion, the differences in FI are minimal for this applied inner pressure and laminate thickness. Laminate C has the highest stiffness on the inner side of the laminate where the tangential strain is the highest. A jump in the FI can be seen in the helical ply, which originates due to the axial stress and in-plane shear stress. This is because the helical plies are oriented at an angle with respect to the axial stress, resulting in a reduced strength, while the hoop plies are oriented exactly in the load-direction of the hoop stress. Also, the beneficial effect of the radial stress is less prominent in the outer plies. Contrarily, laminate A combines placing the hoops on the inner side and the helicals on the inner side, where the stress state is the most prominent. Another beneficial aspect is that the failure occurs in a hoop ply. This can be seen from a normalised radial position of 1.105 and higher for the oblique dotted line. This is desirable, because failure in the hoop plies is more predictable as opposed to helical plies [31]. Therefore, laminate A will be used to construct the preliminary baseline design in Section 3.1.4. A similar procedure is performed, using the FEA model to observe similarities or discrepancies between the analytical and numerical model, in Section 3.2.

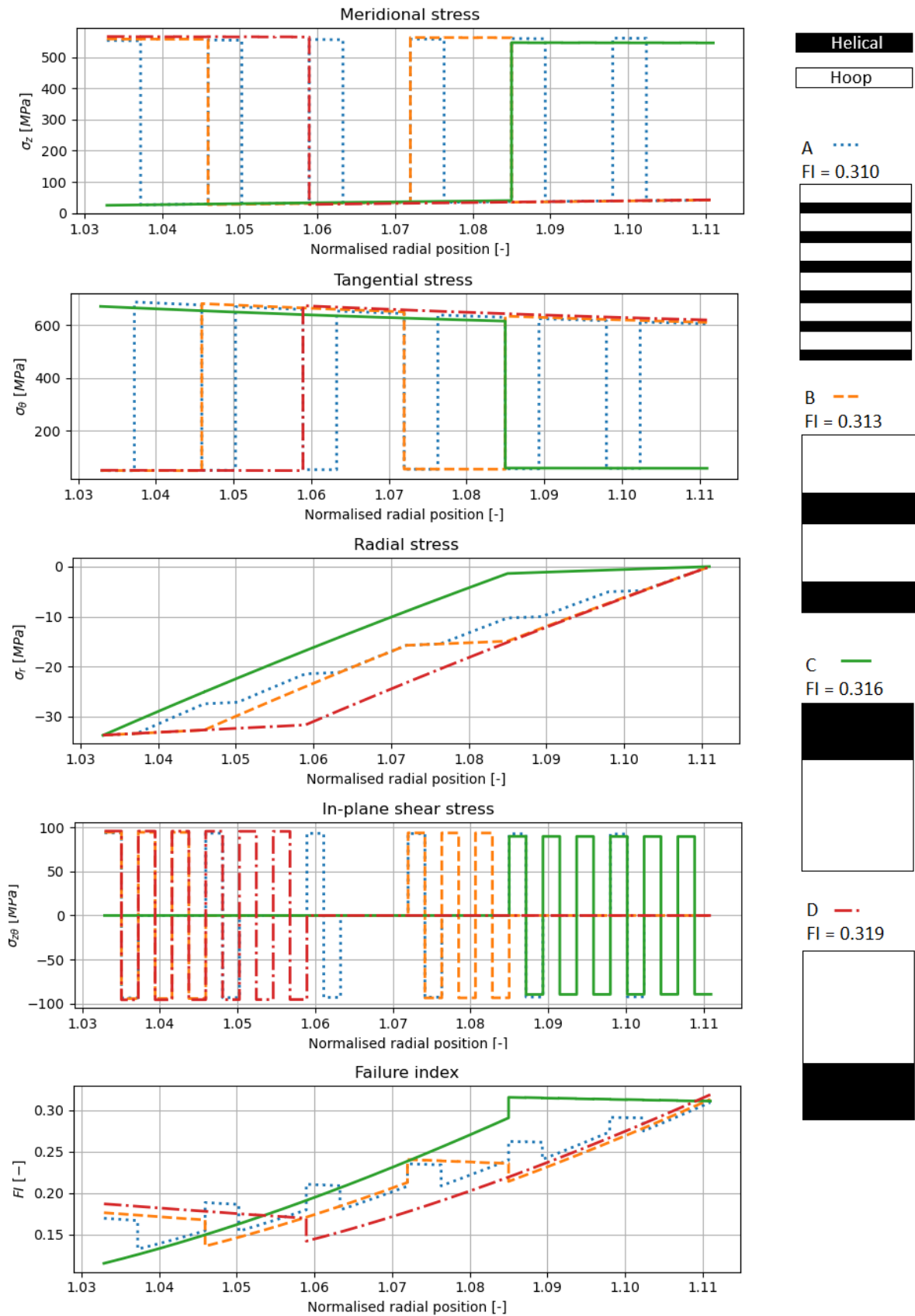


Figure 3.5: Evaluation on the stacking sequence effect for various laminates on the stress distribution through the thickness, for $P = 35$ MPa and $t = 11.88$ mm

3.1.4. Analytical baseline design

In the preliminary design phase of CPVs the netting theory is used to get an estimate of the required thickness for the laminate. For this theory it is assumed that the fibres carry all the load, while a zero stiffness is assigned to the matrix [57]. This is based on the known burst pressure failure of pressure vessels. Here it is shown that the matrix starts cracking at low pressures, while the fibre remains to carry the load until fibre fracture [59]. However, the analysis is based on the two in-plane membrane forces. This is true for thin-walled pressure vessel, i.e. a plane stress condition, but for thick pressure vessel the through-thickness stress (radial) becomes significant. The netting analysis can be divided in two parts, namely the required thickness of the hoop layers and the required thickness of the helical plies. The hoop thickness can be calculated as shown in Equation 3.3 and the helical thickness as depicted in Equation 3.4.

$$t_{hoop} = \frac{RP_{burst}}{2\sigma_{fibre}}(2 - \tan^2 \alpha) \quad (3.3)$$

$$t_{hel} = \frac{RP_{burst}}{2\sigma_{fibre}\cos^2 \alpha} \quad (3.4)$$

where R is the radius in mm, P_{burst} is the burst pressure in MPa, σ_{fibre} is the strength of the fibre in MPa and α the helical winding angle on the cylinder, which is 10 degrees. The fibre strength is taken as the strength in the fibre direction, X_t , of the tow-preg. Because during FW the complete tape is wound and not only the fibre. Also, if only the fibre strength would be used, the thickness of a single ply would be lower. Using the known data, given in Table 2.3, the required thickness according to the netting analysis is:

$$t_{tot} = t_{hel} + t_{hoop} = 1.22 + 2.34 = 3.55 \text{ mm} \quad (3.5)$$

It is assumed that the liner does not have any load-bearing capacity. Therefore the radius is 157 mm and not 152 mm. The netting analysis is very non-conservative and it indicates that the hoop ply thickness should be about twice as thick as the helical layers. Because the actual laminate strength will be lower and it only considers an in-plane stress state. In conclusion, the netting analysis requires to have $\frac{1.22}{0.33} = 4$ helical plies and $\frac{2.12}{0.33} = 8$ hoop plies, resulting in a final total thickness of $(4 + 8) * 0.33 = 3.96$ mm.

Following this, the developed analytical model, discussed in Section 2.3, will be used to construct a preliminary design. The stacking sequence will be based on the results presented in Section 3.1.3, namely alternating of helical and hoop plies. The analytical model, as explained in Section 2.3 is used to compute the number of required plies to attain a burst pressure of 35 MPa. The number of plies are increased or reduced until the FI is below and as close as possible to 1. The resulting baseline design, as a consequence of the analytical model is defined as follows:

$$[10, -10, 90_4] + [10, -10, 90_4] + [10, -10, 90_4] \quad (3.6)$$

where the left side is the bottom of the laminate. The hoop plies are most efficient on the cylindrical section, as the stress-state is predominantly in the hoop direction. Therefore, the tangential stiffness can be best increased by placing the hoops at the position where the strain is the highest. The helical plies are required to take up the meridional stress component. While a reduction in hoop plies results in a significant change in FI, the change is less significant in removing helical plies, because the axial stress component is less high. Although, the hoop plies are very inefficient in the axial direction, as the stress is in the direction of the matrix. The final thickness of the baseline design, created by the analytical model is $(4 * 3 + 2 * 3) * 0.33 = 5.94$ mm. Using this thickness results in a maximum FI of 0.83 in the 4th helical ply. The hoop stress decreases slightly through the thickness, while the radial stress decreases more rapidly, thus, the alleviation effect, caused by the radial stress is reduced, resulting in the highest FI being not in the inner ply. For this design it is not possible to remove any more sub-laminates, the stress distribution for this design is illustrated in Figure 3.6. It can be seen that the inner hoop plies have a high stiffness on the inside of the laminate and minimise the FI. However, the FI through the thickness is not evenly distributed. Meaning, the hoop plies still have remaining strength, while the helical plies are more critical. This behaviour could be further optimised by equalising the FI through the thickness, such that the load is redistributed more evenly. It can also be seen that FI is not maximised. Thus, the

laminate could be further be optimised by changing the helical winding angle or reducing the number of plies. This will be further reviewed in Section 3.3. The difference between the required thickness to reach a burst pressure of 35 MPa for the netting analysis and the analytical method is shown in Table 3.3. It can be seen that the difference in thickness is quite significant between the two methods. This is because the netting analysis assumes that all fibres carry the same load, no interaction between adjacent layers, matrix only transfers the stresses and a constant stress distribution through the wall thickness [16]. Also, it uses the strength of the fibre, which has a higher strength than a single lamina actually has, because once the resin and fibre are combined they have lower strength combined than separately. This is dictated by the rule of mixture for composites, which is defined as follows for the longitudinal modulus [34]:

$$E_1 = E_{1,f}v_f + E_{1,m}v_m \quad (3.7)$$

where $E_{1,f}$ and v_f are the longitudinal Young's modulus of the fibre and the fibre volume fraction, respectively. Also, $E_{1,m}$ and v_m are the longitudinal Young's modulus of the matrix and the matrix volume fraction, respectively. It can be seen that the actual stiffness of a lamina is lower than when only a fibre is used. Therefore the strength of a lamina is overestimated using the netting analysis. Furthermore, the netting analysis also does not consider any shearing between adjacent helical plies. This might be valid for very low angles, where the angular difference between adjacent helical plies is low. But the shear stress becomes more prominent for higher helical winding angles. Also, the netting analysis is based on in-plane membrane forces and does not consider any out-of-plane stresses. In the case for CPVs the radial stress is actually beneficial, because it hampers the Poisson deformation caused by the in-plane axial and hoop stress. Furthermore, for both methods the stresses in other area's, such as the dome-cylinder interface, are neglected. This can result in missing design-critical sections.

Table 3.3: Difference in required thickness between two methods, to create a preliminary design

Netting analysis	Analytical model	Difference
mm		%
3.96	5.94	+67

In the subsequent chapters a FEA models will be created which will also be able to get the stress distribution along the longitudinal direction. Using this model the analytical baseline model can be verified. Also, the stacking sequence effect will be verified, using the same approach as in this chapter. Using these two results, a final baseline design can be created.

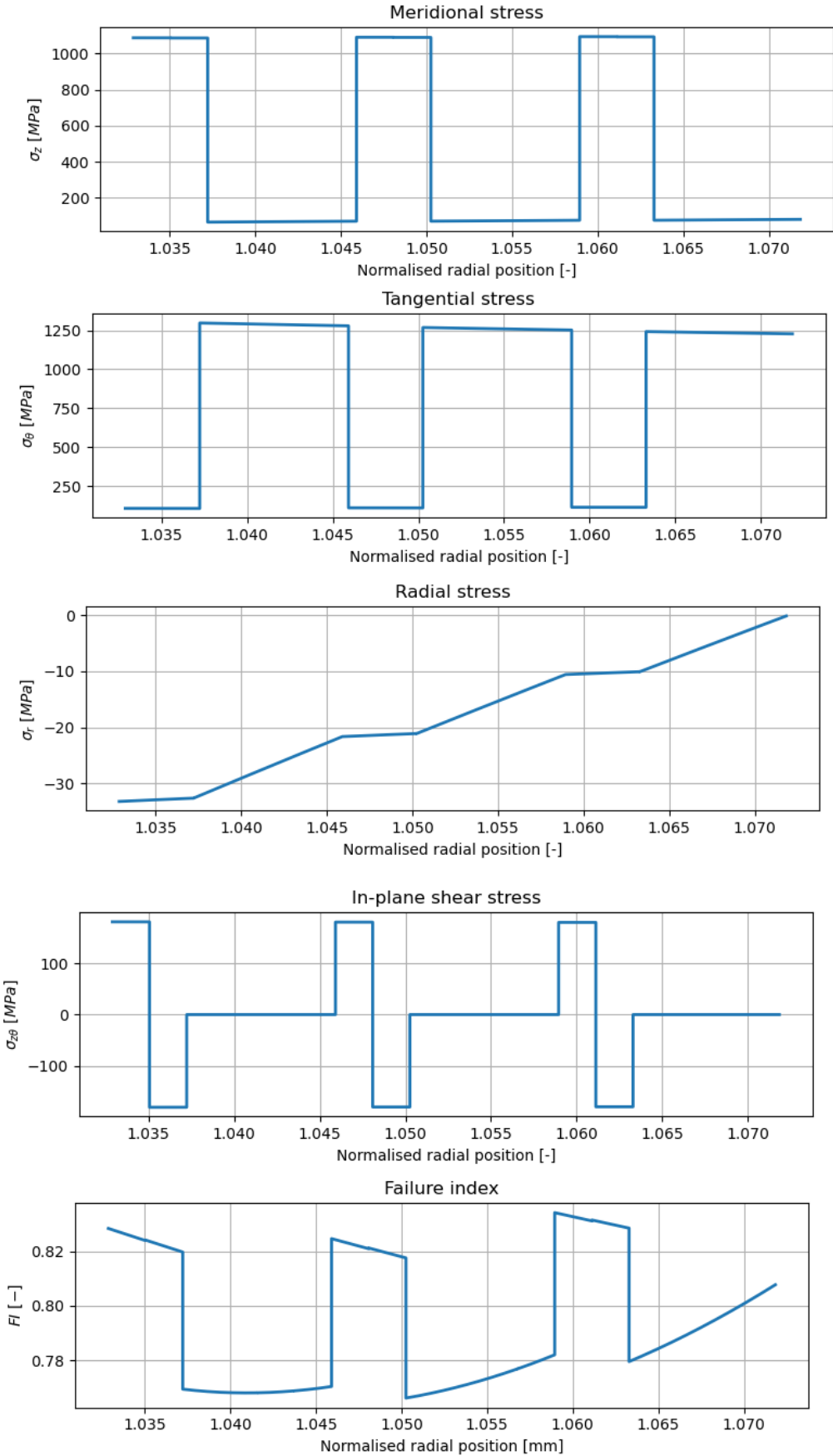


Figure 3.6: Stress distribution through thickness for the preliminary baseline design

3.2. Development of the FEA model

In Section 3.1.4 it was shown that the analytical method could be used to give insight in the three dimensional stress state at the cylindrical section of a thick-walled CPV. The method uses a boundary condition, namely Equation 2.9, to simulate the discontinuity stresses which are created at the dome-cylinder interface. As described previously, the analytical model can serve as an initial tool for the preliminary design of a CPV. However, just as the traditional netting analysis, it is required to verify the design by means of a numerical and/or experimental test. This chapter will focus on creating a numerical model, considering the additional phenomena which occur during the production of CPV, such as non-geodesic winding pattern in the dome and thickness build-up in the dome section.

3.2.1. Element performance

In this section an analysis is performed on various elements types within Abaqus [2]. This is done to assess the accuracy of these elements and the computational cost for the same problem. The stress results are compared with the analytical model. It is assumed that the analytical model yields the theoretical stress state in the cylindrical section. This is done because there are no other theoretical formulae to determine the stresses in an anisotropic thick walled CPV. These are only available for thick-walled isotropic pressure vessels. Furthermore, a $[55, -55]_n$ stacking sequence is used and an inner pressure of $P = 10$ MPa is applied, similarly as [59, 54].

The element performance for a thin-walled cylinder is shown in Table 3.4. Here, the discussed element types are compared with the analytical solution as described by Zu [59] and Xia et al [54]. Similar to the analytical model, the FEA models restrict torsion and have an additional axial load applied. These boundary conditions are applied to emulate an axial equilibrium imposed by the domes. The required axial load can be calculated using Equation 2.9, where the liner stress is zero and $n = 4$ (number of plies). It should be noted that the stresses in Table 3.4 are in the rotated system and not in the global Abaqus coordinate system. This is done because the standard global coordinate system of Abaqus deviates from the desired coordinate system. It is observed that for a thin walled structure the in-plane stresses do not deviate from the analytical stresses. However, the (continuum) shell elements are not able to capture the through-thickness stress. As observed, this influences the resulting failure index. This can also be seen in Section 2.4, where the stress in the hoop direction is summed with the stress in the radial direction. Thus, a negative radial stress could actually alleviate the failure index, this has also been observed by Nebe et al [36]. Furthermore, the computational time is lower for shell elements as opposed to solid elements. Here, the higher value for the computational time for the shell element is probably an error, which can also be seen in Table 3.5. Similarly to the analytical method, the shell elements are not able to capture the intra-laminar shear stresses. The axisymmetric elements are able to capture the in and out-of-plane stresses, while minimising the computational cost.

Table 3.4: Stress evaluation for a thin-walled cylindrical section of shell and solid elements: thin walled $\frac{R}{t} = 25$

Element type	Analytical	S4R	SC8R	C3D8R	CSS8	CGAX4R
Seed size [mm]		5	5	5	5	5
Property type		Lamina	Lamina	Eng const	Eng const	Eng const
# Elements	-	2520	2560	10240	10240	160
σ_z [MPa]	124	124	127	124	125	123
σ_θ	255	248	254	253	255	254
σ_r	-9	0	0	-9	-9	-9
$\tau_{z\theta}$	155	148	152	154	156	155
$\tau_{r\theta}$	-	-	-	0,2	8,6	0
τ_{rz}	-	-	-	0	-5	0
TsaiWu [-]	0.33	0,7	0,7	0.35	0.37	0.33
Comp time [s]	0.004	4	2	6	5	1

Conclusive, for a thin walled cylinder the shell elements describe the in-plane stresses accurately enough, while having a low computational effort. However, because the radial stresses cannot be computed for shell elements, a conservative FI is obtained. This is because the radial stresses lowers the FI. Following this, the solid elements (C3D8R, CSS8 and CGAX4R) describe the stress state

sufficiently good. However, the continuum solid element has excessive intra-laminar shear stresses which are not present in the other solid elements. Therefore, it seems that these intra-laminar shear stresses are artificially generated and should not be present. Withal, the description of stresses by the solid elements is similar, but the generation of the model and the computational effort is much higher for the (continuum) solid element.

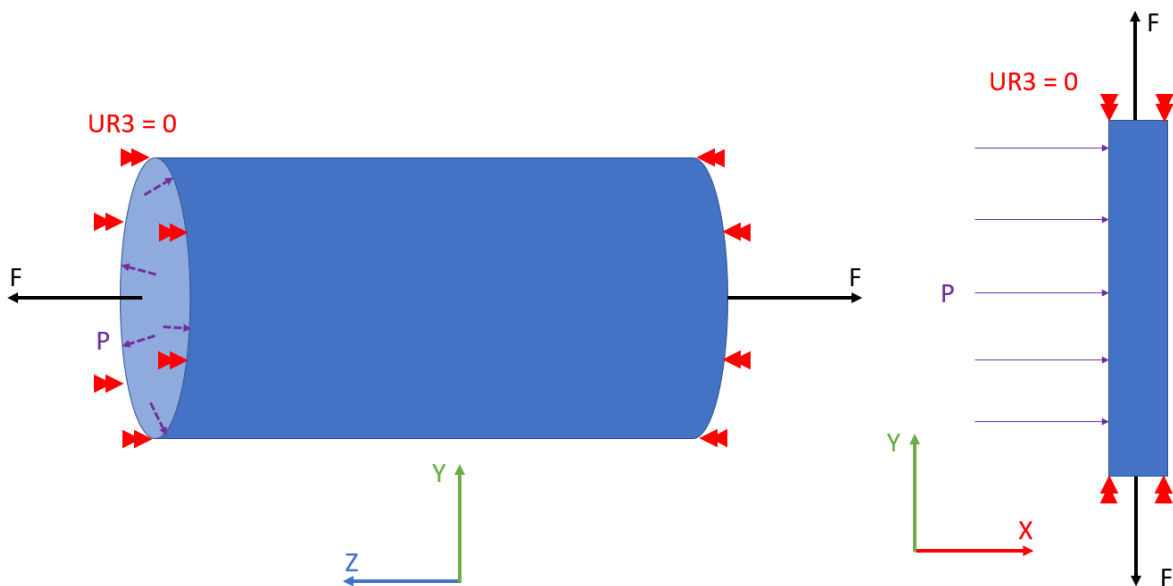
The same procedure is performed for a thick-walled cylindrical section, as shown in Table 3.5. The number of layers is increased to $n = 10$ to achieve a thick-walled condition. This is achieved by $\frac{R}{t} > 10$ [36, 59]. For the thick-walled cylinder even larger deviations are observed for the shell elements, while the solid elements show good correlation to the analytical model. In the table the number of elements required to describe the same models varies quite significantly. This is because only 1 element through the thickness is required to describe the CPV for (continuum) shell element. While the solid element has 1 element per ply, through the thickness, i.e. 10 elements through the thickness. The number of elements for a solid model can be reduced by using the laminate composite modeller in Abaqus. Through this the complete stacking sequence can be defined using a single element. However, this approach loses the through the thickness accuracy, which is characteristic for solid elements and is therefore not recommended.

In conclusion, the axisymmetric element has a good accuracy for thin and thick walled structures and a low computational time. Therefore, this element will be used to create the FEA model for this thesis. Furthermore, (continuum) shell elements can be used for thin walled structures, where the radial stress is not important. However, these element types have a better computational time as opposed to solid elements. But, solid elements are able to better capture the stress behaviour of a thick-walled structure through the thickness. Moreover, the axisymmetric element provides an accurate stress representation and has a low computational time. Also, the geometry definition is simpler, because it is not necessary to define the node locations in a three-dimensional space. The model is defined in a 2D-plane and thus, more elements can be used to discretise the model. And properties, such as the winding angle, can be defined more accurately. This without the computational cost, as opposed the solid elements. Both for the shell and solid model, the laminate on the cylindrical section can be defined using the laminate layup manager. However, on the dome section a special coordinate system needs to be defined, which would track the meridional of the dome. Moreover, for an axisymmetric model, a special coordinate system should be defined in order to describe the winding angles. When specifying the material orientation for an axisymmetric element, it is only possible to rotate around 3-axis. Therefore it is important to define a new coordinate system. Here, the axial coordinate (global y-axis in Abaqus) is the 1-axis, hoop coordinate (global z-axis in Abaqus) is the 2-axis and the radial coordinate (global x-axis in Abaqus) is the 3-axis. Furthermore, for the shell element failure of a composite can be calculated by Abaqus, using either Hashin or Tsai-Wu as failure criterion. But, for both solid elements and axisymmetric element no failure criteria exists in Abaqus. Therefore, the stresses need to be exported for each element to assess if an element has failed.

Overall the axisymmetric element shows the highest accuracy for thick-walled structures while minimising the computational effort. It is also convenient to only define the elements in a 2D space. Therefore the axisymmetric element will be used to create the FEA model. A user-defined coordinate system needs to be defined to describe the variation of the winding angle. However, this is also required for the other elements. Lastly, it is cumbersome to extract all the stresses to compute failure, but this would also be required for solid elements.

Table 3.5: Stress evaluation for a thick-walled cylindrical section of shell and solid elements: thick walled $\frac{R}{t} = 10$

Element type	Analytical	S4R	SC8R	C3D8R	CSS8	CGAX4R
Seed size [mm]		5	5	5	5	5
Property type		Lamina	Lamina	Eng const	Eng const	Eng const
# Elements	-	2520	2640	10240	10240	400
σ_z	49	49	52	49	49	49
σ_θ	106	98	105	106	106	106
σ_r	-9	-	-	-9	-9	-9
$T_{z\theta}$	66	59	62	65	66	66
$T_{r\theta}$	-	-	-	1	3	0
T_{rz}	-	-	-	1	2	0
TsaiWu [-]	-0.03	0,27	0,7	0.005	-0.008	-0.03
Comp time [s]	0,05	1	6	8	9	1

**Figure 3.7:** Boundary conditions for the shell and solid element (top) and the axisymmetric element (bottom), using the Abaqus coordinate system

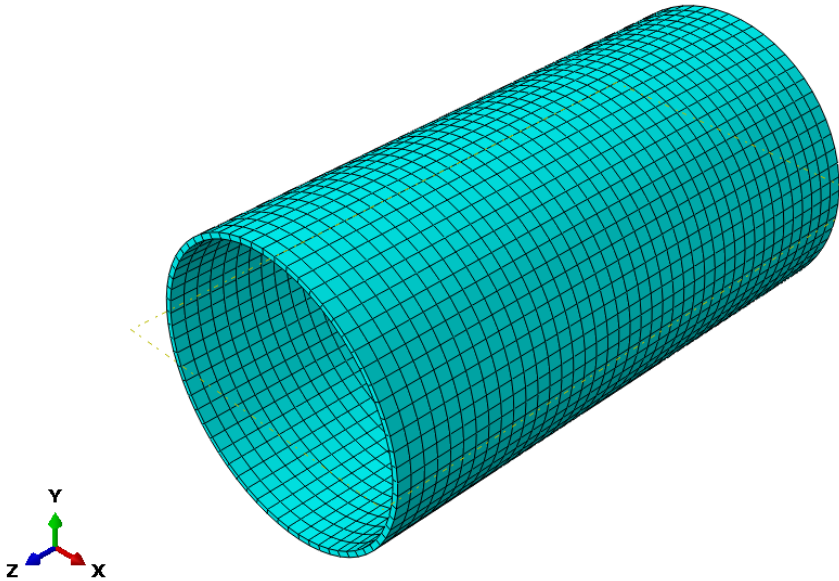


Figure 3.8: Continuum shell mesh for a cylindrical section

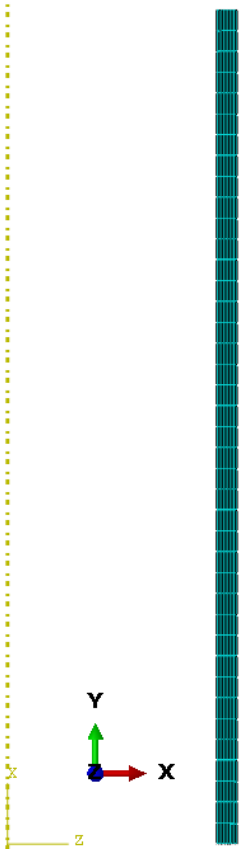


Figure 3.9: Thick-walled axisymmetric mesh for a cylindrical sections

3.2.2. Creation of the FEA geometry

Based on Section 3.2.1, the axisymmetric element shows a high accuracy and low computational effort, with respect to the other evaluated element types. For the axisymmetric element the 3D geometry needs to be discretised at $\theta = 0$ [2]. A graphical representation of the 3D dome section is shown in Figure 3.10. This picture shows a full 3D representation of the dome section. For the axisymmetric model only a plane cross-section is required. The radial and longitudinal axes coincide with the cartesian x and y coordinate from Abaqus, respectively. The full process to create the geometry and assign the properties for an axisymmetric element is described below.

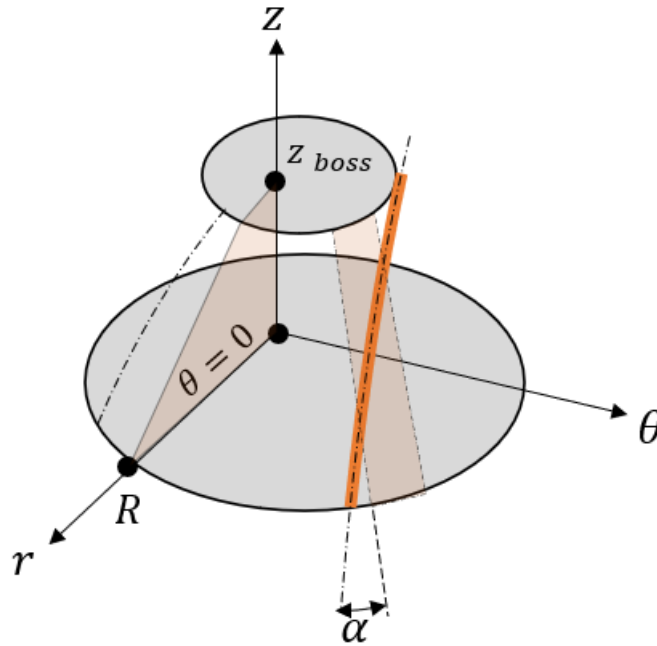


Figure 3.10: 3D graphical representation of an ellipsoid resembling the dome section, illustrating a non-geodesic winding path

Geometry

A thin slice of the ellipsoid is used to discretise the dome section, as shown in Figure 3.11. This ellipsoid is described using Equation 2.2. First, the outer liner shape is generated, in Python, using $R = 157$ mm, $h = 35$ mm and $b = 94.27$ mm, in Equation 2.2. Where the centre of the ellipse is shifted 35 mm in radial position. This is done such that the boss element coincides with the rotational axis in Abaqus, which is located in the global Abaqus coordinate system at $x = 0$. The latter is shown in Figure 3.9, as a yellow dotted line and is the z-axis in Figure 3.11. This naturally imposes symmetry boundary conditions where the boss meets the symmetry axis. At the upper extremity, z_{boss} , the composite meets with the high pressure valve of the polar boss. While at $z = 0$ the dome section ends and the radial position is maximum, i.e. the outside of the liner ($R = 157$ mm). The dome section is characterised by multiple phenomena, such as non-geodesic winding angle, varying thickness and termination of plies, which makes it difficult to model accurately. In the present thesis several characteristic are modelled, which are further discussed in Section 3.2.3 and Section 3.2.4. Below the dome section, in the negative z-direction, the cylindrical section is modelled. This can simply be done using a rectangular shape, which results in a cylindrical section if rotated around the symmetry axis.

The above process is implemented in Python. Here, the first set of nodes are generated using the outside of the liner. For the dome section the elliptical equation is used, using any desired number of points. The cylindrical section is constructed using any desired points between the $z = 0$ and $z = -290.75$ mm. From the first layer, the next one is generated by adding the ply thickness to the previous radial position. In the dome section this is achieved by adding the thickness normal to the previous shape line, as discussed in Section 3.2.3. Helical plies are modelled in a single manner, i.e. a plus and a minus helical ply are modelled separately. This is done to observe the effect on the shear

stress between dissimilar plies. Contrarily, two hoop plies are modelled as a single ply. This is done to emulate a 200% coverage of the circumferential ply and to reduce the number of elements.

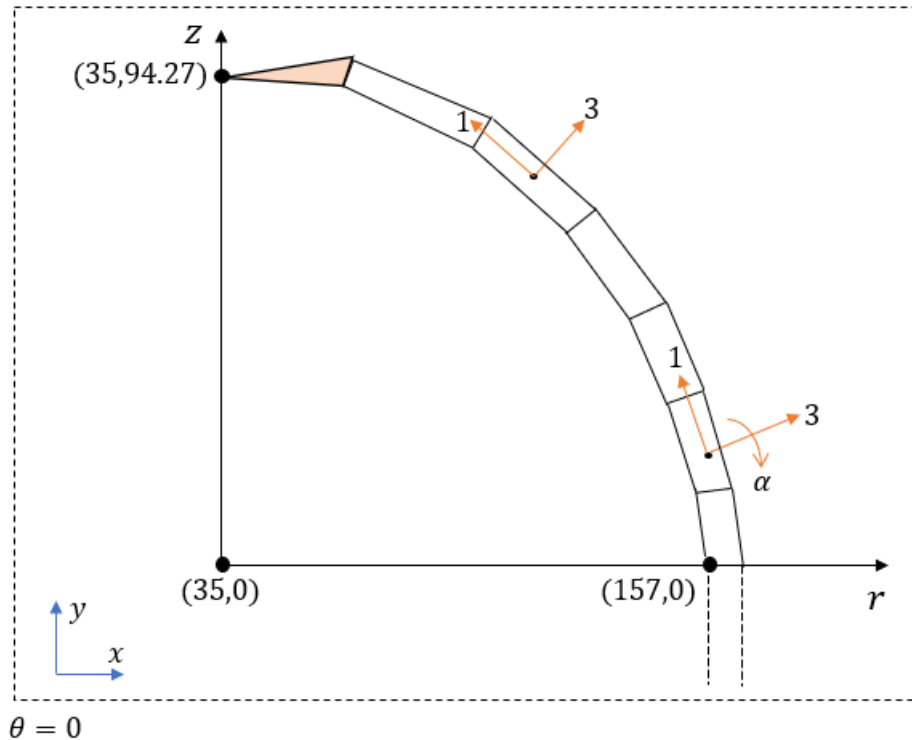


Figure 3.11: 2D depiction of the dome section as implemented in Abaqus, showing the first ply on top of the liner, also defining the used material property coordinate system

First, all the nodes are generated for the helical and hoop plies. These are created based on the defined mesh seed. This defines what size an element has on the cylindrical and dome section in millimeters. For every ply a set of nodes is created to describe the inner and outer side of the ply. On the cylindrical section the shape of the plies are rectangular and have a thickness of 1 times the ply thickness or 2 times the ply thickness, for a helical and hoop ply, respectively. Here, a single hoop ply is modelled as 200% coverage to reduce the number of elements, while every helical ply is modelled separately. The length of the rectangular element depends on the defined mesh seed. Furthermore, the shape of the elements on the dome section depend on the analytical thickness distribution, which is computed for every ply, as defined in Section 2.6. Here, the outer nodes are computed using the normal of the previous element, to correctly add the thickness. The length of the element on the dome is obtained by partitioning the dome shape in angular positions along the meridional to obtain evenly spaced elements. From the generated inner and outer nodes for all helical and hoop plies, the element connectivity is created using a counter-clockwise notation to obtain the correct element face normal.

After this, the nodes and element connectivity for the polar boss are imported from an input file. Lastly, the liner shape is created using the elliptical description in Equation 2.2 and the nodes from the first composite ply. After this the element connectivity is created for all sections. Here it is important that the first element (beige in Figure 3.11) of the composite are triangular elements, while all other elements are quadrilateral. The elements are generated counter-clockwise to obtain the correct element normal, which is important for assigning an internal pressure.

Material Properties

Every helical or hoop ply initiates with an epoxy element. This is done to simulate that during FW at the ply ends resin is squeezed out of the tow-preg. But it also results in a more smoother transition at ply drops between helical and hoop plies. The geometry of the epoxy element is further discussed in Section 3.2.3. For every element a material/section and orientation needs to be defined. The model consists of four different material types, as illustrated in Figure 3.12. Here, the polar boss is made from

stainless steel and can be defined using isotropic material properties in Abaqus. The same applies for the polymeric liner, which is used to prevent leakage of hydrogen gas and is defined using isotropic material properties. Next, every ply ends with an epoxy element and is modelled as an isotropic material. Lastly, the composite is described by orthotropic materials properties, which are defined as engineering constants in Abaqus.

The different materials are assigned to each element. On the cylindrical section the orientation remains indifferent (geodesic) along the longitudinal direction. Therefore, the property and orientation are assigned directly to all cylindrical elements of a single ply. Here, a helical layer is defined using a positive or negative angle. However, on the dome section a non-geodesic winding pattern is assigned to each element. Thus, every single element has the same material properties, but a different material orientation, as shown in Figure 3.16. Important to note is, as shown in Figure 3.11, the material orientation can only be defined using a rotation around the 3-axis in an axisymmetric model. This process is further described in Section 3.2.4. Though, the composite section and liner on the boss have constant material properties.

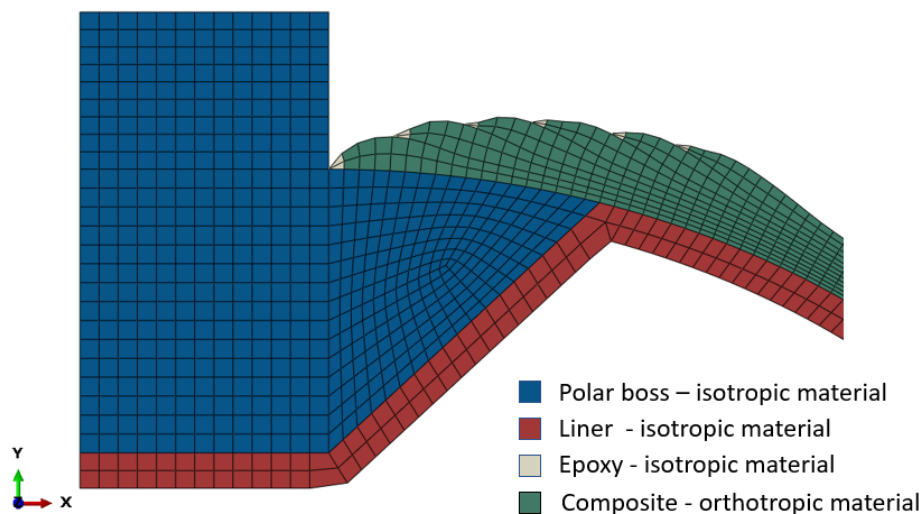


Figure 3.12: The four different material types present in the FEA model

Boundary conditions

To further reduce the size of the model, symmetry in the radial direction at the bottom of the cylindrical section is used to only model half of the cylinder. In an ideal case the winding pattern will be exactly the same on either side of the CPV. However, in reality it is usually quite difficult to obtain an exact symmetric pattern, due to variation in tow-preg width, incorrect robot calibration etc. This could result in differences between the experimental and numerical model. The symmetry is achieved by restricting the translation and rotational freedom in the z-direction. A natural symmetry condition is imposed on the left-side of the polar boss, because it is located on the symmetry axis. This ensures that this side does not move in the radial direction, but can only expand longitudinally. An inner pressure is applied to the inner side of the liner. Here, it is important that the correct element definition is used, such that the inner pressure is applied at the correct element face.

All the above data is written to an input file, which can be imported into Abaqus or directly be used to calculate the stresses and strains for every element. In this thesis the input file is automatically transferred and run on the TU Delft cluster using Python. The results are then fetched from the FTP and post-processed to evaluate failure of the CPV. The above procedure is also illustrated in Figure 3.13.

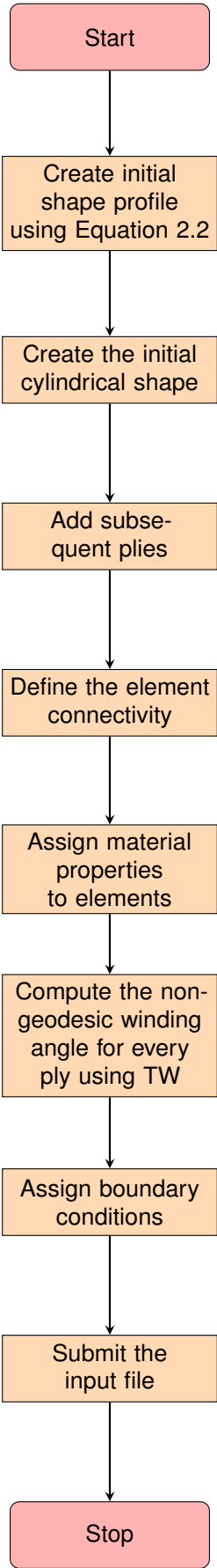


Figure 3.13: Flowchart of the creation of the input file

3.2.3. Thickness variation on the dome

In the dome section, as a consequence of the continuous nature of FW, a thickness build-up is created near the polar boss. This thickness can not directly be added to the previous shape profile. The calculated thickness should be added perpendicular to that particular position. This requires the normal, which can be obtained by firstly taking the difference between two subsequent points. Next, the length between two points should be normalised, which requires the length of that vector, as defined by:

$$|\vec{v}| = \sqrt{d_r^2 + d_z^2} \quad (3.8)$$

where d_r and d_z are the difference in r and z coordinates between two adjacent nodes. Using the length between two nodes the vector can be normalised by dividing by its length:

$$\vec{n} = \frac{\vec{v}}{|\vec{v}|} \quad (3.9)$$

To obtain the normal to the vector along two points, the r and z coordinate should be swapped, or equivalently rotated 90 degrees. The normal vector is required to correctly add the thickness of the subsequent ply to the previous shape profile. For every element the normal should be computed to get the correct new shape profile along the meridian profile on the dome. Care should be taken that the rotation is in the correct direction. Subsequently, multiplying with the thickness at that position, as calculated by an analytical method and adding the coordinates of the previous position, leads to the new coordinates, as described in Equation 3.10

$$\begin{aligned} \vec{v} &= \begin{Bmatrix} d_r \\ d_z \end{Bmatrix} = \begin{Bmatrix} -d_z \\ d_r \end{Bmatrix} \\ \begin{Bmatrix} r_{new} \\ z_{new} \end{Bmatrix} &= \begin{Bmatrix} -d_z \\ d_r \end{Bmatrix} t(r_i) + \begin{Bmatrix} r_{old} \\ z_{old} \end{Bmatrix} \end{aligned} \quad (3.10)$$

where $t(r_i)$ is the thickness at the i^{th} point. The process described above is illustrated in Figure 3.14 and Figure 3.15.

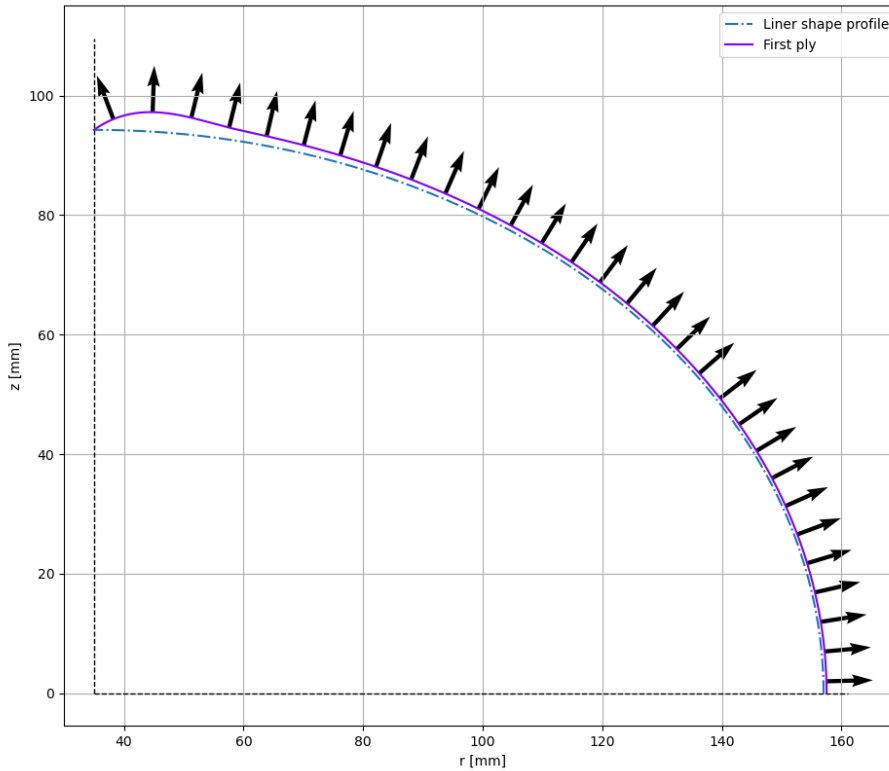


Figure 3.14: Definition of the normal vector along the dome section

As already highlighted in Section 2.6, various analytical descriptions exist to describe the thickness in the dome section. Most have a deficit that the thickness approaches infinite near the polar radius. This is mitigated by Wang et al [52] and Vasiliev et al [51], by using a cubic spline approximation, from the polar boss until two tape distance. This reduces the error between reality and the analytical approximation. A similar method has been used by Nebe et al [35], showing a high degree of correlation with the experimental results. Several aspects have shown to have an impact on the thickness distribution, such as [35, 57, 52]:

- Resin outflow due to viscous deformation of the uncured material
- Ply readjustment/realignment
- FW parameters, i.e. tension and dwell angle
- Tape width

However, as stated in Section 2.6, both methods assume a geodesic winding pattern. This thesis aims to review the effect of changing the winding angle to reduce the material usage. Though, if the true angle is used instead of the geodesic winding angle a mismatch in thickness is created at the dome-cylinder interface, because the analytical formula is only applicable for geodesic winding. Therefore, in this thesis Wang's formulation is used, using the assumption that the winding is geodesic. This will result in a small deficit in thickness distribution on the dome section, hence a difference in mechanical properties. Otherwise, the thickness mismatch would result in unfavourable stresses created at this junction. This assumption leads to the fact that a change in winding angle, does not result in a change of weight. However, for a lower winding angle than the geodesic winding angle, the effective width is lower, resulting in the need of more winding loops and thus a higher thickness. The contrary is true for higher winding angles than the geodesic winding angle. To obtain the correct weight for a single ply on the dome section, the path length is computed in TW and multiplied with the number of required loops to achieve a 200% coverage, as described in Section 2.5.3.

As already stated the thickness distribution on the dome inherently has an effect on the mechanical response. The thickness build-up on the dome, primarily on the polar boss, becomes excessive for many plies. To avoid this stepbacks are introduced in the model. After the winding of one sub-laminate of helical and hoop plies a stepback is applied. The position of the subsequent plies are placed at a distance of two tape-width, to create a uniform thickness on the polar boss.

Also, ply realignment and excessive thickness build-up on the dome could develop, if insufficient stepbacks are performed during the FW process. However, it should be reviewed after the experimental evaluation if more stepbacks should be executed. Failing in to do so could lead in deterioration of the mechanical properties, due to resin-rich areas.

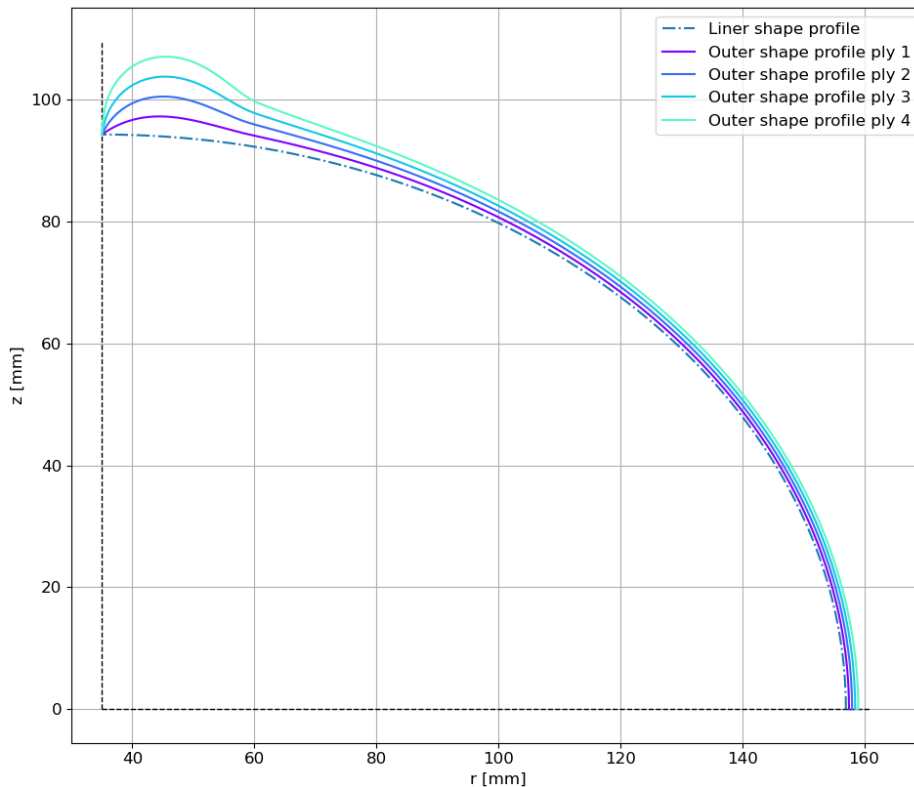


Figure 3.15: Stacking of several helical plies on the elliptical dome shape

Next to the step-back of the helical plies to reduce the thickness build-up, also hoop plies are dropped. Using hoop plies on the dome section has multiple beneficial effects. Here, the stiffness can be increased, alleviating the strains and stresses in this critical area. However, the position until which hoop plies can be wound are based on the available friction. The required friction on the cylindrical section is zero. However, this quickly increases if hoop plies are wound on the dome section. Therefore, during the analysis it is checked how much friction is required to wind a hoop ply on the dome section.

As already stated in Section 3.2.2, the ply ends of a helical and hoop ply are isotropic epoxy elements. This simulates that at these regions resin-rich areas are present. Several guidelines exist to mitigate premature failure or stress concentrations. These can be summarised as follows [21]:

- Avoid any external ply-drops, because this might induce delaminations
- The distance between two successive drop-offs should be 10-15 times the ply thickness
- Do not drop more than 0.5 mm in height at once, to reduce the creation of inter-laminar stresses

3.2.4. Implementation of non-geodesic winding angle

In this thesis the in-house software *TaniqWind* (TW) is used to compute the winding angle variation along the dome. Here, the shape profile is required to be defined in (z,r) coordinates, where z should be monotonously increasing. An adaptive numerical scheme is used to solve Equation 2.25, in which the step size is reduced in more difficult areas, such as on the polar boss, where the winding angle approaches 90 degrees. This adaptive scheme is used to minimise the computational effort to solve the differential equation. It is possible to define the initial winding angle, on the cylinder, and final winding angle (90 degrees), through which the software computes the required friction. This is used to validate if a defined winding angle, on the cylindrical section, is possible to be wound on the dome section, with the available friction.

Furthermore, TW is built using Matlab. Therefore any data exchange from the Python code, is done by using a shared session and running the Matlab script (TW) from Python. Through this, the winding angle distribution and required friction for any shape profile can be extracted. An example showing the variation of the winding angle is illustrated in Figure 3.16. Here, every element on the dome section has

its own material property and orientation. Any identical colour on the dome section does not imply that these elements have the same orientation.

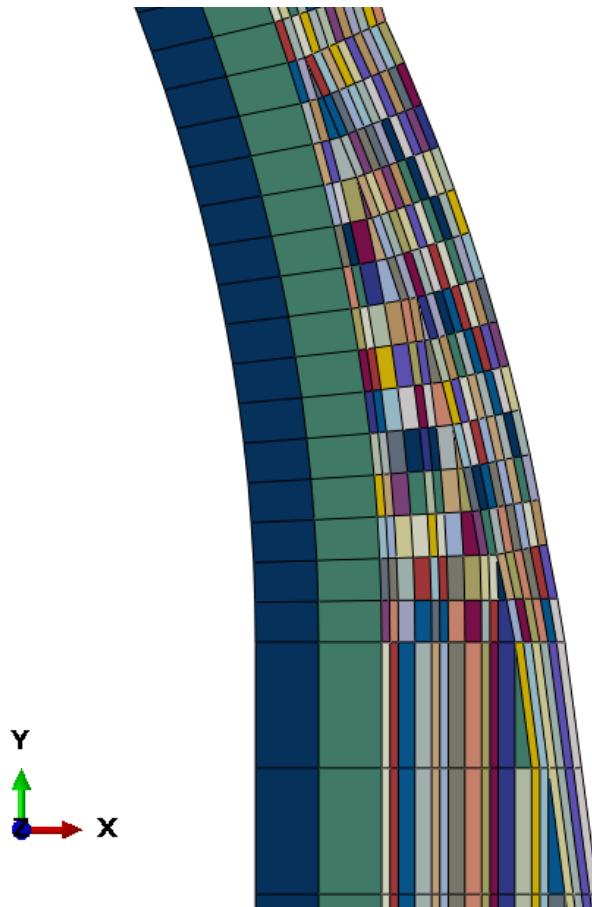


Figure 3.16: Variation of the winding angle, assigned to each element using a set

As explained in Section 3.2.3, the thickness of a ply depends on the shape profile of the previous ply. This might result in instabilities at ply ends on the polar boss, due to a decreasing z-coordinate. If the z-coordinate is decreasing, it is changed according to the average change of the previous two shape profile points, as follows:

$$z_k = z_{k-1} + (z_{k-1} - z_{k-2}) \quad (3.11)$$

where k is the point at which z decreased with respect to the previous point (k-1). This procedure is only used for a few points on the polar boss where the z-coordinate decreased as opposed to the previous point. Physically, a decreasing z-coordinate implies that the shape profile changes from convex to concave, resulting in bridging of the tape [23]. Therefore it is not possible to get a feasible winding path, using FW, for such a shape profile.

Some instabilities may occur during importing of the shape profile into TW, using insufficient number of sampled shape profile points, which is solved by discretising the shape profile with more sample points, using a B-spline from the scipy package¹ in Python. This spline is a linear combination of the sample points, or deBoor points [26]. The B-spline is used because it has a high stability and is able to accurately represent the original shape profile with more points.

From the resulting winding angle variation, calculated in TW, samples are taken at the centre of the element. However, at the polar boss the winding angle changes rapidly. Therefore, a slight change in the z-coordinate, results in a big change in the winding angle. This is illustrated in Figure 3.17. Near the

¹<https://docs.scipy.org/doc/scipy/reference/generated/scipy.interpolate.BSpline.html>

polar boss, the inner side of the tape approaches 90 degrees, while the outer side has a lower angle. In this thesis the inner side of the tape is taken as reference point for the winding angle. This is done because, using FW, the tape should approach 90 degrees to create a continuous winding path. The structural response in the region of the polar boss is neglected, because this area is prone to many imperfections, such as resin-rich areas and ply realignment [35].

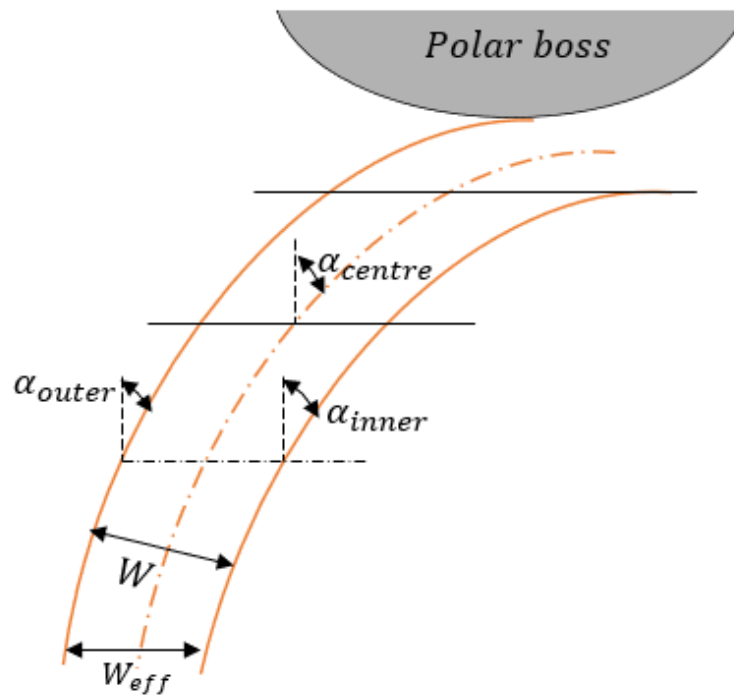


Figure 3.17: Difference in winding angle at the same longitudinal position

Currently, the winding angle is computed using a non-geodesic algorithm in TW. This approach calculates the winding angle based on the derivatives of the shape profile. An example for the variation of the winding angle, using TW, is shown in Figure 3.18. This illustration shows the difference between two methods. The blue line uses constant friction throughout the winding path, while the dotted orange line uses a constant in-plane curvature. Here, the in-plane curvature is defined as the tangential curvature or geodesic curvature, with respect to the supporting surface [23], defined as R_g in equation Equation 2.24. Using constant friction results in a 2% shorter path, but also a 6% lower minimum winding angle, for this specific profile and winding angle. This effect can be beneficial near the dome-cylinder interface, to have a better performance for the induced bending stress, this will be further discussed in Section 3.3.

Remarkably, the winding angle decreases initially, from the cylindrical section (left), because of a low rate of change and curvature of the elliptical shape. Therefore the geodesic effect is low, but the frictional component is larger, resulting in a decrease of the winding angle. However, the geodesic part (second term) of Equation 2.25 increases with a decrease in radial position and an increase of the rate of change of the profile. A change in direction of the winding angle is observed from around $z = 60$ mm. The minimum of the winding angle can be minimised by increasing the geodesic effect, i.e. reducing the eccentricity of the ellipse.

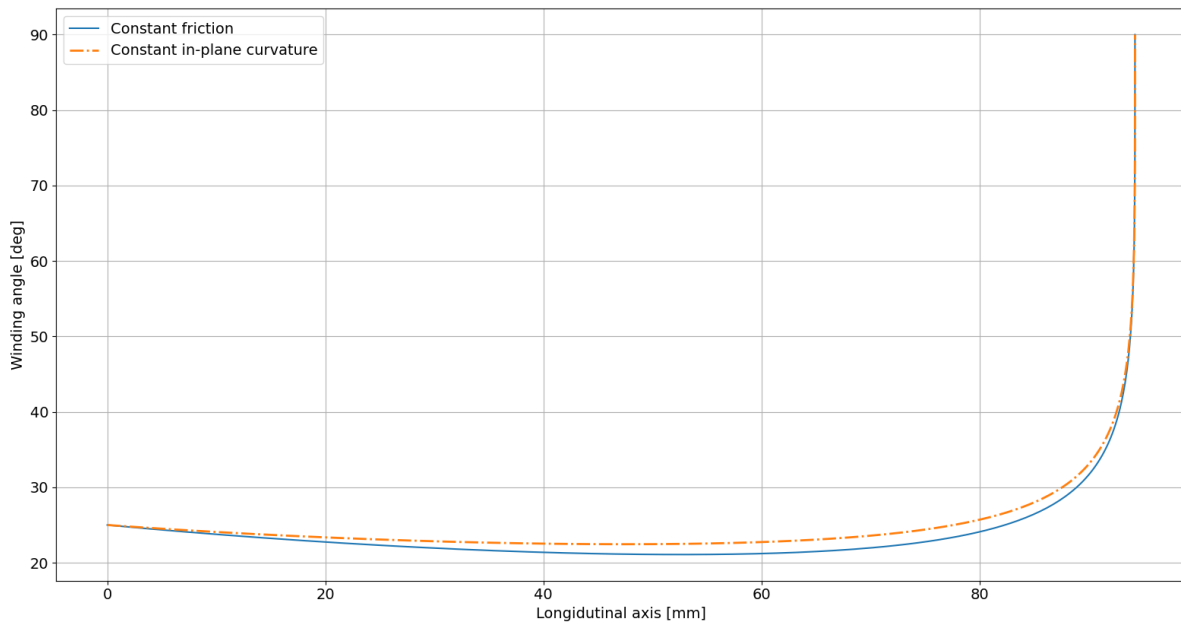


Figure 3.18: variation of the winding angle with a distinctive local minimum

3.2.5. Mesh convergence analysis

The previous chapter (Section 3.2.1) showed that the axisymmetric element has a high accuracy, with respect to the analytical method, and requires a low computational effort. Here, the analytical method is derived using an exact differential equation to solve the stresses and strains on a closed cylinder, i.e. modelling a CPV. Therefore the solution is assumed to be the theoretical solution of the stresses and strains on the cylindrical section. However, in Section 3.2.1 solely the cylindrical section is modelled. Therefore in this section the full CPV is modelled in FEA, to assess the minimum required of elements required to accurately describe the stresses and strains in the CPV. This procedure is split into two procedures, namely mesh convergence on the cylindrical section and mesh convergence on the dome section. This is done because the cylindrical section is a part of the CPV which does not have many intricate modelling issues, while the dome section needs to account for drop-down region, change of curvature and non-geodesic winding angles. The number of elements in the FEA elements are defined by the number of nodes in the dome section and the number of nodes on the cylindrical section. For this mesh convergence analysis a four ply stacking sequence will be modelled, namely $[55, -55] + [90, 90]$, using the orthotropic material properties defined in Section 2.2.

The first mesh convergence is performed on the cylindrical section, depicted in Table 3.6. The inner pressure applied is 10 MPa and the orthotropic material properties, as defined in Section 2.2, are used to define the engineering constants in Abaqus. For every subsequent mesh the element length is halved. The stress results of the FEA model are assessed at the bottom of the FEA model, i.e. the centre of the cylindrical section. This is done to observe the stress state without any disturbances due to the dome. It is observed that the axial, hoop, radial and in-plane shear stress do not deviate significantly with decreasing mesh size, however, the intra-laminar shear stresses do deviate. This is probably because the magnitude of these stresses is very small. This can also be seen in the change of the FI. Where the significant change in intra-laminar stresses does not result in a change in FI. The mesh convergence analysis on the cylindrical section shows that using an element size of 10 mm is sufficient to accurately describe the stresses. Also, a decrease in the element size and thus in the amount of elements does not increase the computational time of the analysis. It should be noted that the reported computational time is the wall-clock time and the processing time is usually lower.

Table 3.6: Mesh convergence analysis on the cylindrical section using the analytical model

	Element size	σ_z	σ_θ	σ_r	$\tau_{z\theta}$	$\tau_{r\theta}$	τ_{rz}	FI	Comp. time
	mm	MPa						-	s
Analytical	-	1023.92	191.06	-7.95	222.58	-	-	1.86	0.05
	20	1045.84	191.57	-7.95	230.73	-0.060	0.086	1.83	0.72
Mesh	10	1033.09	191.31	-7.96	226.09	-0.010	0.061	1.84	0.76
	5	1029.36	191.22	-7.95	224.69	-0.009	0.047	1.84	0.94
	2.5	1027.60	191.17	-7.95	224.01	-0.0007	0.011	1.85	1.02

The mesh convergence analysis for the dome section is shown in Table 3.7. The reported stresses are rotated from the local ply system, as calculated by Abaqus, into the global system, similarly as done for the cylindrical section. A similar trend is observed as the mesh convergence analysis for the cylindrical section. The stresses do not change significantly from the second mesh and forth. However, the number of required elements are doubled. The number of elements stated in Table 3.7 are the total number present in the model. For the current analysis this still results in a very low computational time. If a very thick laminate is modelled the computational time may be reduced by discretising the dome section with less elements, while maintaining sufficient accuracy. This can be done by using the third mesh. Using more elements also results in a more accurate description of the elliptical dome shape, as defined in Equation 2.2. This inherently also leads to a better representation of the change of winding angle along the meridional path, as reviewed in Section 3.2.4. Because more winding angle samples are taken from TW. The change of the FI for an increasing mesh size for both studies are shown in Figure 3.19. Here, the FI is maximum on the cylindrical section, because the same number of hoop and helical plies is used, while the hoop stress is twice the magnitude.

Concluding, the stress-state showed a high convergence rate on the cylindrical section. For this section the element size is chosen to be 5 mm. Using this element size results in good correlation with the analytical model. Furthermore, more variation of the stress state is observed for the mesh convergence analysis of the dome section. This section is prone to irregularities in the stress state, due to varying stiffness, winding angle and voids. But, from mesh 3 and onward the main stresses do not deviate significantly and the FI converges. Therefore, mesh 3 is chosen for the dome section, which corresponds to 90 nodes.

Table 3.7: Mesh convergence analysis on the dome section, without the consideration of the elements on the polar boss

Number of el.	σ_z	σ_θ	σ_r	$\tau_{z\theta}$	$\tau_{r\theta}$	τ_{rz}	FI	Comp. time
-	MPa						-	s
662	1094.39	143.65	1.76	-279.56	69.95	-20.29	1.49	0.72
986	1180.82	155.31	0.32	-271.66	38.14	-9.18	1.14	0.76
1390	1200.81	158.62	-0.81	-267.46	23.25	-5.96	1.07	0.94
1978	1231.29	161.88	-2.85	273.69	14.74	-5.13	1.06	1.02

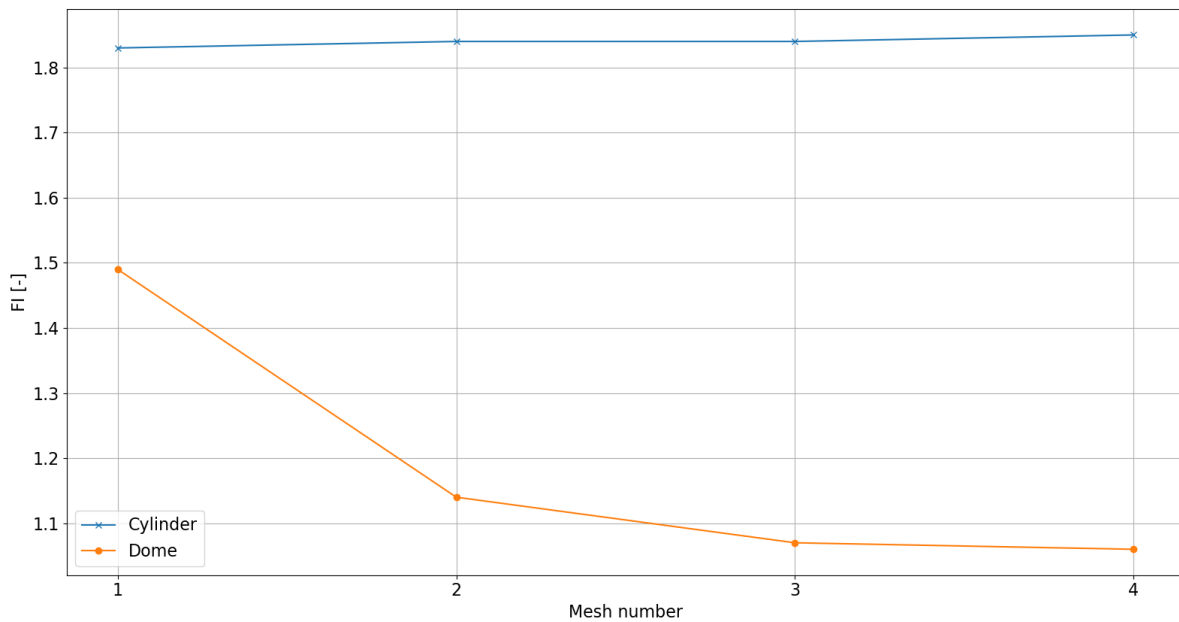


Figure 3.19: Plotted summarised data of the mesh convergence analysis

3.3. Correlation of the analytical model with FEA

In Section 3.1.3 various stacking sequences have been evaluated for their performance using the analytical tool. Consequently, in Section 3.1.4 it was shown that the classical netting-analysis yielded a non-conservative thickness to attain a defined burst pressure. In this section the developed FEA model will be used to review the obtained results for the stacking sequence effect and observe if there is any correlation. From this, the general behaviour of the CPV is reviewed splitting the CPV in two sections. Lastly, a final baseline design will be created using the FEA model.

3.3.1. Stacking sequence effect

In Section 3.1.3 various laminates have been assessed for the effect of grouping and positioning of the plies. The same procedure is performed in this section, but using the developed FEA model. The results are shown in Table 3.8. Here, the analysis is performed using a friction coefficient of 0.2 and 0.5, which applies to wet-winding and tow-preg winding, respectively. The difference between the two models is the position of the hoop plies on the dome. Using 0.2 friction results in only one hoop ply on the dome section, which is wound until $z = 5$ mm. Using 0.5 friction gives the ability to position 5 plies on the dome, until $z = 25$ mm. Due to this the stresses generated near the dome-cylinder interface can be reduced, which can be seen in the difference between the maximum FI on the dome and cylinder, because the stiffness reduction is minimised by positioning the hoop plies further on the dome. Also, a large difference in FI can be observed, comparing the analytical model and the FEA model. This is because the analytical model does not consider the discontinuity stresses generated at the dome-cylinder interface, which results in an increase in the axial, hoop and intra-laminar shear stresses. The bold faced values in Table 3.8, indicate the highest performing stacking sequence for that model. Thus, laminate A has the highest performance using the analytical model and laminate C minimises the FI using the FEA model. It should be noted that currently the laminate thickness is computed by multiplying the number of plies times the single ply thickness. However, in reality the underlying plies are compressed and are less thick [33, 56]. The thickness of a ply depends on the compaction force and depends on the winding angle of the ply. Higher winding angles exert a higher compressive force on the underlying plies, resulting in a thinner ply and a higher fibre volume fraction [36].

In conclusion, laminate C performs the best in both situation, in which all the helicals are positioned on the inside and the hoop plies on the outside of the laminate. The bending stiffness of the helical plies are increased by positioning these on the inside, i.e. from the mid-plane. At the critical area, near

the dome-cylinder interface, the axial stress increases rapidly due to an strain compatibility between the dome and cylinder, further discussed in Section 3.3.3. Near this section the hoop stress also reduces from mainly hoop dominated to axial. The other laminates mainly have a higher FI, because of intra-laminar stresses. Here, on the cylindrical section, ply ends of the hoop ply are present with a very low stiffness, resulting in a significant deformation. This can be mitigated, as done for laminate C, by positioning the hoop plies on the outside. Furthermore, laminate A and D fail due to the hoop plies being loaded on the matrix at the inner side of the laminate, due to the generated bending stresses. Lastly, laminate B also shows a good performance. The inner hoop plies fail due to the generated bending stresses. Thus, it is important to correctly position and group plies, such that these are loaded optimally. Here, a higher axial stiffness is required on the inside of the laminate for the created discontinuity stresses. On the cylindrical section, the stress-state is predominantly in the hoop direction. This can be alleviated by correctly positioning the hoop plies, such that these do not fail by the generated axial bending stresses, but add stiffness in the tangential direction to reduce the hoop strain.

Table 3.8: Correlation of FI between the analytical model and FEA model for two different friction coefficients, using $P = 35$ MPa and $t = 11.88$ mm

	Analytical	$\lambda = 0.2$				$\lambda = 0.5$			
		Cylinder		Dome		Cylinder		Dome	
		FI	Position (z)	FI	Position (z)	FI	Position (z)	FI	Position (z)
A	0.310	4.40	-5	6.99	1.73	1.68	-5	1.4	22.9
B	0.313	4.75	-5.0	5.82	1.73	1.21	-5.0	0.93	22.0
C	0.316	1.44	-10.0	1.01	1.67	1.03	-10	0.54	1.67
D	0.320	5.14	-5.0	8.01	2.0	2.01	-5.0	1.75	22.0

3.3.2. Final baseline design

Similar to the analytical model, the baseline design is created using the highest performing laminate in Section 3.3.1, namely laminate C. This laminate has all the helical plies on the inside and the hoop plies on the outside. It is important to note that the evaluation of the stacking sequence in Section 3.3.1 and Section 3.1.3 only reviews four different laminates. Actually there are many different factors which could further improve the performance of the laminate, such as the helical winding angle. This would however be impractical to evaluate, because there are numerous options. This will therefore be evaluated in Chapter 4. Following this, the number of required plies, of laminate C, are alternated until a valid solution is found, i.e. $FI < 1$. The resulting laminate is defined as:

$$[10, -10]_5 + [90, 90]_7 \quad (3.12)$$

where the maximum FI equals 0.94, on the cylinder at $z = -20$ mm, in the outer hoop ply. The FI indicates that there is remaining strength in the laminate. However, discarding of a sub-laminate results in failure. This is because the single ply thickness is relatively thick, which reduces the design freedom and possibly increases the total composite weight. Furthermore, it is observed that the traditional 2:1 ratio of hoop to helical plies is not present anymore. This is because near the dome-cylinder interface the meridional stress component increases, due to the induced bending stress. Therefore, it is necessary to position the helical plies on the inside. Because the bending stiffness is increased by placing the helical plies as far as possible from the mid-plane, increasing the D matrix. Beneficially, it has been found [35, 36] that positioning the hoops on the outside results in a lower laminate porosity and a higher fibre volume fraction. This increases the mechanical performance of the laminate. However, there are no overlapping helical plies present at the drop-off region of the hoop plies and this could result in pre-mature delaminations [21].

Furthermore, the FI is maximal on the dome-cylinder as expected and further reviewed in Section 3.3.3. Thus, the design of a CPV is driven based on the requirements of the stacking sequence at the dome-cylinder junction. Reducing the FI on this section will result in an optimal CPV. However, in this thesis elements failing above $z = 85$ mm, i.e. at the polar boss section, are neglected. While actually many phenomena, such as helical drop-off, resin rich areas and axial displacement of the boss may be constraining factors in the design of a CPV. This is because the behaviour at the boss section is

difficult to predict using numerical models, due to the aforementioned effects. The variation of the local stress components of the baseline design are illustrated in Figure 3.20 and Figure 3.21. Here, 17 lines are shown, i.e. 10 helical plies and 7 hoop plies, because the hoop plies are modelled as 200%. The FI is shown in Figure 3.22. Here, it can be seen that the FI is maximal on the interface, in the hoop plies. While the FI on the cylinder is lower and has remaining strength. Following this, the FI on the polar boss is disproportionate. This is why this section is neglected. Also, because it is expected that the stainless-steel boss has sufficient strength to mitigate failure in this section.

The final thickness of the CPV can be computed by multiplying the required number of plies times the ply thickness. The results are presented in Table 3.9. Furthermore, using the procedure as explained in Section 2.5.3 and multiplying the total length of all plies, as computed by TW, with the thickness, width and density results in the total weight of the composite. For this design the total weight of the composite is: $W = 9.13$ kg.

In Table 3.9 a significant thickness increase of 25% is required to mitigate failure in the FEA model. This implies that the FEA model is more conservative than the analytical model, because it requires more plies to attain the same burst pressure. However, in Figure 3.20 it can be observed that the stresses increase at the dome-cylinder interface. This is true for all stresses. The increase in stress is observed in the FEA model, because at this section several phenomena are occurring, such as ply drop-off of the hoop plies, non-geodesic winding angle on the dome and bending stresses are induced due to strain compatibility of the dome and cylinder. All these effects are not considered in the analytical model. Which can be seen in Table 3.6. Here the cylindrical stresses of the analytical model correlated with the cylindrical stresses of the FEA model. Thus, the result depicted in Table 3.9 are expected, because the stresses in the analytical model are less conservative than the stresses in the FEA model and this can mainly be attributed to the stress state at the dome-cylinder junction. Furthermore, the FPF occurs at the cylindrical section at a hoop ply. Both effects are desired. Here, Madhavi et al [32] states that the failure of a hoop ply is more predictable. Additionally, the failure of a CPV should occur on the cylindrical section, as otherwise boss blow-out may occur. This failure mode should be mitigated because it could cause damage to the surroundings [27, 18]. Another beneficial effect is that the hoop plies compress the inner helical plies, which result in a lower porosity and higher fibre volume fraction [36]. This results in an improved mechanical response of the CPV.

Table 3.9: Overview of the different required thickness between the analytical model and FEA for $P = 35$ MPa

Analytical	FEA	Difference
mm		%
5.94	7.92	+25

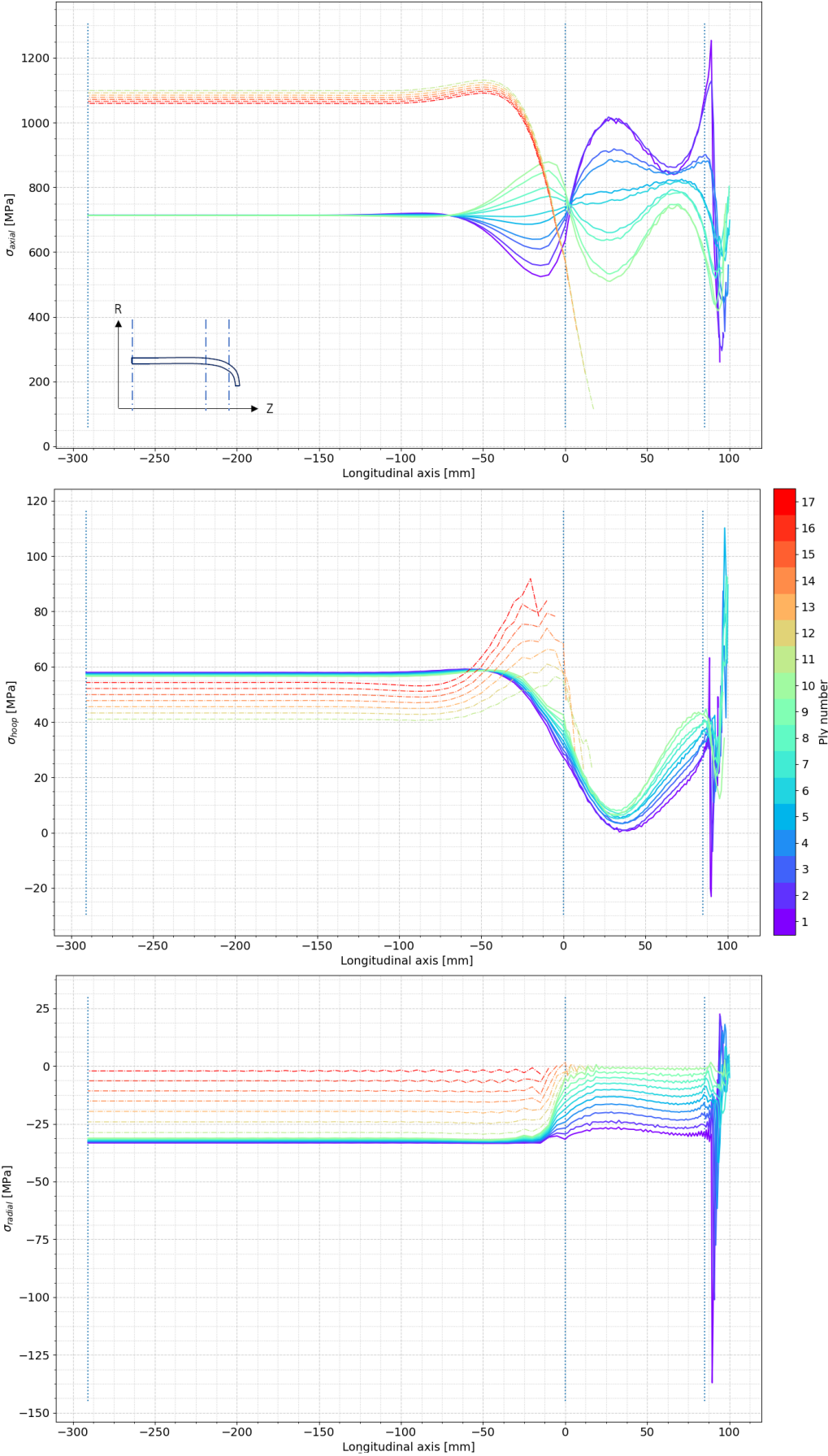


Figure 3.20: Local stresses of the baseline design

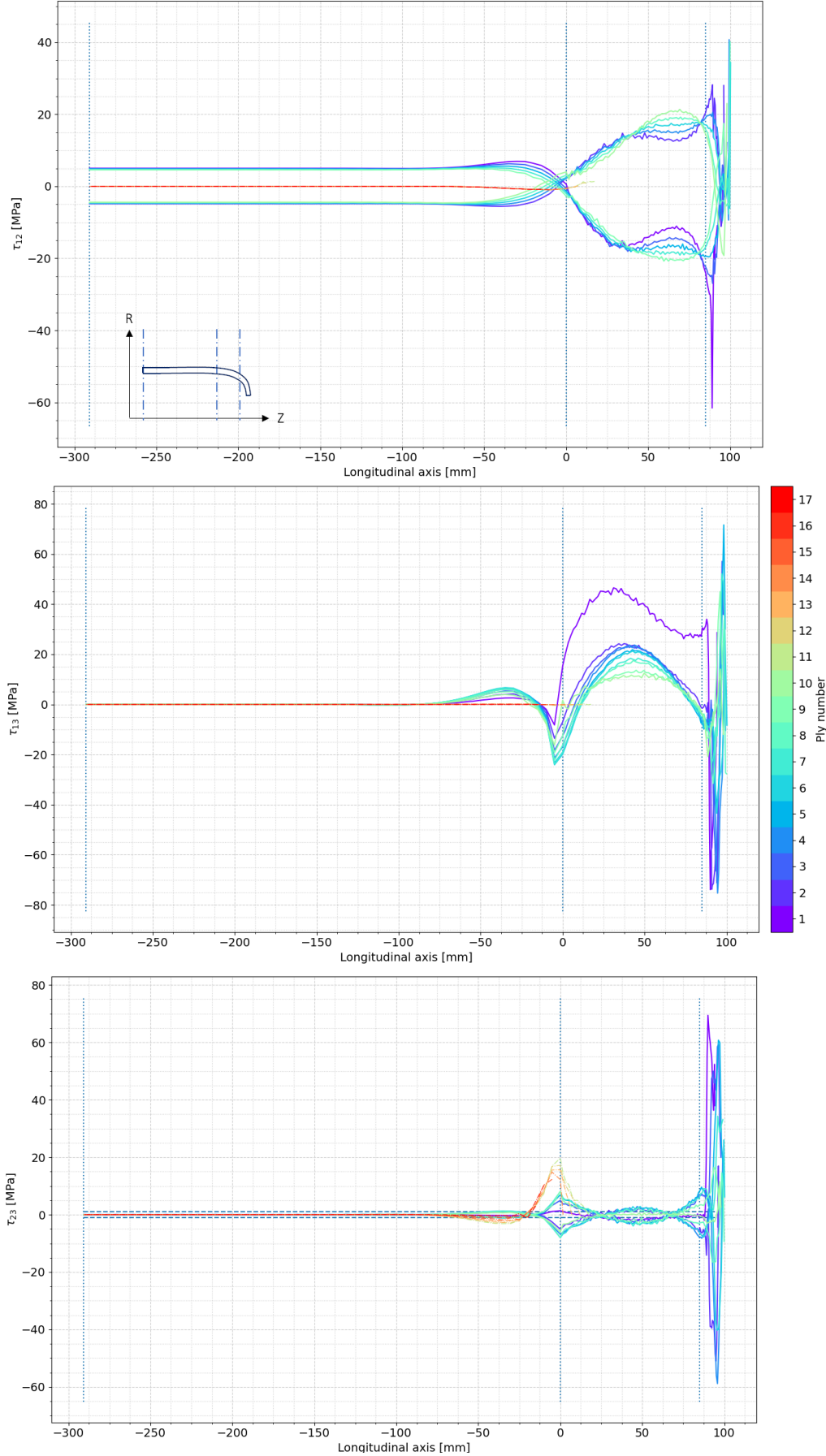


Figure 3.21: Local shear stresses of the baseline design

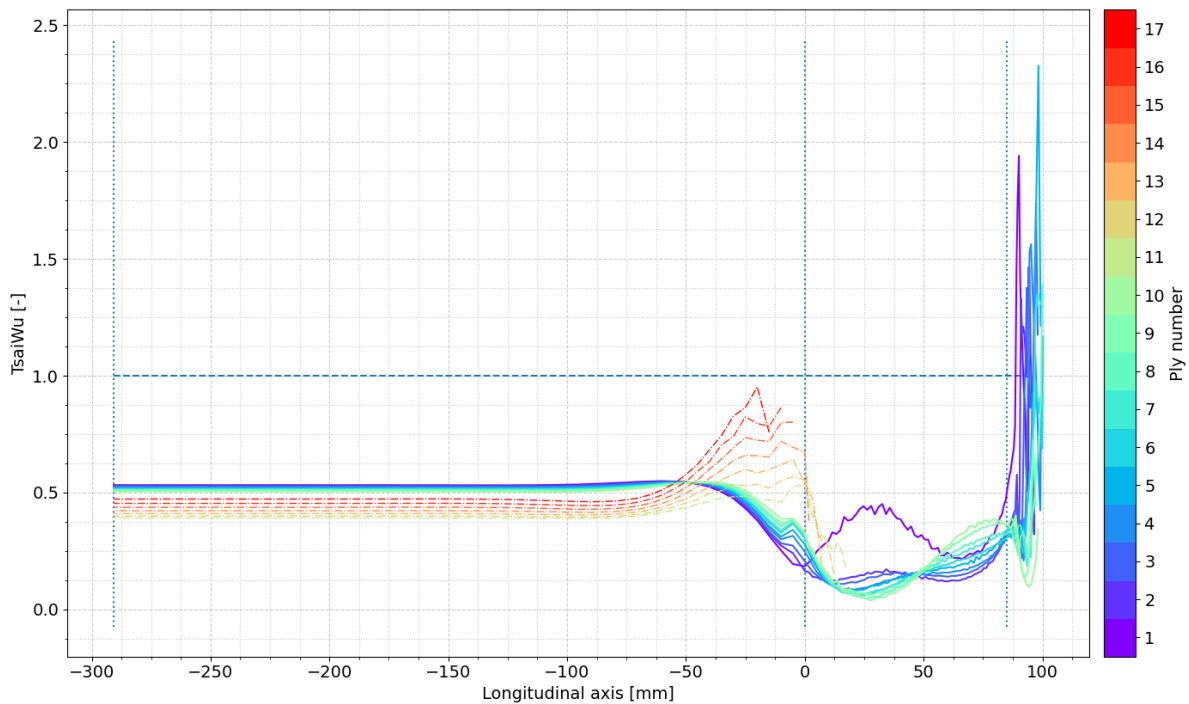


Figure 3.22: Variation of the FI along the longitudinal direction for all plies

3.3.3. General CPV behaviour

In the analytical method the strains only varied as function of the radial position. The FEA model makes it possible to review the stress variation also along the longitudinal direction, as depicted in Figure 3.24 and Figure 3.25. Here, the helical plies and hoop plies are represented by a solid line and a dotted line, respectively. The blue line indicate the most inner plies, while red line the most outer plies. The strains are rotated from the local to the global coordinate system and are obtained for $P = 35$ MPa and the stacking sequence defined in Section 3.3.2. In this chapter the strains are discussed and divided into two segments, the cylinder and the cylinder-dome interface.

Cylinder

The cylindrical section is characterised by constant material properties and a geodesic winding angle, i.e. constant winding angle. The predominant radial expansion results in a negative radial strain component [35]. The compressive strain occurs due to the tangential and radial expansion, thus a thinning of the laminate. Contrarily, the axial and hoop strain are both tensile, similarly for thin-walled CPVs. Following this, the hoop strain decreases through the thickness of the laminate, which is recognisable for the thick-walled effect.

From $z = -100$ mm and below the strains are constant and do not deviate. This means that circa 35% of the cylindrical section is subjected to a constant stress state. This result is important, because if the cylindrical section would have been shorter than the distance in which the stresses become constant, discontinuity stresses could be superimposed. This could induce that the cylindrical section could fail prematurely. The constant nature of the stresses on the cylindrical section impose that the cylinder load and boundary conditions are symmetric in nature, because the development of any bending is mitigated [35].

The used stacking sequence does not have a 2:1 ratio of hoop to helical plies anymore. This can be seen by comparing the hoop vs helical strain. The hoop strain is about 1.5 times larger than the axial strain.

Cylinder-Dome

The most prevalent behaviour occurs on the cylinder-dome intersection. On this section material inhomogenities occur due to non-geodesic winding angle, doubly curved supporting surface and varying stiffness due to hoop drop-offs. These effects result in local changes of stiffness along the meridional path. Nebe et al also [35] stated that the fibre volume and porosity changes in this section due to the

non-geodesic winding angle and curved surface. Because a different winding angle, imposes a different compression force on the underlying plies.

In this section strain compatibility exists between the cylinder and dome, as shown in Figure 3.23. The dome is characterised by an axial displacement, while the cylindrical section expands radially [5]. Therefore, a restriction is imposed on the radial expansion by the dome head. The differences in displacements are matched with a meridional bending component. This is also clearly seen in the Figure 3.24. In the cylindrical section the inner plies are less strained than the outer plies. Implying an outward bending component on the cylinder. Vice versa, on the dome the inner plies exhibit a maximum, indicating an inward bending component.

The hoop strain increases slightly near the intersection, which is a result of the induced stress by the Poisson effect. However, a decrease is seen on the dome. This is a result of the change from a pre-dominant tangential loading to axial loading on the dome. Due to this change in loading, the dome section desires to deform into a cylindrical section, i.e. an upward bending moment is induced at the polar boss.

In Figure 3.25 various shear strain components are shown. The τ_{13} component is induced by the hoop drop-off present in this section, i.e. a reduced stiffness. It is also induced by the resulting bending stress from the strain compatibility between the dome and cylinder. Furthermore, τ_{23} is due to torsion of the CPV. These results shows that torsion is present in an axisymmetric CPV. Therefore, the axisymmetric element, which allows torque has been used. The torque is constant along the tangential direction, because it is an axisymmetric model. For opposing helical plies the strain magnitude is either positive or negative. Also the inner plies have a higher magnitude.

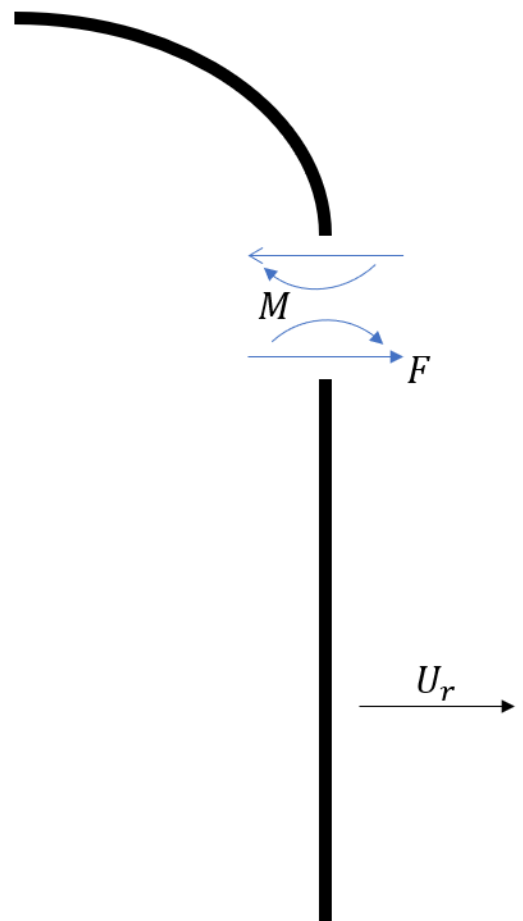


Figure 3.23: Schematic illustration showing the strain continuity between the dome and the cylinder

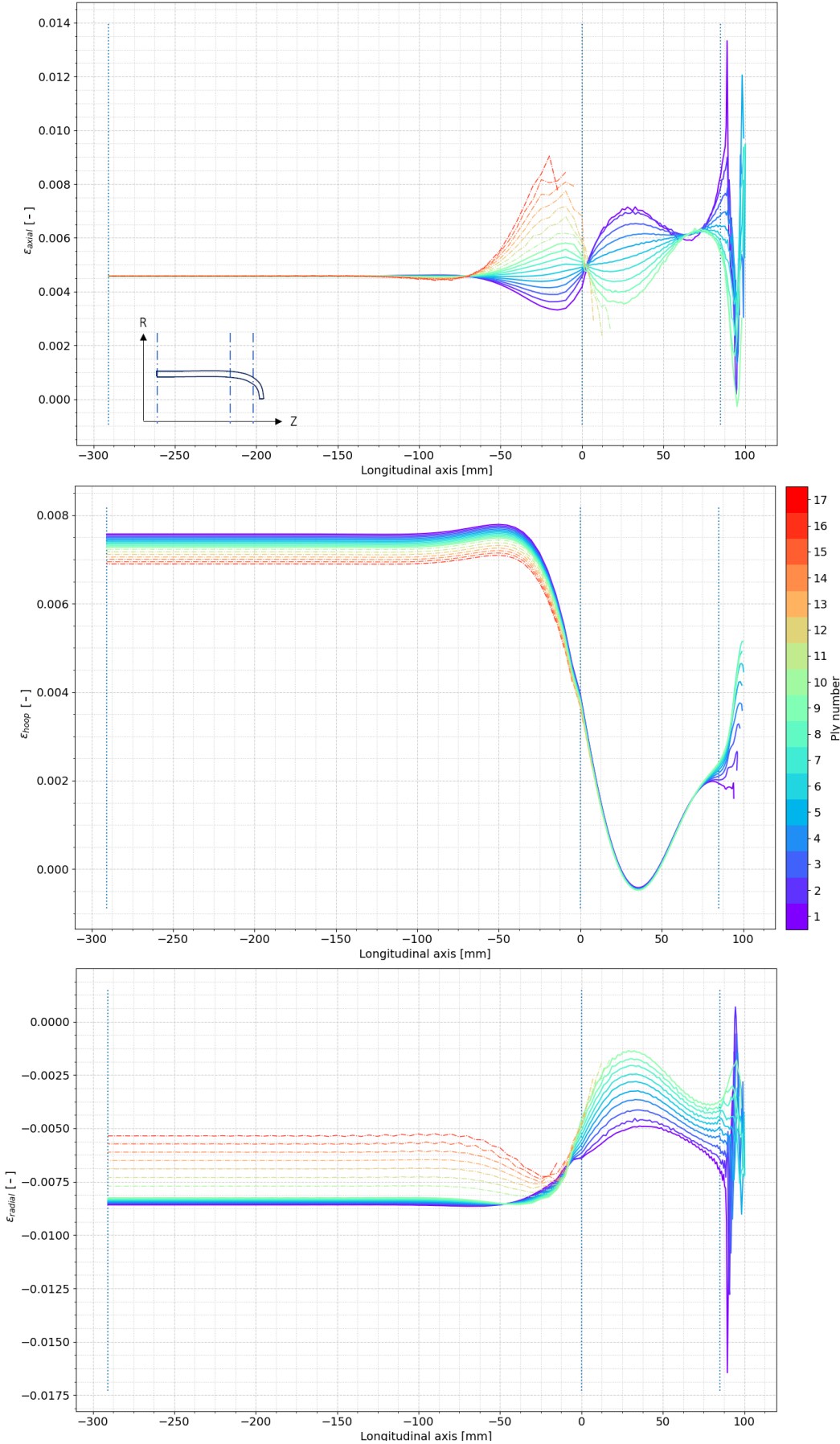


Figure 3.24: Global axial, hoop and radial strain along the longitudinal direction of the CPV

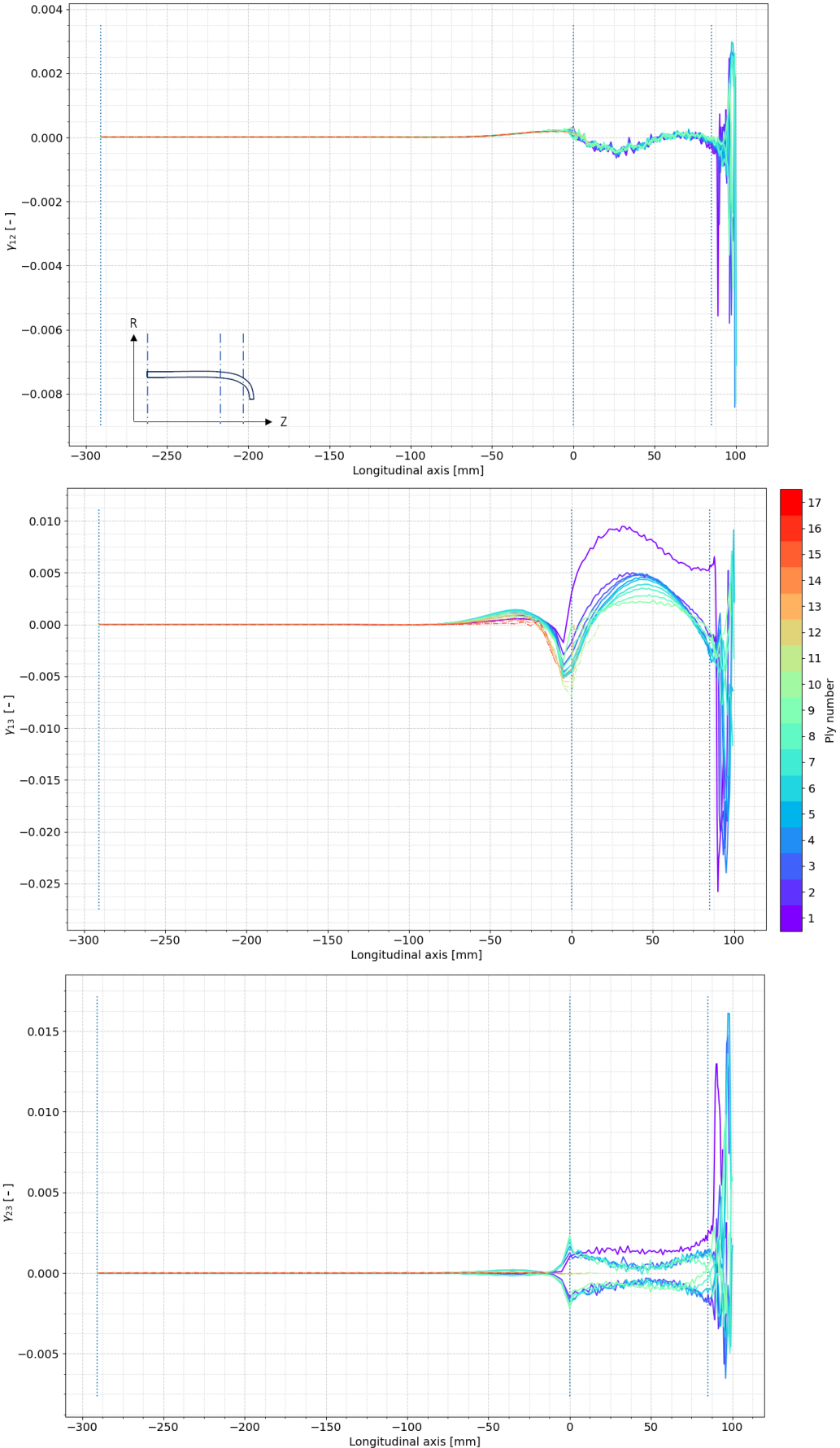


Figure 3.25: Global in-plane and out-of-plane shear strain along the longitudinal direction of the CPV

3.4. Conclusion

This chapter comprised two different methods to evaluate the stress-state in a CPV, to assess the required thickness, for a defined burst pressure. The first model is constructed using an analytical model. Contrary to the classical netting analysis, it does consider the contribution of the matrix, polymeric liner and through the thickness stresses. This is required because from an inner to outer radius ratio of 1.1 and higher, the stresses through the thickness become notable. Though, in this thesis the burst pressure has been reduced to $P = 35$ MPa, because it has been observed that the polymeric liner and polar boss release at around $P = 40$ MPa. Moreover, these effects have been observed in Figure 3.4. Here the axial and hoop strain are similar due to the used 2:1 hoop to axial plies ratio, where the axial strain is constant and the hoop strain decreases through the thickness. For thick-walled analysis the out-of-plane strain is characterised by its compressive nature, where a zero strain condition is imposed on the outside of the laminate.

To assess if a structure failed, a failure criteria should be employed. There is a wide variety of criteria available. From the WWFE it was shown that the Puck and Tsai-Wu failure criteria have high accuracy, with respect to the other evaluated failure criteria in the WWFE and the test data. However, it becomes more difficult to decide which criteria to use. Because there is no complete known experimental data of the failure of CPVs. Therefore, it has been decided to use the most conservative failure criteria, which is Tsai-Wu.

Following this, various stacking sequences have been evaluated to observe the effect of positioning and grouping helical and hoop plies. This showed that interchanging axial and hoop plies results in the lowest FI. However, the differences are minimal for the analytical method. Actually, the hoop strain defines the stacking sequence on the cylindrical section, as it has twice the magnitude with respect to the axial strain. This effect becomes more noticeable for thicker laminates which are subjected to higher internal pressures. Furthermore, hoop plies have a higher effectiveness on the inside of the laminate because the hoop strain decreases through the thickness.

Furthermore, a FEA model was constructed, in Section 3.2, which showed that the computational effort can be significantly reduced by using axisymmetric elements, while maintaining sufficient accuracy. To describe the mechanical response of a CPV several characteristic have been modelled, such as thickness build-up on the dome, drop-off for helical and hoop plies, creation of voids due drop-offs and non-geodesic winding paths on the dome. However, it is still observed that the dome section is very sensitive to changes in the intra-laminar stresses. This is a results of the varying stiffness due to the non-geodesic winding angle and change of curvature.

A similar stacking sequence evaluation is performed as in Section 3.1.3, using the FEA model. This model showed that the FI is minimised by positioning the helicals on the inside of the laminate and the hoops on the outside, a similar result was obtained by Asijee et al [36]. Here, the maximum FI is mainly dictated by the stresses near the dome-cylinder interface. In this section, bending stresses are generated, due to strain compatibility between the dome and cylinder. A outward bending moment is present on the cylindrical section, where the inner plies are less strained. Contrarily, an inward bending moment is present on the dome section. Therefore it is optimal to position helical plies as far from the mid-plane, on either side, to increase their efficiency. Furthermore, the analytical model showed that the design is mainly dictated by the hoop strain on the cylinder. Thus, positioning the hoop plies in the area of high strain would result in an optimal design. But in the FEA model, axial bending stresses are generated at the dome-cylinder interface. This results in the hoop plies being stressed in the matrix, on the inside and outside of the laminate. Therefore, positioning hoop plies on the inside results in failure of the inner hoop plies. Because the strength in the matrix direction is low. In Section 3.3.2 it can be seen that the hoop stress, is the highest in the outermost hoop plies. Which indicates that the hoop plies are loaded by the axial bending stress. However, the axial bending stresses are sufficiently alleviated by the helical plies. Furthermore, the designs with more hoop plies on the outside perform better, because at positions near the dome-cylinder interface voids are present due to hoop drop-offs. This results in a local reduced out-of-plane stiffness. Through this, the subsequent helical plies experience a high intra-laminar shear stress, which is aggravated by the axial bending stress. Because of the reduced out-of-plane stiffness, locally an increase of radial stress is observed, which has a detrimental effect on the FI of the adjacent helical ply.

To define a laminate several variables, such as helical winding angle and number of hoop plies, should be defined. Therefore it is difficult to make an optimal design, as this would require many function evaluations. However, it can be stated that using the analytical model, a different optimal stacking sequence would be obtained as from FEA. Furthermore, by increasing the friction coefficient, the stress concentration present on the dome-cylinder can be alleviated. Because the hoop plies can be wound further on the dome section, reducing the stiffness difference and increasing the mechanical properties. However, on the dome section the applied load changes from predominantly hoop to axial. Therefore it would not be optimal to position the hoop plies too far on the dome, as this would also significantly increase the weight of the CPV.

Using the highest performing stacking sequence, a baseline design, using the FEA model can be constructed. Here, a friction coefficient of 0.5 is used, through which the hoops can be positioned until $z = 25$ mm on the dome. The baseline design is made using the results from the stacking sequence evaluation in Section 3.3.1, which showed that laminate C had the highest performance in the FEA model. For laminate C the helical plies are positioned on the inside and the hoop plies on the outside. From this, the number of plies are altered, until the FI is as close to 1, resulting in the following stacking sequence:

$$[10, -10]_5 + [90, 90]_7 \quad (3.13)$$

with a total weight of 9.13 kg. Compared to the analytical model, an additional 25% thickness is required to reach a burst pressure of $P = 35$ MPa. Therefore, the analytical model remains rather non-conservative. This result was expected because while the analytical model imposes boundary conditions to mimic discontinuity stresses, it is not able to model the additional axial bending stresses generated by the strain compatibility of the dome and the cylinder. However, as a fast preliminary design it could serve to be useful. As it deviates less from the FEA model, than the netting analysis. Furthermore, the current design freedom is restricted by the relatively thick ply thickness.

A general overview of the CPV behaviour is provided in Section 3.3.3, which shows the highest performing stacking sequence. This part shows that the dome-cylinder interface is the most important part for designing a CPV. The cylindrical section, at a sufficient distance from the interface, has a constant stress distribution. This section is also less prone to failure, as the stresses are lower than at the dome-cylinder section. At the dome-cylinder interface, due to strain compatibility between the dome and cylinder, additional axial stresses are introduced in the laminate. Here, an inward bending moment is created on the dome and a matching outward bending on the cylinder. Lastly, the stresses of the composite on the polar boss are neglected. Because of the intricate interaction between different materials, stress concentrations and thickness build-up. These make it difficult to make an accurate stress representation on this section and it is assumed that the polar boss provides sufficient strength to mitigate failure at this area. Thus, based on the findings from the FEA model, it is optimal to position all the helical plies on the inside and the hoop plies on the outside of the laminate. Through this the axial bending stresses on the dome-cylinder junction can be alleviated effectively. Using this, design the CPV fails on the cylindrical section at a position close to the dome-cylinder interface. At this location is the highest stress-state due to the axial bending stress and hoop stress. On the dome section the hoop stress reduces, which induces a less critical stress-state, because the typical 2:1 hoop-to-axial stress-ratio changes to a more predominant axial stress state. This is beneficial, because it is undesirable to have failure on the dome section. Such a failure could cause boss blow-out. This failure mode results in the metal boss being ejected, which could cause significant damage to the surroundings. This failure mode is mitigated by ensuring that the critical plies are located on the cylinder.

4

Optimisation framework

The increased friction, by using tow-preg, enables greater design freedom in terms of achievable winding angles on the cylinder. Several publications have shown that varying the winding angle through the thickness can improve the performance of a CPV. Here, the baseline design used a constant winding angle through the thickness, which resulted in an unequal strength distribution through the thickness. This can be improved by altering the winding angle through the thickness. Here, a greater friction coefficient yields an increased range of possible winding angles. This was already stated by Tsai et al [49], who noted that a laminate can be optimised by lowering the winding angle of plies that have a remaining strength and vice versa.

However, this design freedom is difficult to assess manually. Therefore a surrogate-assisted optimisation will be performed to reduce the weight of the baseline CPV. However, stochastic optimisation algorithms are computationally demanding. Thus, in this chapter an optimisation framework will be developed, in which the mechanical response of the FEA model is approximated using a metamodel. Here, one surrogate model is used to predict the FI and another model will estimate the total weight of the composite. Using this metamodel a more efficient optimisation can be performed using a GA. Finally, the results obtained from the baseline design are correlated with the optimised design. To observe improvements in the stress-state, which are achieved by using an optimisation algorithm.

4.1. Surrogate modelling

In this thesis the *surrogate modelling toolbox* (SMT) [8] will be used, which is an open-source Python distributed code. This toolbox contains different surrogate models. Various studies [27, 4, 20] have shown that the Kriging surrogate model is a very robust and efficient meta-model. The Kriging surrogate model is constructed by interpolation between the data points. It is important that these points are evenly spread over the design space to describe the model behaviour and mitigate an ill-conditioned Kriging prediction matrix. Therefore for the DOE Latin Hyper Cube sampling (LHS) is used to create a quasi-random sample set [8]. However, for a surrogate model it is difficult to estimate how many sample points are required to have a accurate surrogate model. Nik et al [4] and Jin et al [20] used $10n$ sample points, where n is the dimension of the problem. However, this ratio can not be applied to different problems. The sample points are constrained by the boundaries of the design variables.

In the preliminary analysis 10 design variables are used to observe the response of the CPV. Here, 5 sub-laminates of helical plies, similar as the baseline, are evaluated for the effect of the winding angle and 5 sub-laminates of hoops are reviewed for various thicknesses. The bounds of the design variables are defined as follows:

$$[1, 45], [0, 10], [1, 48], [0, 10], [1, 52], [0, 10], [1, 55], [0, 10], [5, 58], [0, 10] \quad (4.1)$$

where, the first set is the upper and lower bound of the helical ply and the second set the number of hoop plies in the sub-laminate etc. The bounds for the helical plies are computed by reviewing the minimum and maximum achievable winding angle for a 0.5 friction coefficient in TW. Following this, the following variables, [25, 3, 5, 0, 22, 4, 54, 0, 6, 9] will create the following laminate:

$$\begin{aligned}
& [25, -25] + [90, 90]_3 + [5, -5] + [90, 90]_0 + [22, -22] + \\
& [90, 90]_4 + [54, -54] + [90, 90]_0 + [6, -6] + [90, 90]_9
\end{aligned} \tag{4.2}$$

The data points are reviewed using a new set of 50 validation points. These points are created to mitigate any bias in the prediction. To assess the error of the surrogate model, the root mean square (RMS) is used, as defined in Section 2.8. The smaller the error, the higher the accuracy of the prediction. The results are plotted using the FI_{true} and \hat{FI} , where the latter is the predicted value by the surrogate model. The RMS error is $RMS = 0.157$ and $RMS = 0.002$ for the FI and weight surrogate model, respectively. Thus, a very high predictive quality is obtained for the weight surrogate model. And a large predictive error is obtained for the FI. The results are plotted in Figure 4.1. The blue line illustrates a 1:1 relation between the predicted and true value, which would result in a zero error. The red dots illustrate the predicted values, using the surrogate model. Some initial observations are made from the initial data set, which can be summarised as:

- Inner hoop plies fail on the dome-cylinder interface due to axial tensile stresses induced by bending stresses
- Using a high number of inner hoop plies result in high inter-laminar shear stresses, mainly τ_{13} , which cause failure in the helical plies subsequent to hoop plies.
- Optimal stacking sequences are obtained by either an increasing, decreasing or constant helical winding angles

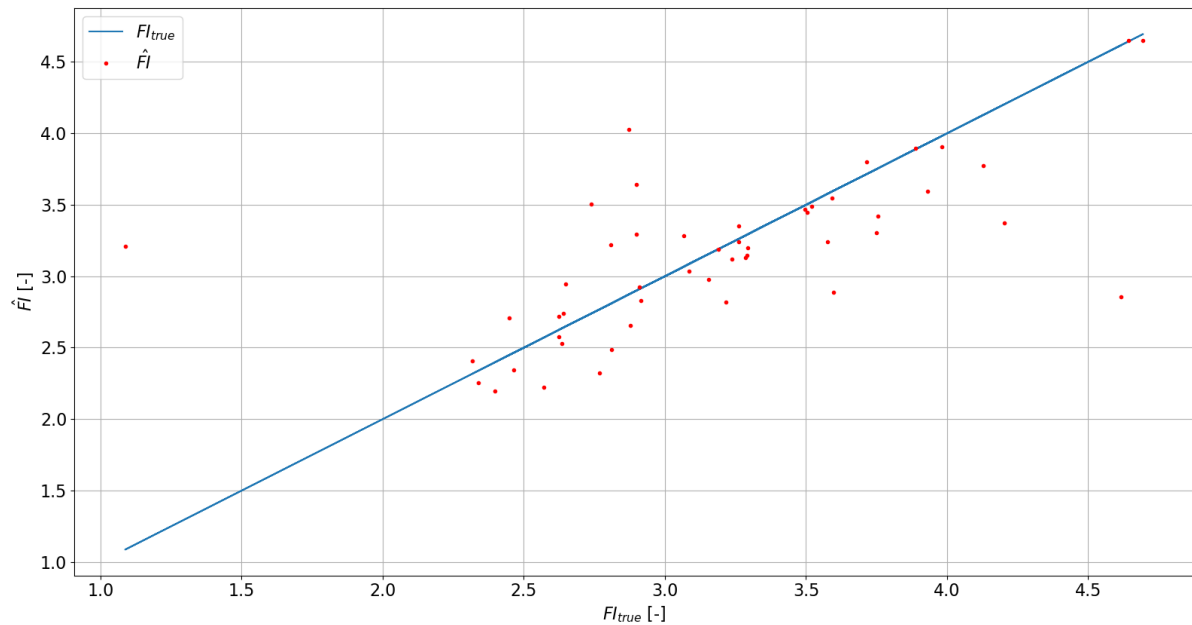


Figure 4.1: The true value plotted versus the predicted value

Furthermore, using the same dataset, two different surrogate models are created. The first surrogate model is trained using the LHS sample points and the FI. Here, the samples which have failed on the dome section are discarded, because this results in a very poor predictive quality of the FI surrogate model. This is induced by the generation of inter-laminar stresses above resin elements and the low axial stiffness of the hoop plies at the inner layers. However, failure on the dome could be predicted by training a surrogate model with designs which fail on the dome section. Similarly, two surrogate models can be trained by evaluating the maximum FI on the dome and cylindrical section, using the same sample set. Secondly, a surrogate model is trained using the LHS sample points and the calculated weight. Together these surrogate models can be used to assess if a stacking sequence results in failure and what the total composite weight is. Using the previously stated observations, the number of design

variables and bounds of the design variables are reduced to improve the predicative quality of the surrogate model. The new bounds are defined as follows:

$$[1, 45], [5, 58], [0, 2], [0, 2], [0, 2], [0, 7] \quad (4.3)$$

where the first two variables are the inner and outer helical ply angle and the other design variables are the number of hoop plies. Here, the helical winding angle is linearly varied between the inner and outer ply, to reduce the number of design variables. This allows the model to either increase, decrease or have a constant winding angle through the thickness. The outer hoops are constrained to have a maximum of 7 sub-laminates, because otherwise the optimised design would have a higher weight than the baseline design, which is constructed in Section 3.3.2. Using the following variables, [2, 10, 1, 2, 1, 5] would results in the equivalent laminate:

$$[2, -2] + [4, -4] + [90, 90] + [6, -6] + [90, 90]_2 + [8, -8] + [90, 90]_1 + [10, -10] + [90, 90]_5 \quad (4.4)$$

An initial data set of 1500 samples is created using LHS and plotted for three design variables in Figure 4.2. Also, an additional 200 data points are created to validate the accuracy of the FI and weight surrogate model, which are shown in Figure 4.3 and Figure 4.4, respectively. For the model the RMS error for the FI surrogate model and the weight surrogate model are $RMS_{FI} = 0.098$ and $RMS_{weight} = 0.0002$, respectively. Thus, a very high predictive quality is obtained for the weight surrogate model, while the FI surrogate model has a lower accuracy.

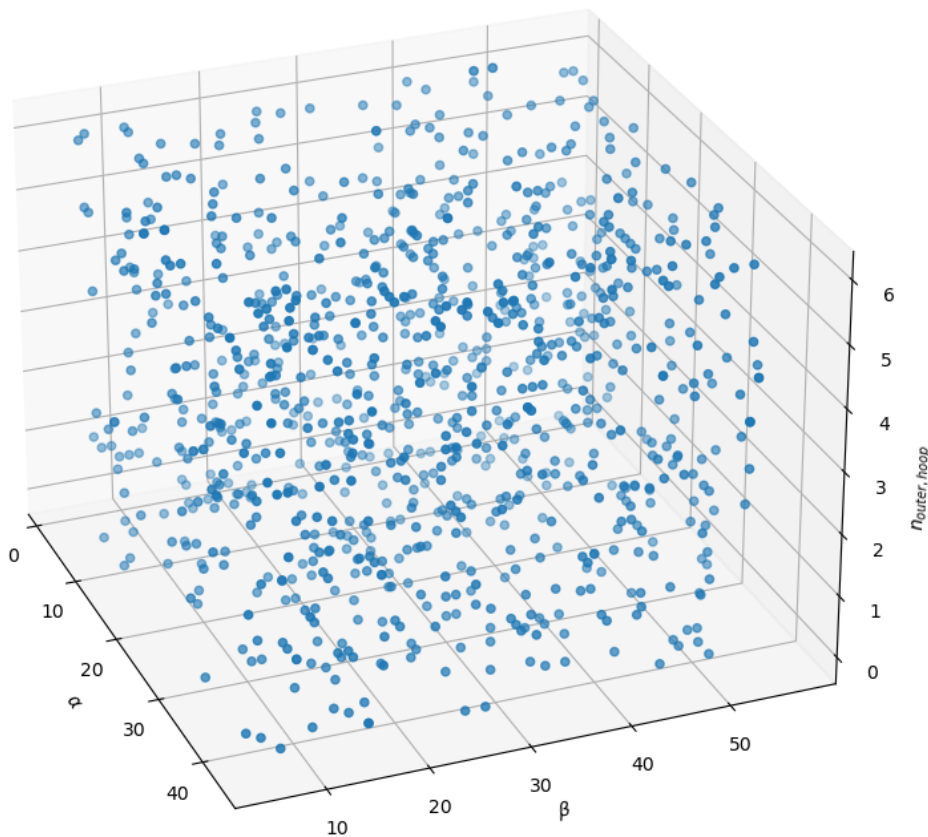


Figure 4.2: The samples plotted in a 3D space for the inner helical winding angle, outer helical winding angle and the number of outer hoop plies

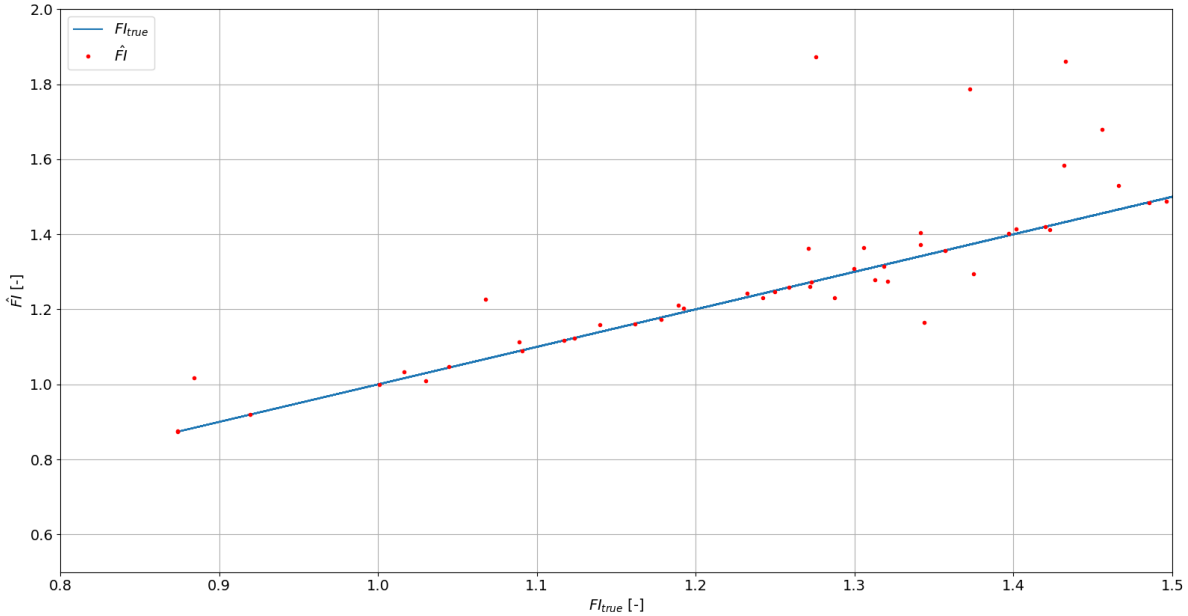


Figure 4.3: Predicted vs true FI, using 200 validation points for the FI surrogate model

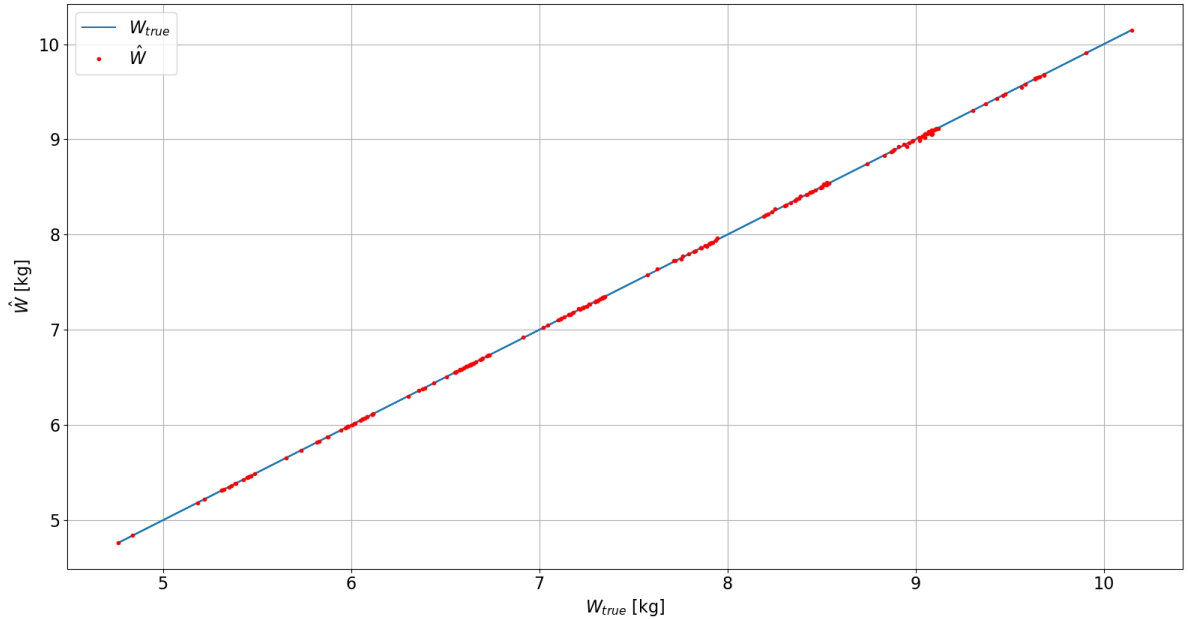


Figure 4.4: Predicted vs true weight, using 200 validation points for the weight surrogate model

In Figure 4.5 the prediction quality is plotted for the inner and outer helical winding angle on a logarithmic scale. Lower values indicate a higher precision of the predictive quality of the FI surrogate model. The several purple dots indicate locations at which has been sampled using the DOE and results in an exact prediction of the surrogate model. The predictive quality of the FI surrogate model is lower because the position of failure on the cylindrical section may vary, which makes it more difficult to predict the FI. The response surface shows more valleys and peaks, while a more even response surface is present for the weight surrogate model.

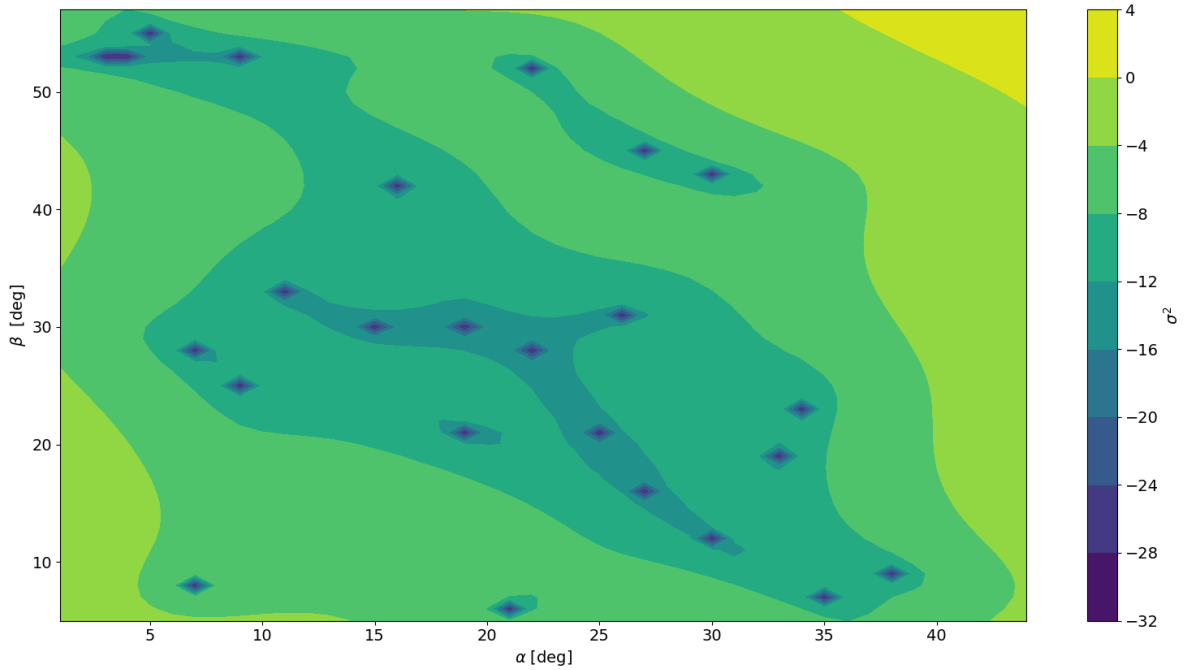


Figure 4.5: Variance of the FI surrogate model for the inner helical winding angle α and outer angle β

4.2. Stacking sequence optimisation of a thick-walled CPV

In this thesis surrogate-assisted optimisation will be used to find a solution which minimises the weight of the CPV. This results that a single function evaluation, or the fitness of an individual can be computed quickly. The objective function is defined as follows:

$$f = \frac{W_{lam}}{W_{baseline}} \quad (4.5)$$

where W_{lam} is the total weight of the composite material of the optimised design and $W_{baseline}$ is the total weight of the composite of the baseline design, computed in Chapter 3. Because the goal is to minimise the weight, but maximise the load-bearing capability, an augmented fitness functions is introduced. Using this type of functions, constraints can be imposed [10]. The augmented fitness function is defined as:

$$\phi = \begin{cases} f + \epsilon FI & \text{if } FI < 1 \\ f + \beta FI & \text{if } FI \geq 1 \end{cases} \quad (4.6)$$

where FI is the failure index, ϵ is the bonus term and β is the penalty term. These terms can be varied to further optimise the design and obtain a unique solution. If a design has a FI above 1, it should be discarded, as it is not a valid design. Furthermore, by varying ϵ , the design can be pushed to a weight dominated result or a more FI dictated design. However, as observed in Section 4.1, the surrogate model for the FI had a lower predictive assessment than the weight. Here, an average deviation of less than 1% is observed for the predicted FI.

The *GeneticAlgorithm2*¹ is a Python module and is used to find a global minimum solution in the defined design space. This algorithm uses a stochastic method to search the entire design space. The randomness is provided by crossover and mutation of an individual. Through this, the entire design space is analysed, without being trapped in a local minimum. The algorithm is able to use both continuous or integer optimisation. In this case, integer optimisation is used to reduce computational effort. The algorithm stops after convergence of the fitness function is not improved for 15 generations.

For the GA several options can be altered to enhance the search for the global minimum. A convergence study has been performed, reviewing the effect of changing each parameter, defined in

¹<https://github.com/PasaOpasen/geneticalgorithm2>

Table 4.1. Only the population size is required to be altered, from the default settings, increasing the size to 500. This ensures that sufficient individuals are spread over the entire search domain and finding a global minimum. The optimisation is arrested once the objective function has not been improved for 15 generations.

Table 4.1: Parameters used in the GA

Parameter	Value
max. iterations	250
Populations size	500
Mutation probability	0.1
Elite ratio	0.05
Crossover probability	0.5
Parents portion	0.3

4.3. Results and discussion

Using the surrogate model, a very efficient optimisation can be performed. A single function evaluation only requires estimated 0.001 seconds, compared to 30 seconds for the actual model. Therefore, a large population can be used to search the design space in the GA. The found optimal solution, conducted using the surrogate-assisted optimisation is:

$$[14, 6, 0, 1, 1, 3] \quad (4.7)$$

which results in the following laminate:

$$[14.0, -14.0] + [12.0, -12.0] + [10.0, -10.0] + [90, 90] + [8.0, -8.0] + [90, 90] + [6.0, -6.0] + [90, 90]_3 \quad (4.8)$$

where $\beta = 100$ and $\epsilon = 0.2$. Here, β is chosen such that any laminate having a FI above 1 is discarded. It can be seen that the helical winding angle decreases through the thickness and that there are no inner hoop plies. To increase the bending stiffness it was expected that helical plies should have a low winding angle and positioned on the inner and outer side of the laminate. However, on the inside of the laminate the hoop stress is higher than on the outside. This stress can be alleviated by a higher winding angle. But on the inside, the helical ply should also be designed for the axial bending stresses. On the outside of the laminate the helical plies have decreased. Here, the hoop stress is lower, because the hoop stress decreases in a thick-walled CPV. Furthermore, higher winding angles have a higher effective width on the dome section. This results in requiring less loops to achieve a coverage of 200%. Therefore, lower helical winding angles, result in a higher total weight. This might be counter-intuitive, because a lower winding angle has a shorter winding path on the dome than higher winding angle. Further observation show that the hoop plies are more equally distributed through the thickness. Through this the hoop strain is minimised more effectively, as opposed to only positioning hoop plies on the outside of the laminate, which was the strategy for the baseline design.

The results for the optimised design, comparing the results from the surrogate, FEA and baseline design are depicted in Table 4.2. The first row shows the design the GA has found using the surrogate model. Next, the second row shows the same design, but verified with FEA. Furthermore, the results found in Section 3.3.2 are shown in the third row and compared with the optimised design in the last row. The results show that the total weight of the composite can be reduced by 13%, compared to the baseline design, using a surrogate-assisted optimisation. This is a result of varying the helical winding angle and positioning the hoop plies more effectively. Through this only 5 sub-laminates of hoop plies are required, while the baseline has 7 sub-laminates of hoop plies. Also, the helical winding angle is varied to get a more evenly distributed FI through the thickness. This should result in that the load-bearing capability after FPF is low. Because after this first ply fails, the load redistributes over the remaining intact plies. However, these plies do not have any remaining strength. Which should result in fast final failure after FPF.

In Section 3.1.4, a 2:1 ratio of hoop to helical plies was found by the traditional netting analysis, resulting from the same ratio for the hoop to helical stress. However, the optimisation shows that the induced discontinuity stresses, generated by the strain compatibility between the dome and cylinder, result in a 1:1 ratio for hoop to helical ply. This is because the helical plies have a higher stiffness in the axial direction to mitigate the bending stresses. Also, the angle of the helical plies is increased, through which a higher stiffness in the hoop direction is achieved. Lastly, the hoop plies are positioned and grouped together to reduce inter-laminar stresses and reduce the hoop strain on the cylindrical section.

Finally, as previously stated in the report, the goal is to redistribute the load more evenly over all the plies. It was shown in Section 3.3.2 that the FI of the hoop plies was much higher than the helical plies. Indicating that the plies are not loaded evenly. In Figure 4.6 the distribution of the Tsai-Wu FI is shown for the optimised design. Here, all plies have a similar maximum FI near the dome-cylinder interface. This also indicates that complete failure should occur close to FPF. Also, the highest FI occurs in a hoop ply, which yields a more predictable failure [31]. Furthermore, FPF occurs at $z = -50$ mm. This is at the dome-cylinder interface on the cylindrical section, which is desired. A failure on the dome section could cause flying parts [55].

Table 4.2: Difference in optimal results between the surrogate model and the FEA model

	FI	W	Difference (W)
	-	kg	%
Surrogate	0.96	7.94	} -13.1
FEA	0.98	7.94	
Baseline	0.95	9.13	

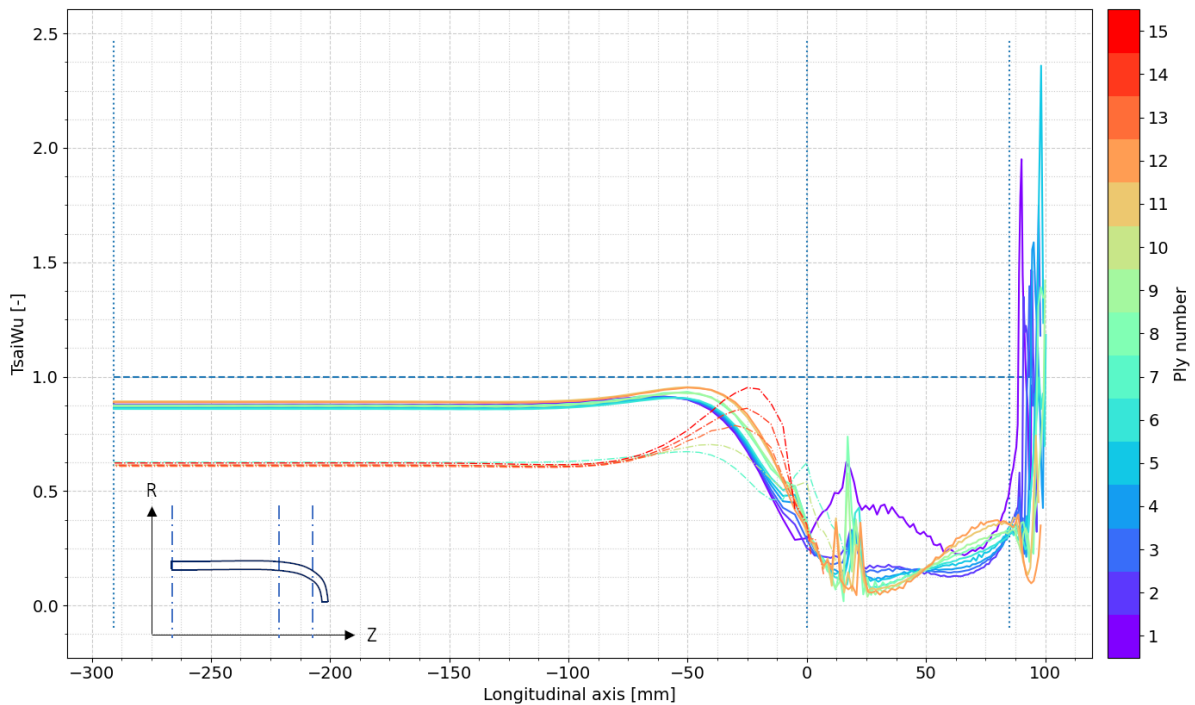


Figure 4.6: A more evenly distributed FI through the thickness for the optimised design

Furthermore, for the optimised design the burst type is evaluated, as defined by Leh et al [27]. Here, it is desirable to have the maximum fibre stress on the cylindrical section. This is evaluated as follows:

$$b_{type} = \frac{\sigma_{1,dome}}{\sigma_{1,cylinder}} \quad (4.9)$$

This value should be below 1 to have a safe failure type, i.e. on the cylindrical section. This is the case for the obtained optimised design, for which $b_{type} = 0.74$.

5

Experimental evaluation

The evaluated tools in the previous chapters are all based on numerous assumptions. Therefore it is necessary to perform experimental tests to observe discrepancies in the developed numerical models. This chapter will first provide an overview of the utilised apparatus, which will be used for the experimental evaluation. Following this, the friction coefficient, of the used tow-preg material, will be determined using an friction experiment. In Appendix C some statements are provided about the initial production trials, supported by some illustrations taken during the production.

5.1. Experimental set-up

The production of the CPV is performed at the samXL facility. This facility contains a variety of robots, aimed at various applications. The CPV will be produced using the *KUKA KR-210* and an AFP robot head, as shown in Figure 5.1. The robot head is capable of placing the tape directly on the mould and compressing it with the roller or placing the tape on the mandrel using FW. The latter will be applicable for this thesis. The tape will be wound using the in-house developed software TW. From the optimised design computed in Section 4.3, a .tpa file will be written. This file is a TW project file, which can be used to generate the robot movements for every ply.

Prior to winding, it is important to have the correct coordinate systems for the robot and the winding tip. This can be reviewed and calibrated in the *Kuka.WorkVisual* environment. The provided tow-preg is delivered on 2 kg bobbins. These need to be re-spoiled on a Hafner spool, which can be fitted on the tool head (position 1 in Figure 5.1). From the initial position, the tape is brought through two rollers. Before this the backing tape can be removed. However, the current material does not contain any backing material, according to the supplier this should enable higher winding speeds. But during production it has been observed that without any backing tape the fibres from the adjacent layers are pulled off. Thus, for the current application backing tape would mitigate any fibre pull-off during production. From this the tape is pinched between two rollers to secure and flatten it (2). After this the tape passes a cutter, which will not be used during FW (3). Lastly, the tape is fed through the chute (4) and tensioned by the compression roller (5). This is achieved by correctly positioning the robot head and attaching the tow-preg tape to the mould. For AFP the compaction roller would be used to press the material directly on the mould to push out any voids. Because of the tackiness of the tape it is not required to fix the tow-preg with any additional tape, as it already provides sufficient adherence to the mould. The robot motion, applicable to a winding path, can be evaluated either in TW or in real-life. Here, it is important to mitigate collision with the robot head and the mandrel or fixture. The mandrel is fitted in the fixture by connecting it with an extension rods, as shown in Figure 5.2. This ensures that the robot head has sufficient movement freedom. In the chuck (right-side Figure 5.2) the extension rod is fixed and rotates. On the left-side it is fitted in a male cone shape, which makes it possible to rotate.

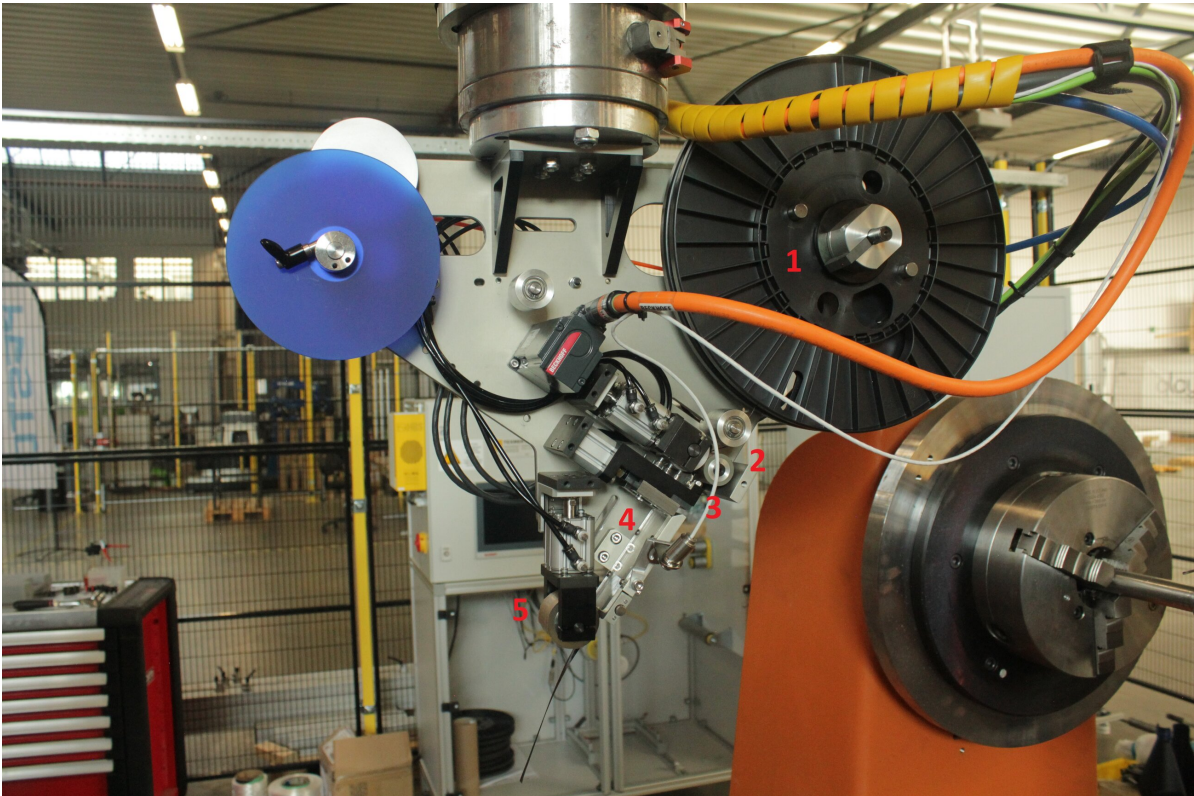


Figure 5.1: The AFP robot head located at the samXL facility



Figure 5.2: Mandrel fitted in the fixture at the samXL facility

5.2. Friction experiment of tow-preg tape

It has been observed in Section 3.3.1, that by increasing the friction coefficient, the discontinuity stresses at the dome-cylinder can be reduced. The effect of the friction coefficient is mainly present on the dome section, where it determines the possible helical winding angles. However, the friction coefficient also determines the axial position until which hoops can be wound. Various publications have reported similar friction coefficients for tape winding [51, 24, 53], namely 0.5. However, the exact determination of the friction coefficient may be tedious. Koussios et al [24] developed a special mandrel shape in which the axial coordinate, translates into a friction coefficient. The convex shape ensures that the magnitude of friction is linearly proportional to the axial coordinate. Through this, the determination of the friction coefficient is made more easily and only requires simple machine control. Initially the cone has a flat plateau, in which the tape can be secured to the mould. The friction can be determined using the following equation:

$$\lambda = c_0 + c_1 z \quad (5.1)$$

where c_0 and c_1 are unknown coefficients. These are determined by the axial coordinates of the cone. Here, z can vary from $z = [0, z_r]$, where z_r is the axial length of the cone, where $\lambda = 1$. Furthermore, at $z = 0$ the friction coefficient is $\lambda = 0$. This results in $c_0 = 0$ and $c_1 = \frac{1}{z_r} = \frac{1}{235}$.

Several factors influence the friction coefficient. The deposition rate and tape tension have a negligible effect [53]. However, the viscosity of the materials plays an important role [53]. A higher viscosity results in a more honey like substance, which results in a better bond to the substrate. Here, wet-winding has a viscosity in the range of 10^{-1} Pa·s, while pre-preg has a viscosity around 10^1 Pa·s. The viscosity can be further increased for thermoset resins by adding additional heat, by a heat torch or laser. A downside of the higher tackiness of the tow-preg is that it might stick to the rollers of the AFP head. Therefore teflon tape is used at positions where the tape might stick to the robot. The results of the experiment are presented in Table 5.1.

During the first test, some wrinkles were present in the tape. This probably occurred during the re-spooling of the tape to the Hafner-spool, due to the low in-plane stiffness of the uncured tape, making it prone to buckle. The second attempt showed less material deficiencies. However, at high axial coordinates the difference in radial position between the outer side and inner side of the tape differs, which results in the outer side of the tape floating slightly above the mandrel. Also, cavities are observed at some locations. This occurred due to slight ply realignment or wrinkled tape. Furthermore, the obtained results show an even higher friction coefficient than the expected 0.5. It should be noted that the reported values are the friction coefficient at which complete release of the tape commenced, while prior tape realignment took place. However, at these values, the tape shows quite significant material deformations, such as, folding, wrinkling and in-plane deformation. Therefore it is advisable to use a reduced friction coefficient for actual production. Lastly, the denoted data in Table 5.1 has only been performed for two tests. But to exactly predict the friction coefficient more tests should be conducted. Also, the test has not been conducted with the tape as substrate, because it is expected that the aluminium mould gives the most conservative results, as has been observed by Koussios [24]. Furthermore, the current test has been performed on a specialised mould, designed to compute the friction coefficient. The actual friction coefficient on the CPV might also be different due to a different substrate material. Which why it would be advisable to reduce the maximum friction coefficient during the actual production of the CPV.

Table 5.1: Experimental results of the friction experiment

Attempt			
1		2	
z [mm]	λ	z [mm]	λ
166.11	0.71	186.97	0.80



Figure 5.3: Moment of full fibre slippage, at $z = 186.97 \text{ mm}$

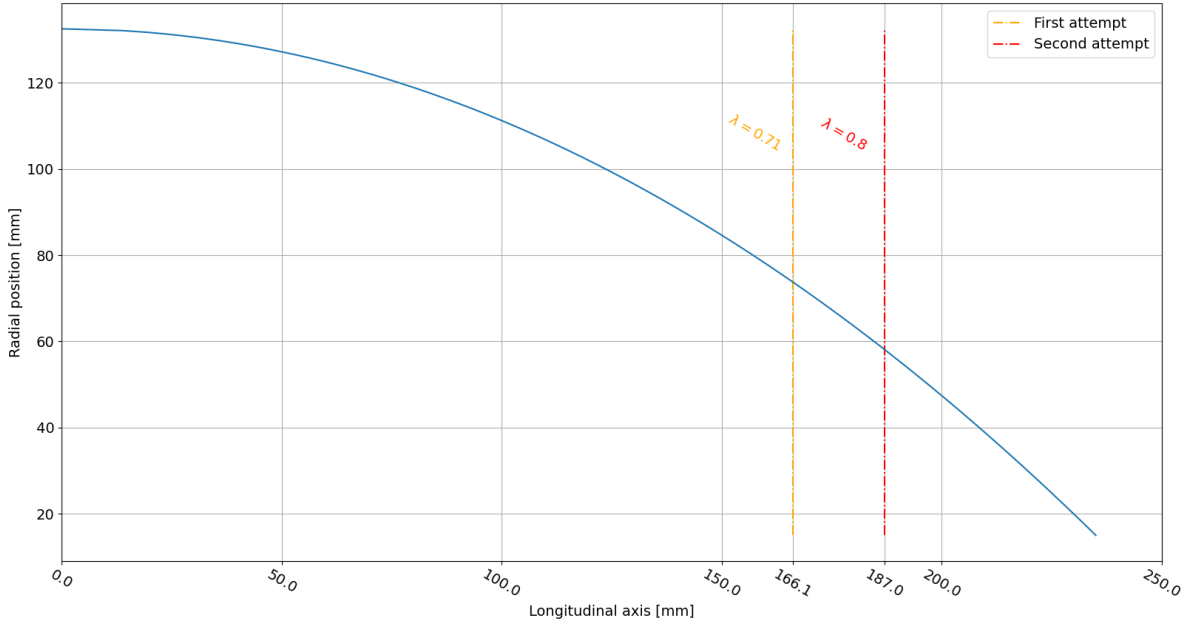


Figure 5.4: Locations of tow-preg slippage depicted on a 2D cross-section of the mandrel

6

Conclusion

Tow-preg material offers the potential to reduce the material usage of carbon fibres in the design of hyperbaric type IV CPVs. Currently, most CPVs are produced using wet-winding, in which prior to placement on the mould, the fibres are wetted in a resin bath. As a consequence, this process yields inconsistent material properties and a low friction coefficient, the latter which is required to use winding paths which deviate from geodesic winding. Alternatively, a new framework is developed, in which the preliminary design was constructed using an analytical model. This model calculates the stresses across the thickness of a thick-walled CPV, including an isotropic liner and boundary conditions. Consecutively, a FEA model is constructed which simulates a variety of characteristics present during the manufacturing and design of CPVs, such as thickness build-up on the domes, non-geodesic winding paths and void creation. The FEA model can be used to readjust the number of plies to attain a predefined burst pressure. In the following paragraph the research questions are answered as stated in Section 1.3.

A certifiable type IV CPV should be designed by using a combination of numerical models and experimental tests. This thesis focused solely on burst pressure analysis, although there are several other analyses required to fully certify a CPV. The burst pressure is defined by the nominal working pressure times a safety factor, usually 2.25. However, due to constraints in the current research it was not possible to design the CPV for higher pressures than $P = 35$ MPa. An analytical model does not provide sufficient accuracy to describe the discontinuity stresses present at the dome-cylinder interface, and may thus only be used for a preliminary analysis. Furthermore, to describe the mechanical response of a CPV, several design characteristics should be included in the numerical model. These features aim to improve the correlation with the experimental burst pressure test. The minimisation of used material can be achieved by using a surrogate-assisted optimisation framework. This methodology aims to achieve an optimal load redistribution, in which each ply has a low remaining strength. As an additional benefit, the minimisation also reduces the cost of the CPV, given material cost is the main contributor to the price of a CPV.

During FW the friction coefficient is not influenced by process parameters such as the fibre tension and winding. However, the tackiness, or viscosity of the used material significantly alter the friction coefficient. In this research, it was shown that the currently used tow-preg material had a very high friction coefficient, compared to reported values from existing literature. Using such excessive friction could result in material deformations such as wrinkling. On top of that, the current tow-preg was relatively thick. Several publications have reported single ply thicknesses between 0.1 and 0.2 mm. This reduces the design freedom of the stacking sequence, given less plies were required to be stacked to achieve a defined burst pressure. Furthermore, the thickness build-up on the dome was heightened due to the higher single ply thickness.

The analytical model developed, provided quick insight into the effect of stacking and grouping different plies. It was shown that, at a sufficient distance from the dome-cylinder interface, stresses can be computed using the analytical model. However, the lack of modelling the dome-cylinder interface, yields a discrepancy in the prediction of the required number of plies. It has been observed that

additional axial bending stresses are generated at the dome-cylinder interface as a result of strain compatibility. Thus, the analytical model underestimated the maximum stresses as well as resulted in a different optimum stacking sequence. The analytical model predicted a 67% higher required thickness versus the netting analysis. However, verifying the preliminary design with the FEA model showed that the thickness should be further increased with 25%. This showed that the analytical model can be used to make a rough estimation of the required number of plies to attain a certain burst pressure. However, it is not able to define an optimal stacking sequence to improve load distribution, and should always be verified with a numerical model. Also, it underestimated the maximum stresses present in a CPV, which resulted in a different optimal stacking sequence and reduced the required thickness to attain a certain burst pressure.

An element performance review showed that axisymmetric elements were highly accurate, while reducing the computational cost of the FEA model. The results of the current model can be obtained within several seconds, due to minimisation of the problem definition using axisymmetric elements. However, the numerous possibilities for the stacking or grouping of plies and variation of the helical winding angle, makes it difficult to manually define an optimal stacking sequence. Therefore, a surrogate-assisted optimisation framework was created. This framework creates a sample set using LHS to evenly distribute data points across the design space. From this, two surrogate models were trained to mimic the behaviour of the FEA model and to estimate the FI and weight of the CPV, from a set of design variables. However, compared to the FEA model, a surrogate model is not able to exactly predict the FI and weight. An average of 1% deviation was observed for the prediction of the FI, whilst an almost exact value was obtained for the composite weight. In conclusion, it is important to have sufficient sample points to train the model depending on the variance of the predicted value.

To minimise the weight of the CPV, a GA was used. A heuristic is employed to explore the design space and minimise the objective function. The objective function was defined as the quotient of the computed composite weight and composite weight from the baseline design. An augmented fitness function was used to achieve an optimal result.

The results from the optimisation showed that the total composite weight was reduced by 13% and a more evenly distributed FI was obtained. The helical winding angle showed a decreasing winding angle for an increasing radial position. This was a result of the induced bending stress at the dome-cylinder interface, where lower helical angles, far from the mid-plane, increase the bending stiffness of the laminate. Furthermore, the hoop plies were evenly distributed through the thickness of the laminate. Moreover, no hoop plies were present in the inner plies, because these would be stressed on the matrix due to the axial bending stress. However, the hoop plies were required to minimise the predominant hoop strain on the cylindrical section. Finally, FPF occurred in the outer hoop ply, where the bending stress has the largest magnitude and the radial stress decreases. The radial stress alleviated the in-plane Poisson deformation caused by the bi-axial tensile stress-state, yielding a beneficial effect for the inner plies.

An internally pressurised CPV causes a three-dimensional stress state in the laminate. On the cylindrical section, the hoop stress has the highest magnitude and the radial stress has a negative value. For a thick-walled CPV, the stresses diminish through the wall thickness. The most significant stress was present at the inner side of the laminate. To effectively alleviate the prevailing hoop strain, hoop plies should be positioned at the inner side of the laminate, because hoop plies have the highest stiffness in the circumferential direction. The internal pressure causes the cylindrical section to expand radially, which in turn results in a tangential strain. Thus, the hoop plies also have a higher stiffness in the radial stress component. Furthermore, for the axial stress component on the cylindrical section, low angle helical plies should be used. A lower angle results in a higher stiffness in the loading direction of the axial stress. Thus, for the cylindrical section the predominant hoop and radial stress can best be alleviated by positioning and grouping hoop plies on the inner side of the laminate. To increase the axial stiffness low angle helical plies should be used. From the stacking sequence evaluation it was observed that the hoop and helical plies should be alternated to minimise the FI.

Furthermore, it has been shown that the most predominant stress state was at the dome-cylinder interface. This was induced by the strain compatibility between the dome and cylinder, which induced axial bending stresses. Also, the varying stiffness due to hoop plies, double-curved shape profile of the dome and non-geodesic winding angle, caused an intricate stress-state. This showed that the stacking sequence of a CPV should be designed using the stress-state at the dome-cylinder junction.

The bending stress can best be alleviated by increasing the bending stiffness of the laminate. This was achieved by positioning fibres on the outside of the laminate to increase the bending stiffness and in the direction of the stress component. Helical plies have the highest axial stiffness and should be positioned on the inner and outer side of the laminate. Through this, the bending stiffness, or D matrix can be increased effectively. Due to the axial bending stresses, the hoop plies should not be positioned on the inner side, but rather on the mid-plane of the laminate. Hoop plies fail prematurely because these are loaded transversely. To mitigate excessive inter-laminar stresses, hoop plies should be spaced at different radial positions of the laminate, separated by helical plies. This results in the drop-off regions being distributed along the axial coordinate. The inner side of the laminate has the most predominant stress state. Therefore the helical winding angle should show a decreasing pattern. Through this a high bending stiffness is achieved, while also having more stiffness in the tangential direction.

In conclusion, the baseline framework was used to construct a representative CPV design and taken as a baseline to compare against the optimised design. The analytical method required a 67% higher laminate thickness than the netting analysis, to attain a burst pressure of $P = 35$ MPa. This can be attributed to the simplified analysis performed by the netting analysis, which neglects the matrix stiffness and only considers in-plane forces. A similar analysis was performed using the FEA model. An additional 25% laminate thickness was required to achieve the desired burst pressure in the FEA model, because the analytical model does not consider the discontinuity stresses present at the dome-cylinder interface. This resulted in a total composite weight of $W = 9.13$ kg. Furthermore, due to the stress-state at the dome-cylinder interface in the FEA model, it was more optimal to position all helical plies on the inside and all hoop plies on the outside. Using the analytical model, an interchanging positioning and grouping of helical and hoop plies was found to be the highest performing stacking sequence. This difference was mainly attributed due to the axial bending stresses generated at the dome-cylinder interface. Following this, an optimisation framework was created, which resulted in a 13.1% composite weight reduction. This was achieved by optimally positioning the hoop plies at different radial positions and altering the helical winding angle to increase the bending stiffness, to effectively alleviate the induced discontinuity stresses. The optimisation methodology showed the potential to reduce the material usage in a thick-walled CPV. Lastly, the friction coefficient of the tow-preg was found to be $\lambda = 0.8$. The high tackiness of the tape introduces several difficulties for the manufacturing process. This can be mitigated by designing the production process for this material, without the need to re-spool the material.

7

Recommendations

This thesis has majorly focused on the development of a framework to simulate the mechanical behaviour of CPVs. Several phenomena which occur during the production of CPVs were included in the models to better predict onset of failure. However, most of these characteristics were based on experimental evaluation described in publications. Thus, to better describe the mechanical behaviour more CPVs should be manufactured and tested. This should enable better description of the size of resin pockets, ply realignment for non-geodesic winding paths and thickness distribution on the dome. During the production the creation of resin pockets should be monitored. Also, the influence of thickness distribution on the dome should be reviewed for non-geodesic winding angles. Here, it is expected that higher winding angles exert a higher compressive force on the underlying plies. Lastly, the effect positioning and grouping of helical and hoop plies have on the underlying plies should be analysed to observe variation of fibre volume fraction and porosity. The previously stated comments can be used to improve the predictive quality of the FEA model.

Currently, only a simple burst pressure test has been planned, to assess the correlation of the numerical models with the experimental test. However, this will only result in knowing at which pressure the structure has failed in the test. But, if the CPV fails at a lower pressure, the cause of failure can not be tracked. Therefore, future test should also include the results of the variation of the in-plane strain components and out-of-plane displacement. These can be correlated to the numerical model at several pressure stages to observe where possible discrepancies occur in the numerical model. Also, these results can be used to select an appropriate failure criteria and to observe if progressive failure analysis is required. Following this, one example of such a measurement, is digital image correlation. This test sprays a speckled pattern upon the structure and tracks the change of the speckles, which relate to a strain component or out-of-plane displacement.

There still remains significant doubt in the analytical thickness descriptions on the dome. While this section is prone to many material inhomogeneities, possibly resulting in premature failure. Therefore, for subsequent projects the thickness variation, as result of a non-geodesic winding pattern should be better described by either a numerical or analytical model. Such a model should include the effect of the local effective tape width, local winding angle and required number of loops to get a full coverage. The difficulty in this model will be in describing the thickness near the polar boss, where the winding angle approaches 90 degrees and resin-rich areas might be present.

The optimisation framework was built using a surrogate model and a GA. Through this, the optimisation could be performed more efficiently. Also, the parameters and the correct objective function could be defined and reiterated, to obtain an optimum design. However, there still remains a prediction error for the FI surrogate model, which is stacked upon the other errors originating from the numerical models. Therefore in future optimisation runs, the prediction error from the surrogate model should be reduced. This can be attempted by creating a better DOE. Which can be achieved by either generating more samples or reducing the bounds of the design variables, based on the current optimal results.

From the optimisation a more evenly distributed FI was obtained for all plies, where most plies are close to failure. This would indicate that after FPF, the remaining strength would be low and final

failure would occur close to FPF. However, the current design has a relative low internal pressure and small laminate thickness, which may not yield big differences between FPF and LPF. But for a increasing laminate thickness and a higher internal pressure it might be more difficult to achieve a uniform strength through the thickness. Therefore, to better predict final failure and possibly reduce composite weight, a progressive failure analysis should be performed. These analyses usually require difficult Fortran programming in Abaqus and also significantly increase the simulation time. However, there exist packages which include very intricate damage progression models, based on Puck's failure criteria, which could be implemented for Abaqus. Here, Nebe et al [35] used *CompDam*¹ to predict the damage progression of a hyperbaric thick-walled pressure vessel. The experimental test only showed a 2% difference in predicted burst pressure without considering damage and a mere 0.2% difference in predicted burst pressure by considering a progressive damage model. Using such a progressive failure analysis could reduce the weight, because the actual strength of the CPV might be higher than predicted by using FPF.

During the production trials it has been observed that the AFP robot head can not be used to manufacture the CPV, with the current tow-preg material. This is because it is required to re-spool the tow-preg material from the bobbin on a hafner spool. During this process folds are created in the spool. Furthermore, during the re-spooling the tow-preg is stacked. This causes problems during the production, as a layer may pull off fibres from an adjacent ply during production. On the bobbin this is mitigated by positioning the material at an angle, such that the fibre does not get pulled off during the production. It is suggested to use a tensioner system, in which the production is performed directly from the bobbin. Such a system consist of several spools to guide the tow-preg tape to the correct position. The advantage of this production method is that it is not necessary anymore to re-spool the material and higher winding speeds can be achieved.

¹https://github.com/nasa/CompDam_DGD

References

- [1] A. Kaddour and M. Hinton. "Maturity of 3D Failure Criteria for Fibre-Reinforced Composites: Comparison between Theories and Experiments: Part B of WWFE-II". In: *Journal of Composite Materials* 47.6-7 (Mar. 2013), pp. 925–966. ISSN: 0021-9983, 1530-793X. DOI: 10.1177/0021998313478710. URL: <http://journals.sagepub.com/doi/10.1177/0021998313478710> (visited on 05/07/2021).
- [2] *Abaqus/CAE User's Manual*. 2011.
- [3] V. Alcántar et al. "Optimization of Type III Pressure Vessels Using Genetic Algorithm and Simulated Annealing". In: *International Journal of Hydrogen Energy* 42.31 (Aug. 2017), pp. 20125–20132. ISSN: 03603199. DOI: 10.1016/j.ijhydene.2017.06.146. URL: <https://linkinghub.elsevier.com/retrieve/pii/S0360319917325016> (visited on 08/18/2021).
- [4] Mahdi Arian Nik et al. "A Comparative Study of Metamodeling Methods for the Design Optimization of Variable Stiffness Composites". In: *Composite Structures* 107 (Jan. 2014), pp. 494–501. ISSN: 02638223. DOI: 10.1016/j.compstruct.2013.08.023. URL: <https://linkinghub.elsevier.com/retrieve/pii/S0263822313004200> (visited on 06/14/2021).
- [5] Pavo Baličević, Dražan Kozak, and Tomislav Mrčela. "Strength of Pressure Vessels with Ellipsoidal Heads". In: *Journal of mechanical engineering* (July 2008), p. 8.
- [6] Alicia Benitez et al. "Ecological Assessment of Fuel Cell Electric Vehicles with Special Focus on Type IV Carbon Fiber Hydrogen Tank". In: *Journal of Cleaner Production* 278 (Jan. 2021), p. 123277. ISSN: 09596526. DOI: 10.1016/j.jclepro.2020.123277. URL: <https://linkinghub.elsevier.com/retrieve/pii/S0959652620333229> (visited on 04/13/2021).
- [7] A.W Blom. *Structural Performance of Fiber-Placed, Variable-Stiffness Composite Conical and Cylindrical Shells*. S.l.: s.n., 2010. ISBN: 978-90-90-25563-7.
- [8] Mohamed Amine Bouhlef et al. "A Python Surrogate Modeling Framework with Derivatives". In: *Advances in Engineering Software* 135 (Sept. 2019), p. 102662. ISSN: 09659978. DOI: 10.1016/j.advengsoft.2019.03.005. URL: <https://linkinghub.elsevier.com/retrieve/pii/S0965997818309360> (visited on 06/14/2021).
- [9] F. C. Campbell. *Manufacturing Processes for Advanced Composites*. 2004. 533 pp.
- [10] Julien Marie Jan Ferdinand van Campen. "Optimum Lay-up Design of Variable Stiffness Composite Structures." S.l.: [s.n.], 2011. ISBN: 9789090264264.
- [11] D. van den Bergen. *Research on the Fiber Build-up of Filament Wound Products*. July 14, 2016.
- [12] Isaac Daniel. *Engineering Mechanics of Composite Materials*. Second edition. Oxford university press, 2006. 463 pp.
- [13] Frederick W DuVall. "Cost Comparisons of Wet Filament Winding versus Prepreg Filament Winding for Type II and Type IV CNG Cylinders". In: (), p. 9.
- [14] P. Francescato et al. "Comparison of Optimal Design Methods for Type 3 High-Pressure Storage Tanks". In: *Composite Structures* 94.6 (May 2012), pp. 2087–2096. ISSN: 02638223. DOI: 10.1016/j.compstruct.2012.01.018. URL: <https://linkinghub.elsevier.com/retrieve/pii/S0263822312000335> (visited on 04/13/2021).
- [15] Hirotada Fujiwara et al. "High-Pressure Gaseous Hydrogen Permeation Test Method -Property of Polymeric Materials for High-Pressure Hydrogen Devices (1)-". In: *International Journal of Hydrogen Energy* 45.53 (Oct. 2020), pp. 29082–29094. ISSN: 03603199. DOI: 10.1016/j.ijhydene.2020.07.215. URL: <https://linkinghub.elsevier.com/retrieve/pii/S0360319920328421> (visited on 04/28/2021).
- [16] G Roghrauer. "Ultra-High Pressure Composite Vessels with Efficient Stress Distribution". Dissertation. Montreal: Concordia university, June 1999. 801 pp.

- [17] M J Hinton, A S Kaddour, and P D Soden. "Predicting Failure in Fibre Composites: Lessons Learned from the World-Wide Failure Exercise". In: 13th Intl Conference on Composite Material. Beijing, p. 14.
- [18] Zhengyun Hu et al. "Investigation on Failure Behaviors of 70 MPa Type IV Carbon Fiber Overwound Hydrogen Storage Vessels". In: *Composite Structures* 259 (Mar. 2021), p. 113387. ISSN: 02638223. DOI: 10.1016/j.compstruct.2020.113387. URL: <https://linkinghub.elsevier.com/retrieve/pii/S0263822320333134> (visited on 04/13/2021).
- [19] J.M.J.F van Campen. *Pattern Search*. Nov. 29, 2013.
- [20] R. Jin, W. Chen, and T.W. Simpson. "Comparative Studies of Metamodelling Techniques under Multiple Modelling Criteria". In: *Structural and Multidisciplinary Optimization* 23.1 (Dec. 1, 2001), pp. 1–13. ISSN: 1615-147X, 1615-1488. DOI: 10.1007/s00158-001-0160-4. URL: <http://link.springer.com/10.1007/s00158-001-0160-4> (visited on 08/06/2021).
- [21] Christos Kassapoglou. *Design and Analysis of Composite Structures: With Applications to Aerospace Structures*. 1st ed. AIAA Education Series. Reston, Va. : United Kingdom : b John Wiley & Sons: American Institute of Aeronautics and Astronautics, 2010. 299 pp. ISBN: 978-0-470-97263-2 978-1-60086-780-4.
- [22] M. Knops. *Analysis of Failure in Fibre Polymer Laminates*. Springer, 2008. 208 pp.
- [23] S. Koussios. "Filament Winding, a Unified Approach". Delft: TU Delft, 2004. 400 pp.
- [24] Sotiris Koussios and Otto K. Bergsma. "Friction Experiments for Filament Winding Applications". In: *Journal of Thermoplastic Composite Materials* 19.1 (Jan. 2006), pp. 5–34. ISSN: 0892-7057, 1530-7980. DOI: 10.1177/0892705706049561. URL: <http://journals.sagepub.com/doi/10.1177/0892705706049561> (visited on 08/07/2021).
- [25] Karen Law et al. *U.S. Department of Energy Hydrogen Storage Cost Analysis*. DOE/GO14283, 1082754. Mar. 11, 2013, DOE/GO14283, 1082754. DOI: 10.2172/1082754. URL: <http://www.osti.gov/servlets/purl/1082754/> (visited on 04/13/2021).
- [26] D. Leh et al. "Multi-Sequence Dome Lay-up Simulations for Hydrogen Hyper-Bar Composite Pressure Vessels". In: *Composites Part A: Applied Science and Manufacturing* 52 (Sept. 2013), pp. 106–117. ISSN: 1359835X. DOI: 10.1016/j.compositesa.2013.05.007. URL: <https://linkinghub.elsevier.com/retrieve/pii/S1359835X13001413> (visited on 04/13/2021).
- [27] D. Leh et al. "Optimisation of 700 Bar Type IV Hydrogen Pressure Vessel Considering Composite Damage and Dome Multi-Sequencing". In: *International Journal of Hydrogen Energy* 40.38 (Oct. 2015), pp. 13215–13230. ISSN: 03603199. DOI: 10.1016/j.ijhydene.2015.06.156. URL: <https://linkinghub.elsevier.com/retrieve/pii/S0360319915016857> (visited on 04/13/2021).
- [28] S.G. Lekhnitskiy. *Anisotropic Plates*. Moscow, Mar. 11, 1969. 477 pp.
- [29] Song Lin et al. "Progressive Damage Analysis for Multiscale Modelling of Composite Pressure Vessels Based on Puck Failure Criterion". In: *Composite Structures* 255 (Jan. 2021), p. 113046. ISSN: 02638223. DOI: 10.1016/j.compstruct.2020.113046. URL: <https://linkinghub.elsevier.com/retrieve/pii/S026382232032972X> (visited on 04/13/2021).
- [30] M. Lossie and H. Van Brussel. "Design Principles in Filament Winding". In: *Composites Manufacturing* 5.1 (Mar. 1994), pp. 5–13. ISSN: 09567143. DOI: 10.1016/0956-7143(94)90014-0. URL: <https://linkinghub.elsevier.com/retrieve/pii/0956714394900140> (visited on 09/08/2021).
- [31] M Madhavi. "Computer Aided Analysis of Filament Wound Composite Pressure Vessel with Integrated End Domes Considering the Change of Winding Angles through the Thickness Direction". In: 91 (2010), p. 7.
- [32] M. Madhavi. "Design and Analysis of Filament Wound Composite Pressure Vessel with Integrated-End Domes". In: *Defence Science Journal* 59.1 (Jan. 30, 2009), pp. 73–81. ISSN: 0011748X, 0976464X. DOI: 10.14429/dsj.59.1488. URL: <http://publications.drdo.gov.in/ojs/index.php/dsj/article/view/1488> (visited on 04/13/2021).

- [33] B. Magneville et al. "Modeling, Parameters Identification and Experimental Validation of Composite Materials Behavior Law Used in 700 Bar Type IV Hydrogen High Pressure Storage Vessel". In: *International Journal of Hydrogen Energy* 40.38 (Oct. 15, 2015), pp. 13193–13205. ISSN: 0360-3199. DOI: 10.1016/j.ijhydene.2015.06.121. URL: <https://www.sciencedirect.com/science/article/pii/S0360319915016067> (visited on 09/18/2021).
- [34] P.L. Mallick. *Processing of Polymer Matrix Composites*. 356 pp.
- [35] M. Nebe et al. "Analysis on the Mechanical Response of Composite Pressure Vessels during Internal Pressure Loading: FE Modeling and Experimental Correlation". In: *Composites Part B: Engineering* 212 (May 2021), p. 108550. ISSN: 13598368. DOI: 10.1016/j.compositesb.2020.108550. URL: <https://linkinghub.elsevier.com/retrieve/pii/S1359836820335976> (visited on 04/13/2021).
- [36] M. Nebe et al. "Experimental and Analytical Analysis on the Stacking Sequence of Composite Pressure Vessels". In: *Composite Structures* 247 (Sept. 2020), p. 112429. ISSN: 02638223. DOI: 10.1016/j.compstruct.2020.112429. URL: <https://linkinghub.elsevier.com/retrieve/pii/S0263822320302944> (visited on 04/13/2021).
- [37] Panos Y. Papalambros and Douglass J. Wilde. *Principles of Optimal Design: Modeling and Computation*. 2nd ed. Cambridge ; New York: Cambridge University Press, 2000. 390 pp. ISBN: 978-0-521-62215-8.
- [38] Jae-Sung Park et al. "Analysis of Filament Wound Composite Structures Considering the Change of Winding Angles through the Thickness Direction". In: *Composite Structures* (2002), p. 9.
- [39] Levend Parnas and Nuran Katirci. "Design of Fiber-Reinforced Composite Pressure Vessels under Various Loading Conditions". In: *Composite Structures* 58.1 (Oct. 2002), pp. 83–95. ISSN: 02638223. DOI: 10.1016/S0263-8223(02)00037-5. URL: <https://linkinghub.elsevier.com/retrieve/pii/S0263822302000375> (visited on 04/13/2021).
- [40] D.M.J. Peeters. "Design Optimisation of Practical Variable Stiffness and Thickness Laminates". Delft University of Technology, 2017. DOI: 10.4233/UUID:A07EA6A4-BE73-42A6-89B5-E92D99BB6256. URL: <http://resolver.tudelft.nl/uuid:a07ea6a4-be73-42a6-89b5-e92d99bb6256> (visited on 06/11/2021).
- [41] Singiresu S. Rao. *Engineering Optimization: Theory and Practice*. 4th ed. Hoboken, N.J.: John Wiley & Sons, 2009. 813 pp. ISBN: 978-0-470-18352-6.
- [42] H.S. Roh, T.Q. Hua, and R.K. Ahluwalia. "Optimization of Carbon Fiber Usage in Type 4 Hydrogen Storage Tanks for Fuel Cell Automobiles". In: *International Journal of Hydrogen Energy* 38.29 (Sept. 2013), pp. 12795–12802. ISSN: 03603199. DOI: 10.1016/j.ijhydene.2013.07.016. URL: <https://linkinghub.elsevier.com/retrieve/pii/S0360319913017163> (visited on 04/13/2021).
- [43] Rongguo Wang et al. "A New Method for Predicting Dome Thickness of Composite Pressure Vessels". In: *Journal of Reinforced Plastics and Composites* 29.22 (Nov. 2010), pp. 3345–3352. ISSN: 0731-6844, 1530-7964. DOI: 10.1177/0731684410376330. URL: <http://journals.sagepub.com/doi/10.1177/0731684410376330> (visited on 04/13/2021).
- [44] J Rousseau and D Perreux. "The Influence of Winding Patterns on the Damage Behaviour of Filament-Wound Pipes". In: *Composites Science and Technology* (1999), p. 11.
- [45] A. K. Roy and S. W. Tsai. "Design of Thick Composite Cylinders". In: *Journal of Pressure Vessel Technology* 110.3 (Aug. 1, 1988), pp. 255–262. ISSN: 0094-9930, 1528-8978. DOI: 10.1115/1.3265597. URL: <https://asmedigitalcollection.asme.org/pressurevesseltech/article/110/3/255/439102/Design-of-Thick-Composite-Cylinders> (visited on 04/13/2021).
- [46] S. Klardie. *Tape Build-up and Manufacturing Strategy for High-Pressure Composite Pressure Vessels Made with Tapes*. 29-9-20.
- [47] S. McWhorther and G. Ordaz. *Onboard Type IV Compressed Hydrogen Storage Systems – Current Performance and Cost*. July 17, 2013.
- [48] P D Soden, A S Kaddour, and M J Hinton. "Recommendations for Designers and Researchers Resulting from the World-Wide Failure Exercise". In: *Composites Science and Technology* (2004), p. 16.

- [49] Stephen W Tsai and Edward M Wu. "A General Theory of Strength for Anisotropic Materials". In: *Journal of Composite Materials* (), p. 23. DOI: 10.1177/002199837100500106.
- [50] V.V. Vasiliev. *Composite Pressure Vessels*. 2009. 607 pp.
- [51] V.V. Vasiliev, A.A. Krikanov, and A.F. Razin. "New Generation of Filament-Wound Composite Pressure Vessels for Commercial Applications". In: *Composite Structures* 62.3-4 (Jan. 2003), pp. 449–459. ISSN: 02638223. DOI: 10.1016/j.compstruct.2003.09.019. URL: <https://linkinghub.elsevier.com/retrieve/pii/S0263822303002575> (visited on 05/12/2021).
- [52] Rongguo Wang et al. "Dome Thickness Prediction of Composite Pressure Vessels by a Cubic Spline Function and Finite Element Analysis". In: *Polymers and Polymer Composites* 19.2-3 (Mar. 2011), pp. 227–234. ISSN: 0967-3911, 1478-2391. DOI: 10.1177/0967391111019002-327. URL: <http://journals.sagepub.com/doi/%2010.1177/0967391111019002-327> (visited on 04/13/2021).
- [53] Rongguo Wang et al. "Slippage Coefficient Measurement for Non-Geodesic Filament-Winding Process". In: *Composites Part A: Applied Science and Manufacturing* 42.3 (Mar. 2011), pp. 303–309. ISSN: 1359835X. DOI: 10.1016/j.compositesa.2010.12.002. URL: <https://linkinghub.elsevier.com/retrieve/pii/S1359835X10003106> (visited on 07/28/2021).
- [54] M Xia, H Takayanagi, and K Kemmochi. "Analysis of Multi-Layered Filament-Wound Composite Pipes under Internal Pressure". In: *Composite Structures* (2001), p. 9.
- [55] Ming Zhang et al. "A Literature Review of Failure Prediction and Analysis Methods for Composite High-Pressure Hydrogen Storage Tanks". In: *International Journal of Hydrogen Energy* 44.47 (Oct. 2019), pp. 25777–25799. ISSN: 03603199. DOI: 10.1016/j.ijhydene.2019.08.001. URL: <https://linkinghub.elsevier.com/retrieve/pii/S0360319919329106> (visited on 04/13/2021).
- [56] Q. Zhang et al. "Analytical Solution of the Thermo-Mechanical Stresses in a Multilayered Composite Pressure Vessel Considering the Influence of the Closed Ends". In: *International Journal of Pressure Vessels and Piping* 98 (Oct. 2012), pp. 102–110. ISSN: 03080161. DOI: 10.1016/j.ijpvp.2012.07.009. URL: <https://linkinghub.elsevier.com/retrieve/pii/S0308016112000944> (visited on 04/13/2021).
- [57] Qian Zhang et al. "Design of a 70 MPa Type IV Hydrogen Storage Vessel Using Accurate Modeling Techniques for Dome Thickness Prediction". In: *Composite Structures* 236 (Mar. 2020), p. 111915. ISSN: 02638223. DOI: 10.1016/j.compstruct.2020.111915. URL: <https://linkinghub.elsevier.com/retrieve/pii/S0263822319344897> (visited on 04/13/2021).
- [58] Lei Zu, Sotiris Koussios, and Adriaan Beukers. "Design of Filament-Wound Domes Based on Continuum Theory and Non-Geodesic Roving Trajectories". In: *Composites Part A: Applied Science and Manufacturing* 41.9 (Sept. 2010), pp. 1312–1320. ISSN: 1359835X. DOI: 10.1016/j.compositesa.2010.05.015. URL: <https://linkinghub.elsevier.com/retrieve/pii/S1359835X10001569> (visited on 04/13/2021).
- [59] Lei Zu, Jihui Wang, and Shuxin Li. "Analysis of Multi-Layered Thick-Walled Filament-Wound Hydrogen Storage Vessels". In: *International Journal of Hydrogen Energy* 39.36 (Dec. 2014), pp. 21083–21096. ISSN: 03603199. DOI: 10.1016/j.ijhydene.2014.10.075. URL: <https://linkinghub.elsevier.com/retrieve/pii/S0360319914029152> (visited on 04/13/2021).
- [60] Lei Zu et al. "Design and Analysis of Filament-Wound Composite Pressure Vessels Based on Non-Geodesic Winding". In: *Composite Structures* 207 (Jan. 2019), pp. 41–52. ISSN: 02638223. DOI: 10.1016/j.compstruct.2018.09.007. URL: <https://linkinghub.elsevier.com/retrieve/pii/S0263822318327533> (visited on 04/13/2021).

A

Baseline design

A winding pattern is constructed in TW by first creating a single winding path for the specified winding angle. In this thesis the initial winding angle is calculated at the cylindrical section and the final winding angle is on the dome section which is 90 degrees to ensure a continuous winding path. Using this path, a variety of winding pattern solutions are calculated by TW. For a single winding path a variety of winding patterns can be created, as shown in Figure A.1. These patterns are different in the number of angular partitions and how many positions are skipped. The goal is to achieve a coverage which is close to the desired value, in this case 200%. However, high patterns should be avoided as these may contain voids [44]. The dwell angle of the pattern should be low, as a larger dwell angle will result in a higher thickness build up at the polar boss. The winding pattern parameters for the baseline design are defined in Table A.1 and illustrated in Figure A.2 and Figure A.3. A hoop path is shown in Figure A.4. The number of loops, N , is halved during the production, as the aim is to position two tapes for a single winding path. For the baseline design a 33/32 lagging pattern is chosen with $N = 164$, because it minimises the dwell angle and the coverage. The 65/53 pattern is not chosen, as it is a high pattern.

	p	q	Lead/Lag	Dwell [deg]	N	Coverage [%]
1	39	38	-1	1.3827	310	191.0601
2	31	30	1	0.2587	312	192.2928
3	39	38	1	1.4419	314	193.5254
4	63	61	-1	0.2954	314	193.5254
5	63	61	1	0.3317	316	194.7581
6	32	31	-1	0.3675	318	195.9907
7	40	39	-1	1.4996	318	195.9907
8	32	31	1	0.4378	322	198.4560
9	40	39	1	1.5558	322	198.4560
10	65	63	-1	0.4723	324	199.6887
11	41	40	-1	1.6107	326	200.9213
12	65	63	1	0.5064	326	200.9213
13	33	32	-1	0.5401	328	202.1539
14	41	40	1	1.6642	330	203.3866
15	33	32	1	0.6062	332	204.6192
16	42	41	-1	1.7165	334	205.8519
17	67	65	-1	0.6387	334	205.8519
18	67	65	1	0.6707	336	207.0845
19	34	33	-1	0.7024	338	208.3172
20	42	41	1	1.7675	338	208.3172
21	34	33	1	0.7647	342	210.7825
22	43	42	-1	1.8174	342	210.7825

Figure A.1: Possible winding patterns generated by TW

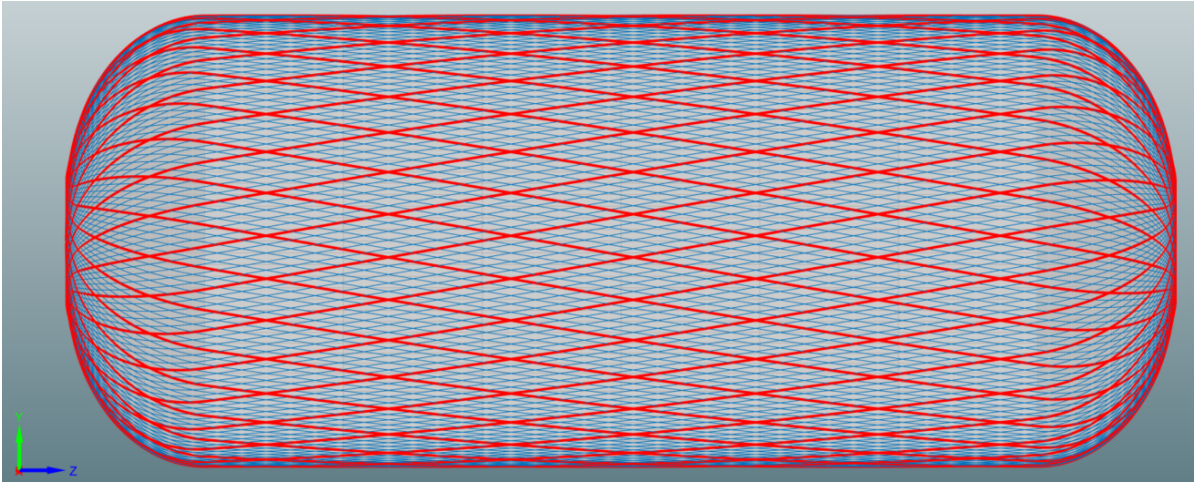


Figure A.2: Front-view of the winding pattern used for the first helical layer of the baseline design

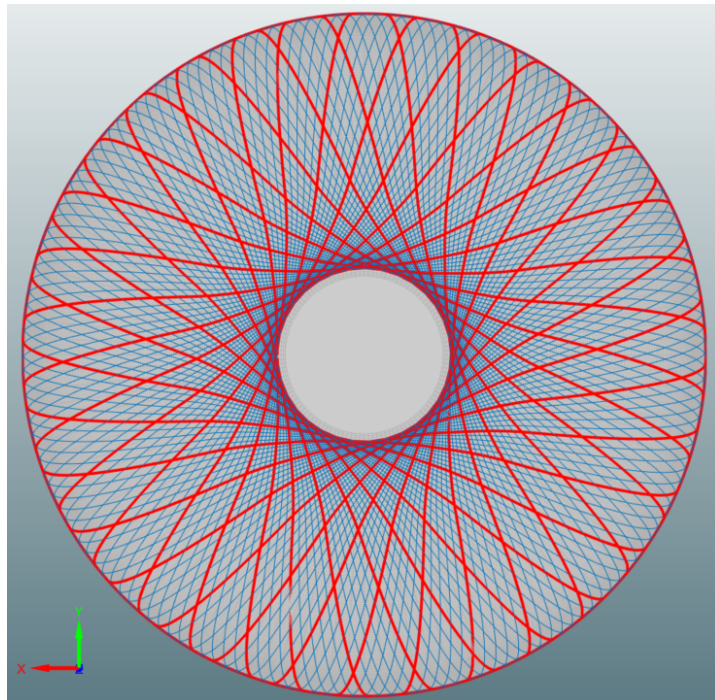


Figure A.3: Side-view of the winding pattern used for the first helical layer of the baseline design

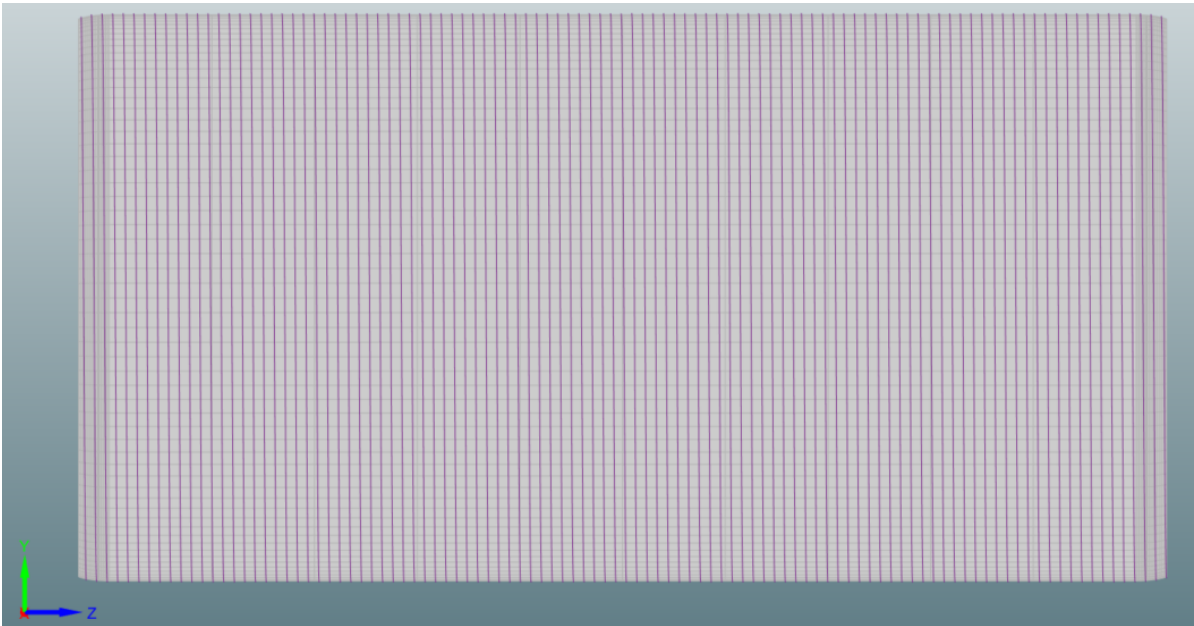


Figure A.4: Hoop winding path for the first hoop ply which starts and end slightly on the dome section

Table A.1: Winding pattern parameters for the optimised design

Parameter	unit	value
p	-	33
q	-	32
Type	-	lagging
Dwell	deg	0.54
Coverage	%	202.15
n_{loops}	-	164

B

Optimised design

To manufacture the optimised design calculated in Section 4.3, a winding pattern is created using TW. The winding pattern is illustrated in Figure B.1 and Figure B.2. This pattern uses the parameters defined in Table B.1. It can be seen that the resulting pattern has slightly higher coverage than desired. This pattern is chosen because a 71/15 is a high pattern which may result in deficiencies, such as voids. In Figure B.3 the machine path is shown, these coordinates are used for the creation of the robot path and are discretised at several green nodes, which will be the input for the robot. The Kuka robot available at the samXL facility is illustrated in Figure B.4 simulating the first helical layer.

Table B.1: Winding pattern parameters for the optimised design

Parameter	unit	value
p	-	37
q	-	8
Type	-	lagging
Dwell	deg	1.38
Coverage	%	203.1
n_{loops}	-	162

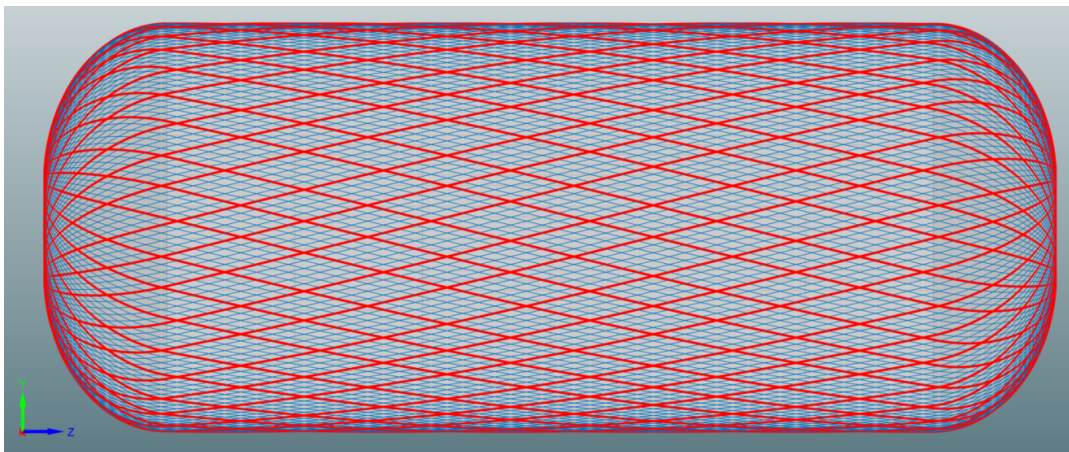


Figure B.1: Front-view of the winding pattern used for the first helical layer of the optimised design

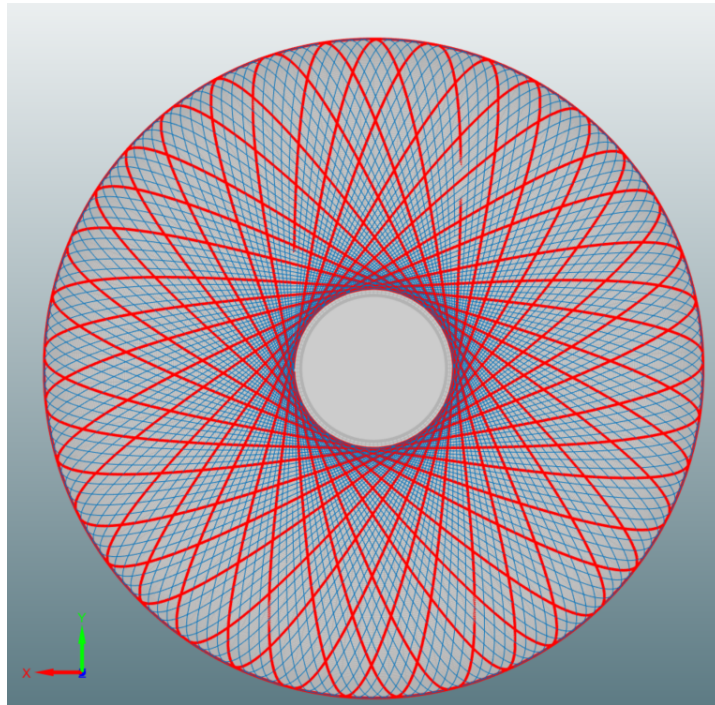


Figure B.2: Side-view of the winding pattern used for the first helical layer of the optimised design

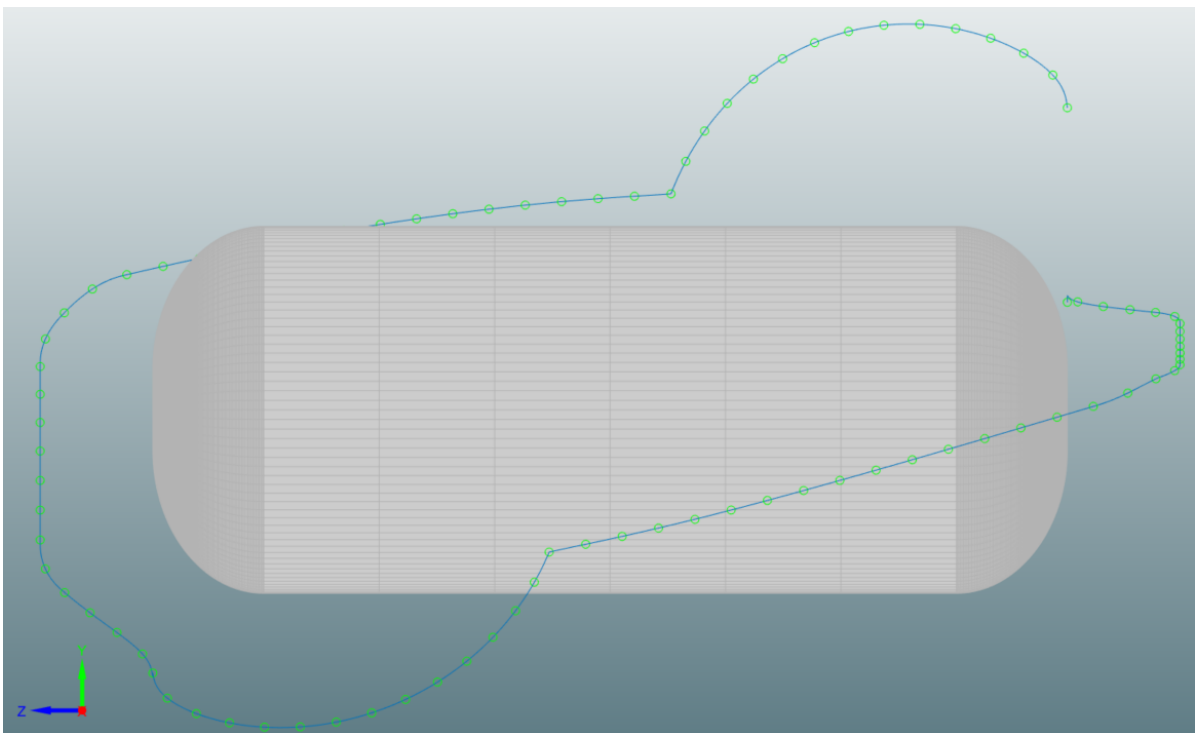


Figure B.3: Machine path used to position the tow-preg on the mandrel of the optimised design

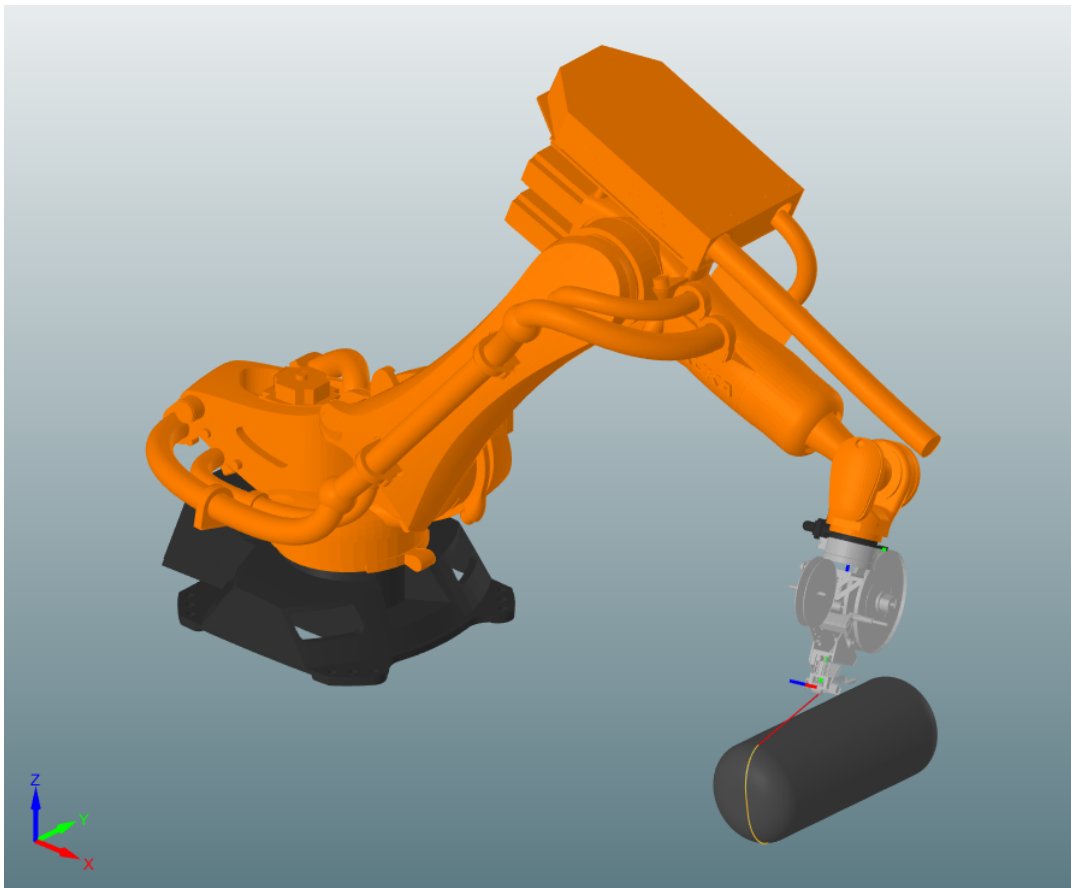


Figure B.4: Visualisation of the virtual Kuka robot, winding the first helical path

C

Manufacturing defects

Several manufacturing defects have been observed during the production trials of the CPV, using the AFP robot head. The first defects initiated during re-spooling of the tow-preg. The distance between the bobbin and first spool were too low, i.e. too low pressure on the tape, which raised the opportunity to twist around its axis, shown in Figure C.2 This resulted in several folds at the Hafner spool. The folding was mostly mitigated by re-spooling using the frozen material, in which the material has more in-plane stiffness. However, this might cause yarn breakage as advised by the material manufacturer. The material is wound helically on the bobbin. This ensures that during production that the tape does not remove fibres from adjacent layers. However, once the material has been re-spooled the material is stacked vertically. This resulted in loose fibres during production, as shown in Figure C.1 and Figure C.3. This effect could be alleviated by a slower robot motion. However, it was not possible to fully prevent this effect. A fully 200% coverage pattern is shown in Figure C.4. This shows that due to the folds the mandrel periphery is not fully covered with tape, which results in a reduced mechanical strength at these positions.

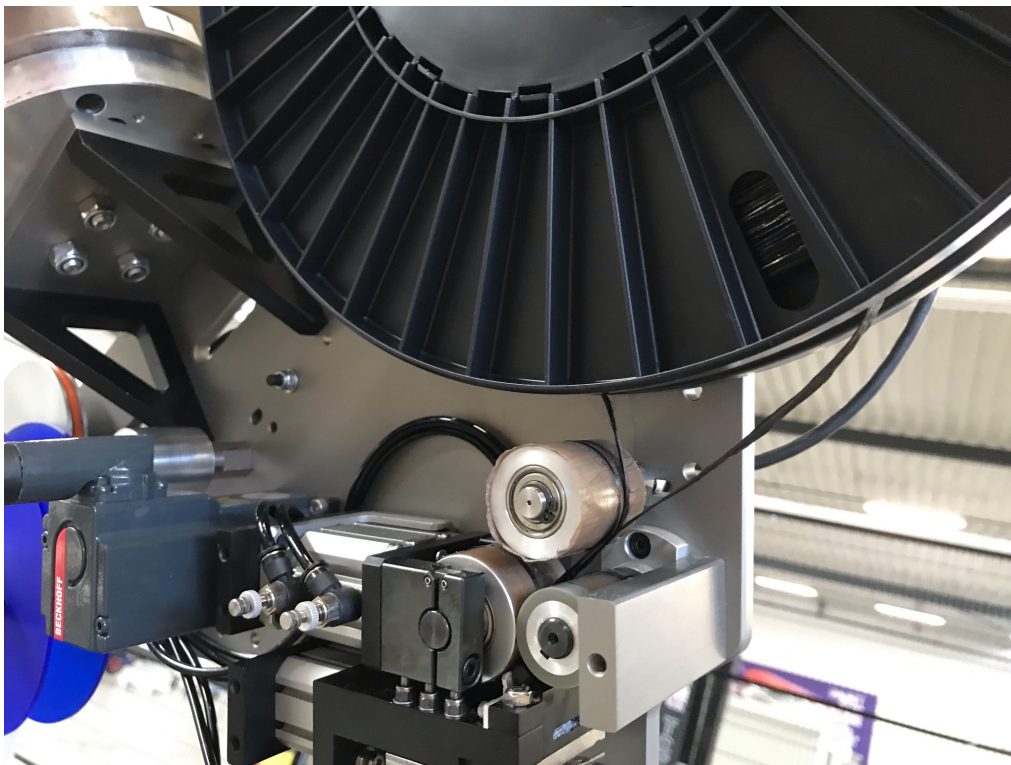


Figure C.1: Disintegrated tow-preg on the AFP head, which initiated on the Hafner spool



Figure C.2: Fold created during the re-spooling



Figure C.3: Loose fibres positioned on the mandrel



Figure C.4: Voids in the winding pattern, caused by folded tape